CERN-ACC-2022-0004
rogelio.tomas@cern.ch

Optics Measurement and Correction Strategies for HL-LHC

X. Buffat, F. Carlier, J. Coello, R. De Maria, J. Dilly, E. Fol,
N. Fuster-Martínez, D. Gamba, H. García Morales,
A. García-Tabares, M. Giovannozzi, M. Hofer, N. Karastathis,
J. Keintzel, M. Le Garrec, E.H. Maclean, L. Malina, T.H.B. Persson,
P. Skowronski, F. Soubelet, R. Tomás, F. Van der Veken,
L. Van Riesen-Haupt, A. Wegscheider and D.W. Wolf,
CERN, Geneva, Switzerland.
J. Cardona,
Universidad Nacional de Colombia.
B. Dalena and T. Pugnat,
CEA, Saclay, France.

CERN-ACC-2022-0004
22/01/2024

Abstract

The baseline strategy for optics commissioning in the HL-LHC era is presented and reviewed in detail, along with recent developments and unsolved matters in the linear and nonlinear optics measurement and correction techniques.

Geneva, Switzerland
January 22, 2024

Contents

1 Introduction

As part of the HL-LHC project [1], the ATLAS and CMS Interaction Region (IR) magnets will be replaced with larger aperture components to allow reaching β^* at the Interaction Point (IP) as low as 15 cm in the round optics and 7.5 cm in the flat optics [2, 3]. The geometric luminosity loss from a full crossing angle of 500 µrad is partially mitigated with local crab cavities [4], generating a crabbing angle of 380 µrad. Figure 1 shows the layout of the new IR.

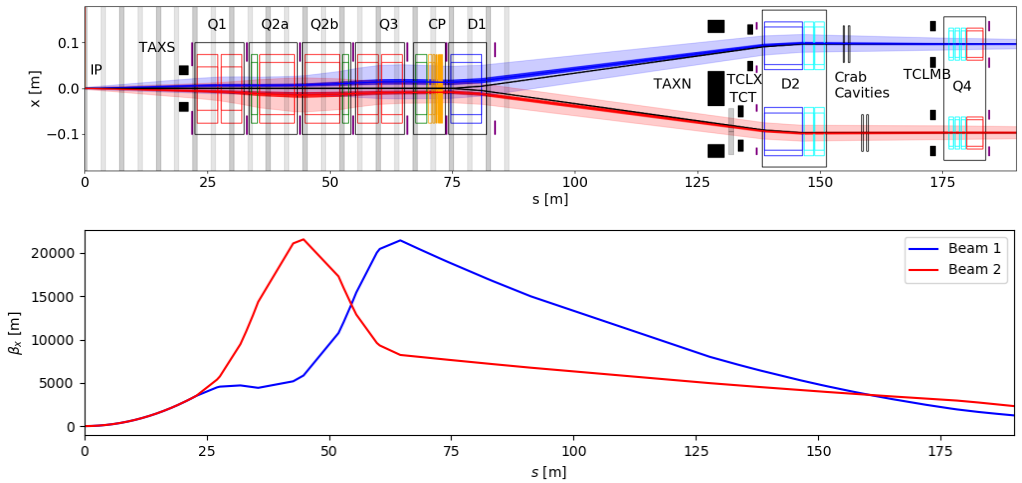

Figure 1: HL-LHC IR layout (top) and β-function (bottom) for $\beta^* = 15$ cm. Quadrupoles are shown in red, separation dipoles in blue (D1 and D2), orbit correctors in green (MCBXF) and cyan (MCBRD and MCBY), beam position monitors in black ticks, and high order corrector magnets in orange grouped in the corrector package (CP). The bottom plot shows the corresponding horizontal β-functions for Beam 1 (blue) and Beam 2 (red). The Beam 1 vertical β-function is equal to the horizontal β-function of Beam 2 and similarly for the Beam 1 horizontal β-function.

At $\beta^* = 15$ cm, the luminosity could reach $16.9 \times 10^{34}\,\mathrm{cm}^{-2}\mathrm{s}^{-1}$ generating a too high event pile-up for the detectors. Hence, luminosity will be leveled by acting on the β^* mainly. A leveled luminosity of $5 \times 10^{34}\mathrm{cm}^{-2}\mathrm{s}^{-1}$ needs a β^* of about 60 cm at nominal intensity and with crab cavities on. Cryogenics limitations in the first 30 minutes of the physics fill [5] might require reducing the initial luminosity below the nominal value, down to $2.5 \times 10^{34}\mathrm{cm}^{-2}\mathrm{s}^{-1}$. For this lower luminosity, the initial β^* could be about 1 m with zero crabbing angle.

The start of HL-LHC with beam is foreseen for 2029, when a large campaign of magnet training will be required to reach 7 TeV for the new HL-LHC mag-

Table 1: Performance, full crossing angle (θ) and β^* targets in the HL-LHC luminosity ramp-up years. An emittance of $\varepsilon = 2.5$ μm is assumed for all years. β^*_{start} and β^*_{end} correspond to the IP β-function at the start and at the end of the physics fill. β^*_{start} is defined to deliver $2.5\times10^{34}\text{cm}^{-2}\text{s}^{-1}$ at the start of the fill to meet requests from cryogenics.

Year	ppb $[10^{11}]$	Virtual lumi. $[10^{34}\text{cm}^{-2}\text{s}^{-1}]$	Days in physics	θ [µrad]	β^*_{start} [cm]	β^*_{end} [cm]	Crab cav.
2029	1.7	3.95	30	450	50	30	off
2030	1.7	3.95	120	450	50	30	exp
2031	2.2	10.3	140	500	100	25	on
2032	2.2	13.5	160	500	100	20	on
2031			Long shutdown 4				
2033	2.2	13.5	170	500	100	20	on
2034	2.2	16.9	200	500	100	15	on

nets and, possibly, part of the arc dipoles. Table 1 shows the baseline ramp-up plan to reach HL-LHC nominal operation [6]. The main operational goal in 2029 will be to recover Run 3 performance, aiming at a minimum $\beta^* = 30$ cm and a bunch charge about 1.7×10^{11} ppb. Note that this ramp-up plan is evolving as this document is being finalized [7].

As proton burn-off from luminosity reduces the bunch intensity during the physics fill, β^* is simultaneously reduced step-wise in ATLAS and CMS to level the instantaneous luminosity. The following effects will introduce a luminosity imbalance between the two detectors:

- Optics errors affecting β^* and linear coupling, these are the main topic of this report.
- Errors in the crossing and crabbing angles, including crabbing in the non-crossing plane generated from tilts or from a non-closure of the crabbing bump in the other IP.
- A difference in the horizontal and vertical emittances, which introduces a luminosity imbalance for equal crossing and crabbing angles in the two IPs, since the crossing planes are orthogonal in IR1 and 5.
- The beam-beam head-on and long-range interactions introduce up to 15% peak β-beating at the highest bunch intensity [8, 9]. Assuming this peak beta-beating in both planes at the IP, the corresponding luminosity loss would be about 7%, see Appendix A.

The preferred technique to equalise the luminosities in the two detectors is by applying a separation offset in the IP with the largest luminosity. Separations

below 1 σ in that IP should suffice to equalise luminosities. However, reaching the end of the fill with a separation in one IP should be avoided as it implies a loss of integrated luminosity. Therefore, tolerances to imperfections will be the tightest at the lowest β^*.

Crossing angle can also be used for luminosity levelling and to mitigate the radiation dose in the IR magnets. Indeed, in the "adaptive" scenario [10], the crossing angle is reduced during the fill while ensuring a dynamic aperture (DA) of 6 σ. A minimum full crossing angle of about 400 µrad could be achieved towards the end of the physics fill. At the start of the fill, a crossing angle as low as 300 µrad has been considered to reduce the radiation dose into IR magnets [11]. In summary, in the HL-LHC it is considered to change the full crossing angle in the range between 300 µrad and 500 µrad in the start of the fill and between 400 µrad and 500 µrad in the end. The separation offset throughout the fill will be between 0 and 1 σ.

The MCBFX and MCBRD magnets are orbit correctors involved in the generation of IR orbit bumps and orbit correction. Their multipolar components can generate significant optics errors and have a non-negligible impact on dynamic aperture [12, 13, 14]. This will require the implementation of time-dependent linear and nonlinear corrections based on extensive magnetic measurements. In addition, another means of mitigation is based on the use of orbit correction approaches that minimise the deviation of the settings of these magnets from their nominal strength. In this respect, the Full Remote Alignment System (FRAS) (see Ref. [15] and references therein) provides an efficient tool for this purpose.

The HL-LHC optics commissioning will therefore face unprecedented challenges [16] aiming to reach the following goals:

- Peak β-beating $\leq$ 20% around the ring, as assumed in aperture calculations [17] to guarantee a relative beam size deviation below 10%, so to ensure reaching the overall machine protection and the feasibility of the nominal value of β^*.
- β^*-beating $\leq$ 2.5% to guarantee a luminosity imbalance $\leq$ 5% between ATLAS and CMS, especially towards the end of the physics fill with the lowest β^* configuration and the lowest bunch intensity.
- Betatron phase advance between dump kickers and IR 1 & 5 tertiary collimators should match the design within 20 degrees. This tolerance is based on LHC Run 2 experience.
- IP horizontal and vertical dispersions should be below 7 mm in absolute value to guarantee an instantaneous luminosity reduction below 1% at the end of the fill with $\beta^* = 15$ cm.
- In the start of the physics fill it might be possible to relax the β^*-beating

tolerance above 2.5%, probably up to 5%, since equalising luminosity with separation will be required anyway due to the beam-beam luminosity shift of up to 7%, see Appendix A.

- Global linear coupling should be corrected so that the closest tune approach is $\Delta Q_{\min} \leq 10^{-3}$ to avoid deteriorating Landau damping [18] and DA [19] at a fractional tune split $Q_y - Q_x \approx 5 \times 10^{-3}$.
- Local linear coupling at the IP should be corrected to guarantee a luminosity reduction below 1%, which requires $|f_{1001}|^2 + |f_{1010}|^2 \leq 0.005$ at the IP, under the assumption that $|f_{1001}| \approx |f_{1010}|$ [20].
- Triplet octupolar errors should be locally corrected to keep the generated amplitude detuning within design tolerance for optimal Landau damping [21]. The residual detuning after correction should be compensated with the arc octupoles, yet maintaining the DA, which is most challenging during the collision adjustment process as the maximum octupole current with DA of 6 σ is the same value as needed for stability, 460 A [22] (for the baseline scenario at the start of physics, i.e. with $\beta^* = 1$ m, and ATS factor [23] of 1). The residual amplitude detuning from the IR after ideal corrections is only 6 A (assuming non-linear corrections up to dodecapolar order but with pessimistic $b_6 = 4$ in the quadrupoles), which is considered sufficiently low. In the first years of HL-LHC operations, the bunch intensity will be up to 1.8×10^{11} and therefore an increased margin above 100 A equivalent Landau octupoles is expected. At the end of the levelling, i.e. with a $\beta^* = 20$ cm the octupole current is set by the less bright witness bunches leaving a margin of about 200 A. The ideal residual detuning from the IR is about 150 A.
- All IR multipolar components should be locally corrected within a 30% accuracy [24] from DA considerations.
- Feed-down effects from separation offsets at the level of 1 σ or from full crossing angle changes at the level of 200 µrad at the start of the fill and 100 µrad at the end should generate negligible optics aberrations.

2 HL-LHC lattice imperfections and performance of instruments used for optics measurements

2.1 Triplet quadrupoles

According to [25] the MQXFA magnet must provide an integrated gradient between 554 T and 560 T when powered with a current of 16.470 kA. The difference between the integrated gradient of any pair of series magnets with the same cross-section shall be smaller than 3 T, which, in relative terms, corresponds to

50×10^{-4}. First magnetic measurements of four triplet quadrupoles, including magnets with different cross sections, lie within this 50×10^{-4} tolerance [26]. The MQXFA magnetic length requirement is 4.2 m with a tolerance of ±5 mm at 1.9 K. The relative precision of the measurement of the integrated gradient shall be within $\pm2\times10^{-4}$. The global systematic relative error of the integrated gradient measurement is assumed to be within $\pm10\times10^{-4}$ [27].

The positions of the local magnetic centre and magnetic field angle are measured along the magnet axis with values obtained by averaging over sections of 500 mm maximum length. In each section, the local magnetic centre is to be within ±0.5 mm from the magnet magnetic axis both in horizontal and in vertical directions. The local magnetic field angle in each section is to be ±2 mrad from the average magnetic field angle of the whole magnet.

According to [28], the common average MQXFA field angle with respect to the cold mass fiducials should be measured with an accuracy better than 0.5 mrad. The magnetic length and nodal points of each of the two MQXFA magnets in the cold mass need to be known within ±1 mm accuracy relative to external fiducials. In [29, 30] the alignment of the average magnetic axis of each cryostat with respect to the ideal reference orbit is assumed to be within ±0.5 mm, while the field angle is assumed to be within ±1 mrad for quadrupoles and ±0.5 mrad for dipoles. With these assumptions, the expected residual rms orbit after correction is to be below 0.4 mm rms with respect to the magnetic axis of each element [30]. Recently the alignment values have been reviewed in a dedicated EDMS document [31] concluding that right after the alignment campaign the triplets should be within ±0.65 mm transversely, yielding an rms orbit after correction below 0.5 mm. During a year, ground motion has the potential to significantly deteriorate this value, especially in IR5. If this occurs additional alignment will be required.

To mitigate the removal of the Q2A trim power converter [32] it was agreed that Q2A and Q2B pairing would be performed to ensure that the difference of the transfer function of the two quadrupoles in the Q2 circuit would not exceed 20 units [33].

Figure 2 shows the expected HL-LHC rms and peak β-beating generated by the triplet quadrupoles gradient errors described above when applying pairing to the Q2 quadrupoles, at $\beta^* = 30$ cm. The distribution of the magnetic errors for the 1000 seeds used in the simulation are shown in Fig. 3. An illustration of the errors for one seed can be found in [34]. Optics configurations with $\beta^* < 30$ cm were not useful for estimating the resulting β-beating since a significant fraction of the seeds could not successfully converge. One can see that the rms β-beating peaks at around 10% β-beating and gives a maximum rms slightly above 50%. The maximum β-beating exceeds 100%, therefore a significant effort must be put in correcting the errors introduced by the triplet. A large contribution to the total

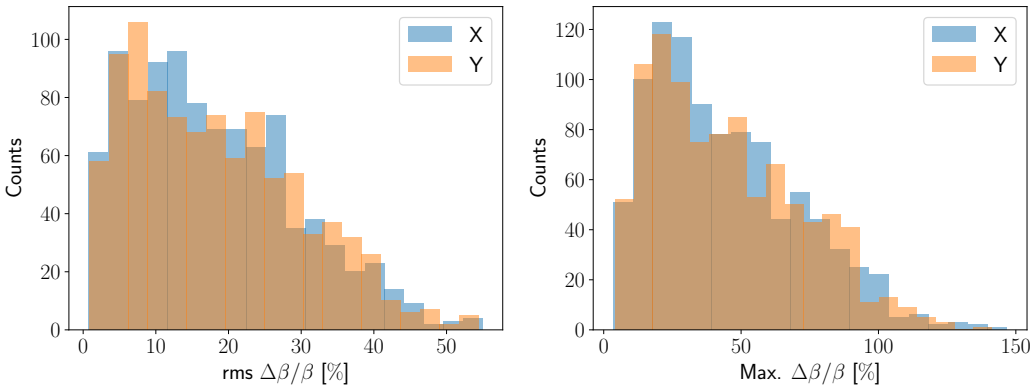

Figure 2: Expected HL-LHC rms (left) and peak β-beating (right) distributions for 1000 randomly-assigned gradient errors in the triplet quadrupoles and after pairing Q2 quadrupoles for optics v1.3 and $\beta^* = 30$ cm.

β-beating observed comes from the systematic error associated with the Q2 gradient measurement of 10 units, as mentioned above. This alone produces 10% rms β-beating, while the random component only contributes by about $2-3\%$ rms. Due to its importance, predicting the value of the systematic component is being studied using Machine Learning tools. The effect of sorting in Q2 was also evaluated resulting in minor differences of the β-beating before correction between different sorting strategies due to the large uncertainty introduced by systematic errors.

Nonlinear errors in the IRs can also feed-down to generate non-negligible β-beating in the HL-LHC when crossing angles are applied. Figure 4 shows the peak β-beat obtained in either transverse plane, due to feed-down at $\beta^* = 0.15\,\text{m}$ (250 µrad crossing-angle). Histograms are shown over the sixty wise seeds before (red) and after (blue) correction of the nonlinear errors in the IRs. Correction of the nonlinearities in the IRs is evidently necessary to maintain an acceptable β-beat at low-β^*, however even after nonlinear corrections are applied some residual optics errors may still need to be compensated with the quadrupoles. It should be noted that the expected β-beat due to feed-down will scale with both the β^* and crossing-angle, so is of greatest concern at end-of-squeeze.

2.2 Separation dipoles

Expected quadrupolar and sextupolar errors in the IR1 and IR5 D1 and D2 dipoles are shown in Table 2. The actual error assigned is given by the systematic error, plus the so-called uncertainty error, which is multiplied by a Gaussian truncated at 1.5σ and rescaled to unity, with σ equal to the uncertainty, plus the so-called

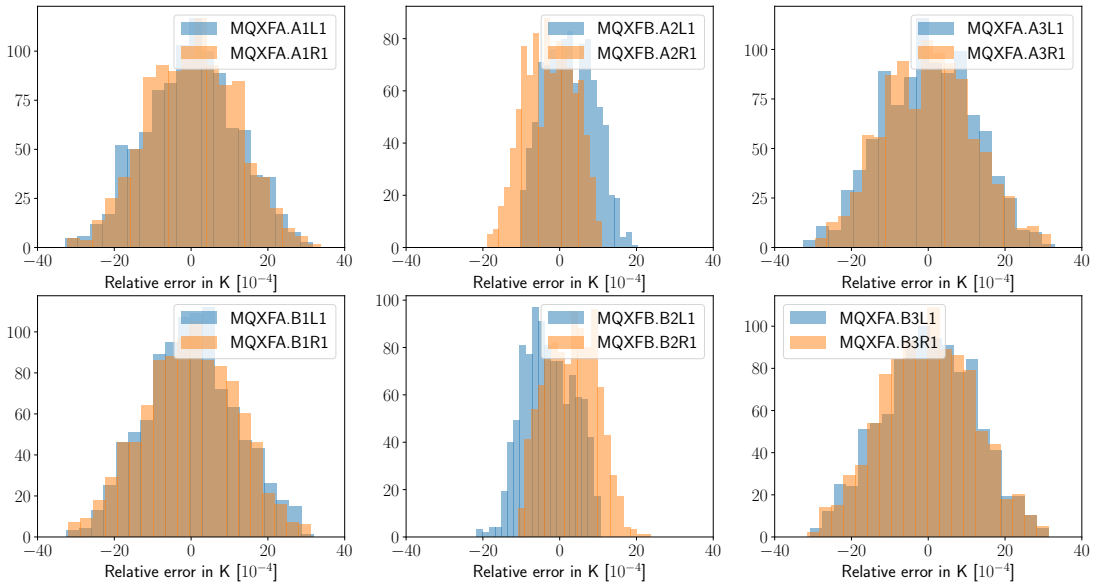

Figure 3: Magnetic error distributions in the triplet quadrupoles of IR1. Similar distributions are found for IR5. Left plots are for Q1, middle plots for Q2 and right plots for Q3. The offset between left and right Q2s is due to the sorting choice but it does not affect the resulting β-beating.

random error which is multiplied by a second Gaussian truncated at 3σ (but not rescaled). The impact on the β-beating is shown in Figs. 5 and 6 for the case of D1 and D2, respectively, for nominal round collision optics (β^*=15 cm). In these simulations only the field quality of a single magnet's family is included and the b_2 and b_3 components are assigned one at a time.

The impact on β-beating of the b_3 component is almost twice as large as that of the b_2, but the use of the nonlinear correctors ensures a very efficient cancellation of the β-beating.

D2 features a systematic b_2 component due to the peculiar design of the coils. This effect is clearly visible in the distribution of the rms β-beating that peaks at 3% in both planes and beams and reaches a maximum value of 8%. This is sufficiently large to pre-compute corrections based on magnetic measurements. The close-by Q4 magnet could be used as a local corrector for this effect. However, validation with the beam of this local correction might be difficult due to the expected large errors coming from the nearby triplet quadrupoles (the use of the special ballistic optics with switched off triplets and large β-functions might be explored). The feed-down from b_3 is, on the other hand, negligible and should not

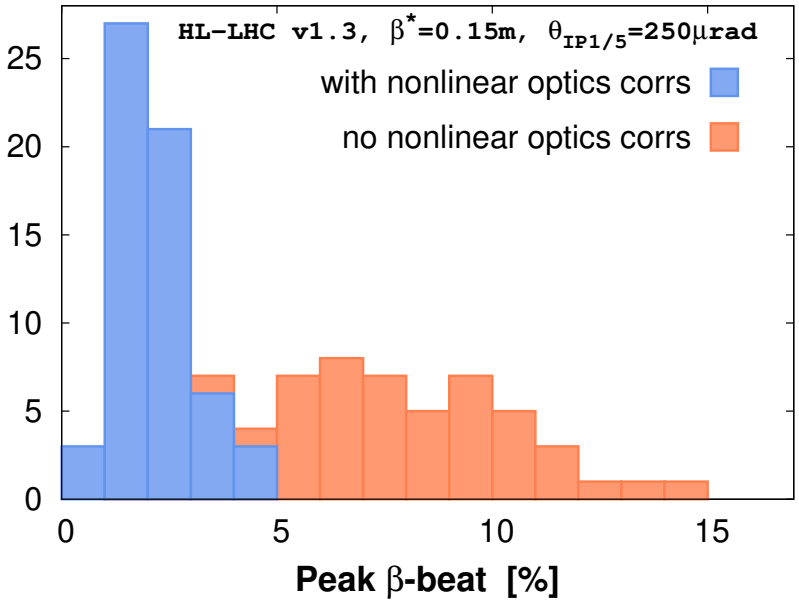

Figure 4: Predicted peak β-beat due to feed-down in the IRs at $\beta^* = 0.15\,\mathrm{m}$ (250 µrad crossing-angle). Values shown are the peak β-beat in either transverse plane before and after application of nonlinear corrections in the IRs.

be a source of concern for the beam commissioning.

2.3 Orbit correctors

As shown in Fig. 1, the new layout of IR1 and IR5 comprises two new types of orbit correctors, namely MCBXF and MCBRD. The expected values of the main multipoles for these corrector magnets are reported in Table 2 [35, 36]. Note that a 2D modelling of the MCBXF errors is under preparation, which could potentially reduce the expected values of b_3 and a_3. The random part of the multipoles has been computed by taking the total interval of variation of the multipole, as provided in the official acceptance criteria, and dividing it by $\sqrt{12}$ to match the standard deviation of the Gaussian generation of multipoles in the error routines to the uniform distribution assumed in the acceptance criteria.

The impact of the field quality of the MCBXF magnets is particularly relevant as it can be seen in Fig. 7, where the impact of the b_2 and b_3 components of the MCBXF on the β-beating is evaluated for both beams. It is worth noting that the MCBXF magnets have a two-fold function: they generate the crossing and separation bumps and, at the same time, they provide the correction of the transverse misalignment of the triplet quadrupoles. This implies that the strength usage is not fully known, depending on the actual misalignment of the triplets. This is taken

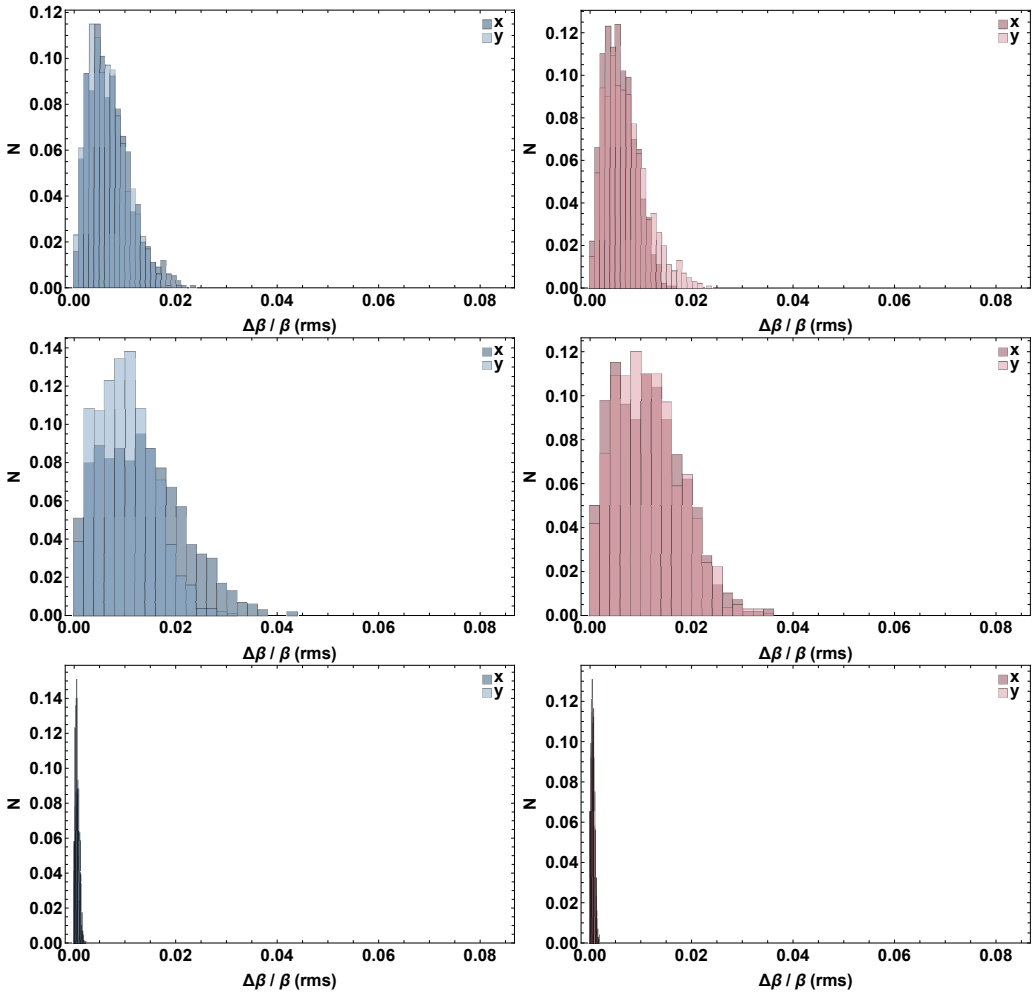

Figure 5: RMS beta-beating generated by the b_2 (upper row), b_3 component without correction (middle row), b_3 component with correction (lower row) of the D1 separation dipoles. Horizontal and vertical values are shown in each plot, while Beam 1 and Beam 2 results are reported in the first and second column, respectively.

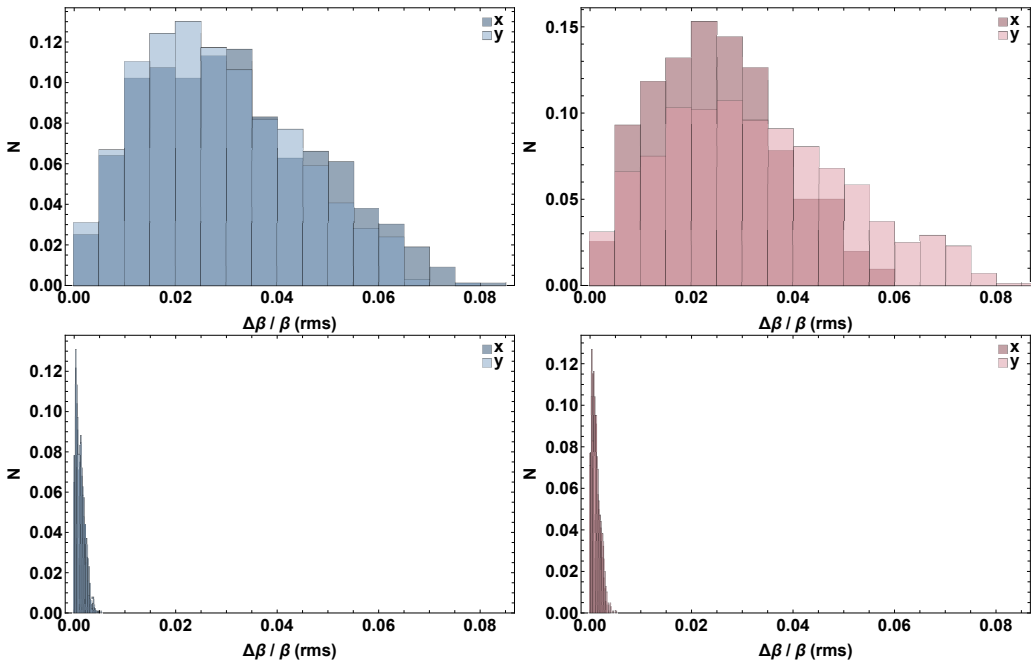

Figure 6: RMS β-beating generated by the b_2 (upper row) and feed-down from the b_3 component (lower row) of the D2 separation dipoles for the HL-LHC optics v1.4 at $\beta^* = 15$ cm. Horizontal and vertical values are shown in each plot, while Beam 1 and Beam 2 results are reported in the first and second column, respectively.

into account by using the maximum strength in the numerical simulations. This is what generates the data shown in the first two upper rows of Fig. 7, while the b_2 generates an RMS β-beating that peaks at about 1%, the presence of systematic b_3 and a_3 components shifts the β-beating generated by feed-down towards several percent. The difference between the two planes is due to the difference between a_3 and b_3 values.

The FRAS has been recently added to the HL-LHC baseline as a means to provide an efficient realignment of active and passive elements in the HL-LHC experimental IRs. Under the assumption of an optimal performance of FRAS, one can assume that the transverse misalignment of the triplets is corrected by FRAS and, hence, the MCBXF magnets will run close to their nominal strength. Under these idealised conditions, the β-beating generated is much reduced (see the third and fourth rows of Fig. 7). In particular, the impact of the b_2 component is in the noise of the β-beating level, while the feed-down from a_3 and b_3 is reduced by about a factor of two. If one assumes that these nonlinear field errors are compensated using the nonlinear correctors close-by, which has been shown in simulations to work well, the impact of MCBXF field quality on β-beating seems

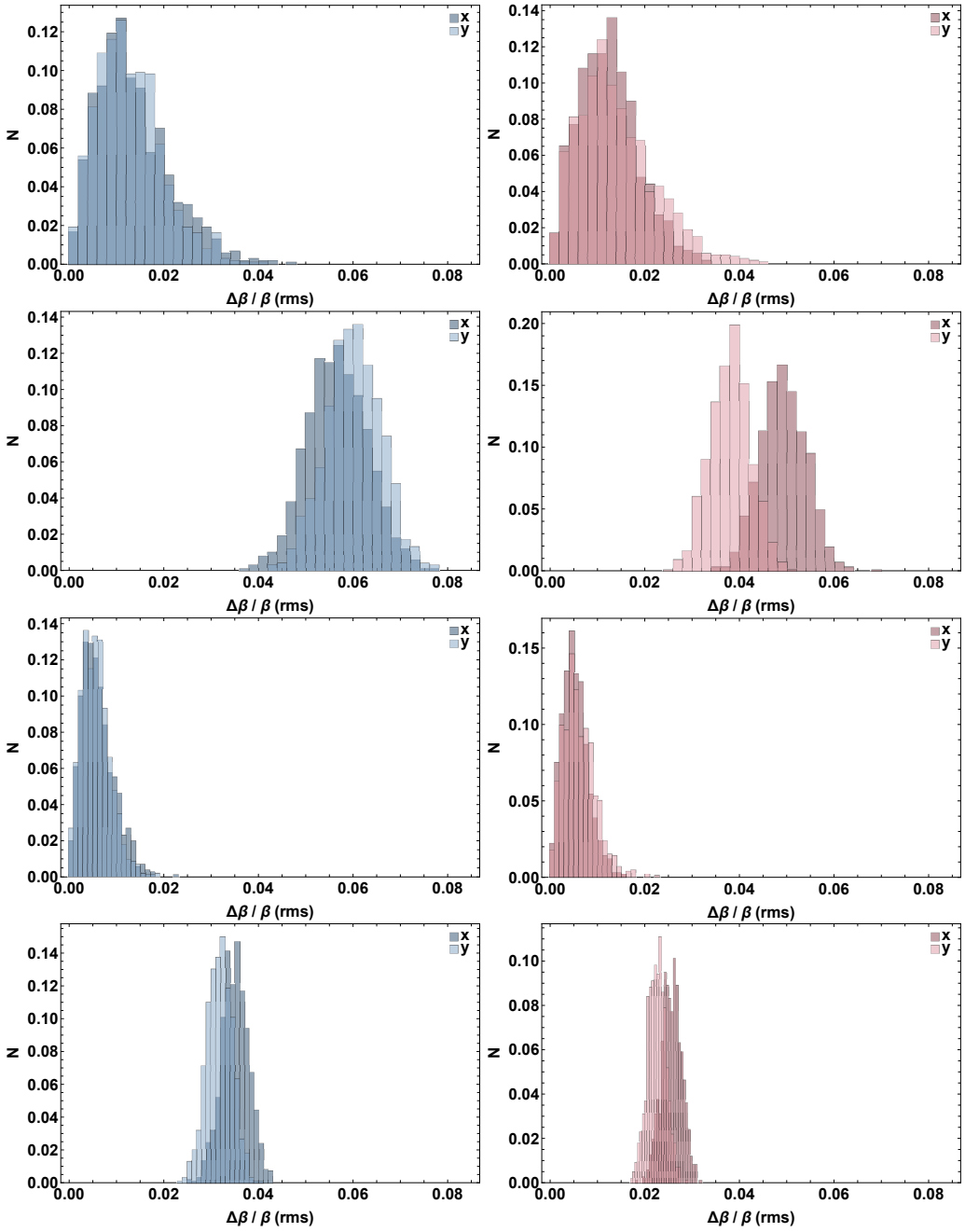

Figure 7: RMS β-beating generated by the b_2 (first row), b_3 component (second row), b_2 with FRAS (third row), and b_3 with FRAS of the MCBXF corrector magnets at $\beta^* = 15$ cm. Horizontal and vertical values are shown in each plot, while Beam 1 and Beam 2 results are reported in the first and second column, respectively.

Table 2: b_2, b_3, and a_3 field errors in IR1 and IR5 dipoles (D1 and D2) and orbit corrector (MCBXF) in 10^{-4} units with their corresponding reference radius.

		Systematic	Uncertainty	Random	Reference field [T m]	Reference radius [mm]
	MCBXFA	0	0	2.887	4.5	50
	MCBXFB	0	0	2.887	2.5	50
b_2	D1	0	0.2	0.2	35.08	50
	D2	1	1	1	35.08	35
	MCBRD	0	0	1.732	5	35
	MCBXFA	-16.65	0	2.887	4.5	50
	MCBXFB	17.37	0	2.887	2.5	50
b_3	D1	-0.9	0.727	0.727	35.08	50
	D2	1	1.667	1.667	35.08	35
	MCBRD	-10	0	0	5	35
	MCBXFA	20.12	0	2.887	4.5	50
	MCBXFB	-10.33	0	2.887	2.5	50
a_3	D1	0	0.282	0.282	35.08	50
	D2	0	0.282	0.282	35.08	35
	MCBRD	10	0	0	5	35

to be under control, at least for an ideal FRAS operation.

During the first years of operation of the HL-LHC, with β^* of 0.3 m and crossing angle of 380 µrad, the β-beating due to the MCBXF field imperfections will be more than a factor 2 lower. The impact on DA has also been verified for this scenario and has been shown not to be an issue either [37].

The impact of the MCBRD on the β-beating, due to b_2, is small and is reported in Fig. 8. Furthermore, the β-beating generated by the feed down from b_3 is completely negligible, due to the small amplitude of the orbit bumps in these magnets.

2.4 11 T dipoles

In previous HL-LHC baseline scenarios four 11 T dipoles made with Nb_3Sn, named MBH, were considered to replace two Nb-Ti dipoles in the IR7 dispersion suppressors for both beams. These magnets feature about 12 units of quadrupolar component at a reference radius of 17 mm at top energy [38], generating a vertical and horizontal peak β-beating of 5% and 1%, respectively (in both beams). Most of this β-beating can be locally corrected with the MQTLI.8 quadrupoles, left and right of IR7. The 11 T dipoles were recently descoped from the HL-LHC project, yet they could be again considered in the future.

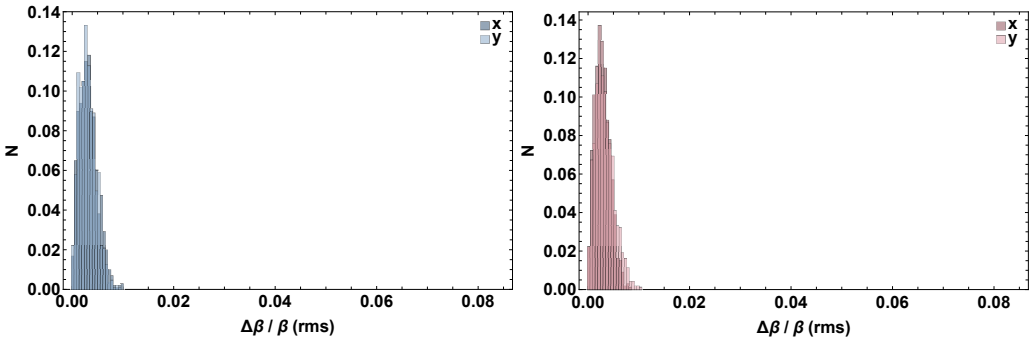

Figure 8: RMS β-beating generated by the b_2 component of the MCBRD corrector magnets. Horizontal and vertical values are shown in each plot, while Beam 1 and Beam 2 results are reported in the first and second column, respectively.

2.5 High order IR correctors

Concerning the magnets in the corrector package, a tolerance on their transverse offset of ± 1 mm has been specified based on DA calculations [39].

2.6 Hollow electron lens

The Hollow Electron Lens (HEL) is an advanced tool for active control of diffusion speed of halo particles. In HL-LHC, the hollow electron beam will be placed in IR4, featuring an inner radius smaller than the primary collimator setting for a controlled depletion of beam tails. The electron beam requires solenoid fields over a length of about 3 m with a peak field of 5 T. This field introduces an almost negligible amount of transverse linear coupling in the main proton beams of about $\Delta Q_{\min} = 2 \times 10^{-4}$ at injection energy [40]. The HEL will not need dedicated local optics control as the aimed β-beating of 20% is sufficient [41]. The HEL has recently been descoped from the HL-LHC project, nevertheless it is still considered for Run 5.

2.7 Beam Position Monitors

The Beam Position Monitors (BPMs) are the key instruments to measure the optics around the ring. Detailed tolerances for the HL-LHC BPMs are given in [42]. It is assumed that the BPM resolution in turn-by-turn mode with a pilot bunch (10^{10} p) in the HL-LHC era will not exceed 0.1 mm (which is approximately the current value in the LHC).

The rms calibration error of the BPMs in the HL-LHC IRs should not exceed the 0.8% level to allow using amplitude information in the measurement of

β-functions. If beam-based calibration is also considered, as presented in Section 5.6, up to 1.6% rms calibration error might be tolerated in the IR BPMs [43].

In LHC, the DOROS BPMs feature a resolution of about 0.015 mm in turn-by-turn mode for pilot bunches, allowing to measure the β-function at the position of the waist in the IR, β_w, with an uncertainty below 2% [44]. The same BPM resolution of 0.015 mm is sufficient to measure β_w with 2% uncertainty in HL-LHC. This technique is complementary to K-Modulation in the measurement of β_w. The longitudinal location of the betatron waist is best measured with luminosity scans (see Section 5.4).

2.8 Amplitude detuning

Figure 9 shows the predicted amplitude detuning generated in the low-β IRs of the HL-LHC (v1.4 with the target error tables) at $\beta^* = 0.4$ m and with a flat-orbit. A β^* of 0.4 m is considered since it represents the optics at start of collision in ultimate HL-LHC scenarios in the absence of any cryogenic limitations, and can also be directly compared to $\beta^* = 0.4$ m configurations studied in the LHC. IR generated first order detuning scales with $(\beta^*)^{-2}$. A histogram is shown for the direct horizontal detuning term over the 60 WISE seeds. The magnitude of detuning anticipated for the horizontal term is representative of all three detuning coefficients, and is expressed in terms of the detuning coefficient (left) and the equivalent Landau octupole current required to generate the same detuning at the flattop with an ATS factor of 1 (right).

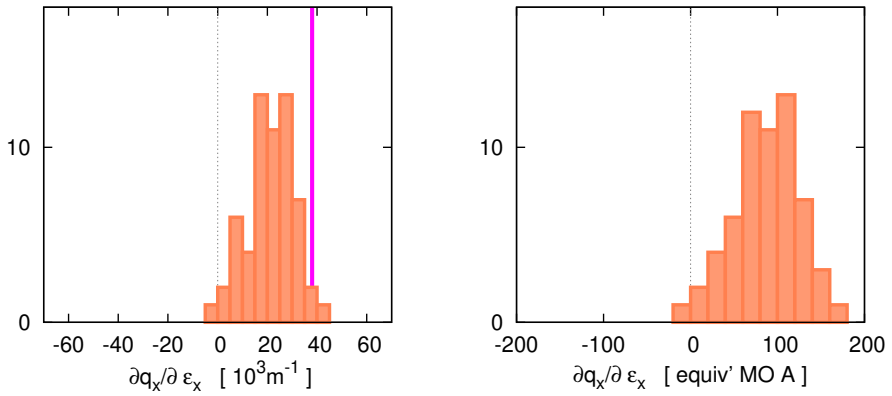

Figure 9: Predicted horizontal amplitude detuning generated in the HL-LHC low-β IRs at $\beta^* = 0.4$ m, flat-orbit. The LHC measured value at the same β^* is shown as a vertical purple line on the left plot.

Amplitude detuning generated by nonlinear errors can elicit a variety of effects, detrimental to both commissioning and operation. The detuning generated

by errors can potentially cancel that introduced by Landau octupoles during operation, effectively reducing the MO power available to stabilise the beams, which could become detrimental to stability of non-colliding beams. During optics commissioning, Landau octupoles are depowered, however detuning generated by errors can still be detrimental to beam instrumentation, for example to online tune measurement with the base-band tune meter (BBQ) or beam losses upon AC-dipole excitation. Consequently, amplitude detuning can also impede the commissioning effort (particularly where techniques such as K-Modulation are employed). In the LHC, the correction of normal octupole errors was of significant benefit to the measurement and correction of the linear optics [45]. Specifically, benefits to commissioning in the LHC were obtained following correction of detuning at the level of $40 \times 10^3\,\mathrm{m}^{-1}$. This value is indicated as the purple line on Fig. 9 (left). As evident from Fig. 9, the predicted detuning in HL-LHC can reach a level that had clear relevance to the viability of LHC linear optics commissioning by $\beta^* \approx 0.4\,\mathrm{m}$. Commissioning to $\beta^* = 0.4\,\mathrm{m}$ is currently foreseen in the initial years of HL-LHC operation, as such octupole corrections in the low-β IRs to minimise the detuning at flat-orbit should be anticipated for inclusion in the first round of HL-LHC commissioning. Techniques for octupole correction are well established in the LHC and are further discussed in Sec. 8.

An additional complication arises due to the feed-down of higher-order errors to normal octupole when the crossing scheme is applied. Figure 10 shows predictions of the change to amplitude detuning generated by feed-down upon introduction of a 380 µrad full crossing angle in IR1 and IR5 at $\beta^* = 0.4\,\mathrm{m}$. All three first-order detuning coefficients are shown, and units are expressed in terms of the equivalent Landau octupole current necessary to generate the same shift to detuning at flattop. Dodecapole errors in the triplets are taken to have a systematic $b_6 = -4$ units together with a random component of 1 unit. This represents a pessimistic scenario for the systematic b_6 error based on early magnet designs.

From Fig. 10 it is seen that the decapole and dodecapole errors are also capable of introducing a significant amplitude detuning, comparable to that generated directly by the b_4 errors at flat orbit. As such, some detrimental impact may be anticipated for the linear optics commissioning and to BBQ performance, however this will be constrained to circumstances where the crossing scheme is applied (such as for reiteration of linear optics corrections in the operational scheme to account for sextupole feed-down). Consequently, correction of the decapole and dodecapole errors is less critical to the early HL-LHC commissioning effort than the normal octupole corrections. With regard to operation in the initial years of the HL-LHC, collisions are currently planned to start with β^* of about 0.6 m. Considering a worst case detuning scenario equivalent to 250 A at $\beta^* = 0.4\,\mathrm{m}$ due to feed-down, this would scale with $(\beta^*)^{-2}$ to give an equivalent detuning of 110 A at $\beta^* = 0.6\,\mathrm{m}$. This value is within the available Landau octupole margin for

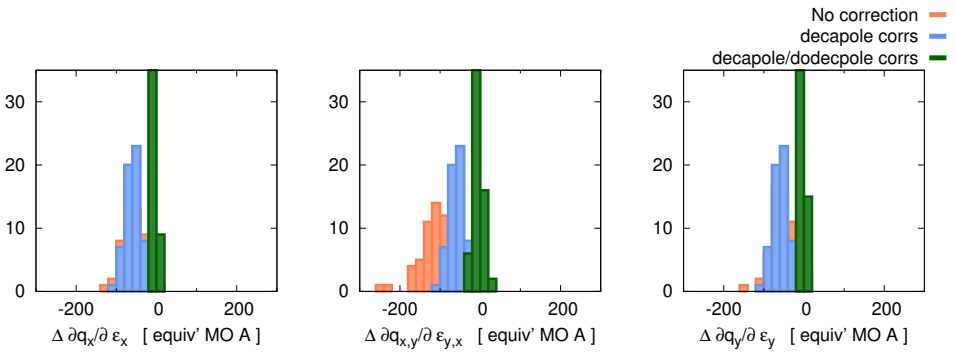

Figure 10: Predicted shift to detuning, generated upon introduction of a 380 µrad crossing-scheme in IR1 and IR5 at $\beta^* = 0.4$ m.

the expected HL-LHC beam-intensities in the initial years (up to 1.8×10^{11} ppb). Thus, correction of decapole and dodecapole nonlinearities does not at present appear essential to HL-LHC commissioning and operation in the first years [46]. Nevertheless, it is noteworthy that successful dodecapole correction, based on feed-down to amplitude detuning, has already been executed in the LHC [47], thereby affirming the feasibility of such correction. As the HL-LHC progresses to larger bunch intensities and smaller β^* correction of the high-order errors is expected to become critical to both the commissioning and operation.

2.8.1 Amplitude detuning from IR misalignments

Misalignment studies of triplets and nonlinear correctors at $\beta^* = 30$ cm have shown that misalignments within the required tolerances as given in Section 2.1 and Section 2.5 have minor influence on amplitude detuning [48, 49]. In these studies, the decapole and dodecapole field errors were applied to the triplets and D1 and the correctors powered to locally correct the nonlinearities [24]. Magnetic errors were taken from the WISE tables from 2015 for 6.5 TeV [50] to be used in the IP2 and IP8 magnets. In IP1 and IP5, the error tables for the MQXF (v5 [52]) and D1 (v1 [53]) were used. For each of 60 different WISE error realisations 50 random realisations of misalignments were chosen. A uniform distribution of misalignments between ± 1 mm was chosen for the correctors, while a truncated Gaussian distribution with rms at 0.4 mm and a cutoff at 1 mm was used for the triplets, based on the tolerance values in [30, 39] and mentioned above. Amplitude detuning was calculated from these misalignments via feed-down to b_4. It was found, as presented in [48] and [49], that the standard deviation on amplitude detuning introduced by the expected misalignments is equivalent to less than a 4 A powering of the Landau octupoles. Therefore these results instil confidence that

the amplitude detuning created by triplet and nonlinear corrector misalignments are tolerable.

3 General strategy

The optics commissioning steps in the first year of HL-LHC follow:

1. Beam-based magnet polarity checks of all HL-LHC magnets at injection energy. A summary of polarity checks performed for LHC in Run 1 can be found in [54].
2. Beam-based measurement of BPM calibrations with the ballistic optics (see Section 5.6).
3. Global linear-coupling corrections are needed to be applied in an iterative manner throughout the commissioning. The first corrections will be applied before the local linear-coupling corrections since a large global linear coupling might prevent sufficient tune control and has a negative impact on measurements. After the local linear-coupling correction, a refinement of the settings of the linear-coupling knobs is needed. The global linear coupling should then be corrected for most matched points in order not to deteriorate the quality of other measurements and to reach the requirement for the ΔQ_{min}, described in Section 7.
4. Optics measurements throughout the machine cycle with flat orbit and without quadrupolar corrections. This ensures an accurate assessment of the quadrupolar errors (normal and skew) of the new magnets (see Sections 5 and 7). β-beating could reach up to 150% at $\beta^* = 30$ cm, as shown in Fig. 2. During Run 1, these measurements served to find quadrupole gradient non-conformities above the 1% level [55, 56]. Note that the expected MBH quadrupolar component could be verified with optics measurements at this point (see Section 2.4).
5. Local linear-coupling corrections in IR1, IR2, IR5, and IR8 based on the measurement of linear-coupling Resonance Driving Terms (RDTs) and the rigid waist shift correction method (explained in Section 7).
6. At this point, it might be possible to power the nonlinear IR corrections according to the predictions based on magnetic measurements and alignment data. This might be particularly useful if they demonstrate improved tune-measurement resolution and reduced losses when exciting the beam with AC dipoles. Accurate beam-based nonlinear corrections should only be performed in later steps.

7. Accurate local corrections in IR1, IR5 and IR8 should bring β-beating down to about 20% at top energy and along the energy ramp. Dedicated global corrections will be needed at injection energy to bring the β-beating to 20% or below, as shown in Fig. 11 for the Run 2 ATS optics. Details of the injection optics commissioning in 2021 and 2022 are given in [57]. A new injection optics was developed in 2023 to minimize octupolar resonances [58].
8. At this point (β-beating $\lesssim 20\%$), it should be possible to use 3 pilot bunches for AC dipole measurements [59] to speed up optics commissioning, in particular through the energy ramp. Furthermore, the use of 3 bunches during the energy ramp removes the errors introduced from possible timing errors and from combining measurements from different ramps [60].
9. 3D excitation, i.e. AC dipole kicks together with RF phase modulation, will also significantly speed up the measurement of dispersion and other chromatic properties [61].
10. Preliminary measurements of nonlinear lattice properties such as tune change versus crossing angle and amplitude detuning can take place to compare with magnetic-model predictions, possibly in combination with preliminary aperture measurements (see Section 3.2).
11. Crossing angles and dispersion correction bumps are incorporated in the machine. Both BPM and K-Modulation measurements will serve to determine crossing angles with accuracy below 5% (see Sections 5.3 and [31]).
12. Precise K-Modulation measurements and luminosity scans should be performed to allow for accurate global and local optics corrections including β^*, coupling and dispersion (see Sections 5.1, 5.4, and 7). Special attention should be put at the minimum β^* optics to guarantee a β^*-beating below 2.5% and IP dispersion below 7 mm.
13. The FRAS system could be used at this stage of commissioning to rigidly re-align all components from Q5 left to Q5 right according to the offsets seen in the inner tracker [62].
14. Beam-based nonlinear corrections for sextupolar and octupolar effects should be implemented as described in Section 8.
15. Another iteration of point 12, linear optics correction, might be required due to the feed-down from the changes in the FRAS and the nonlinear corrector settings together with the IR crossing angles. Figure 4 (Sec. 2.1) presents simulations of peak β-beat due to such residual feed-down after sextupole and octupole correction of up to 5 % at $\beta^* = 0.15\,\mathrm{m}$. At higher β^* residual β-beat will be less significant, scaling with $\approx \frac{1}{\beta^*}$, however correction may still be desirable to maintain consistent β^* between ATLAS and CMS.

16. Decapolar and dodecapolar beam-based corrections, as presented in Section 10, are postponed for later years, as it is expected that a large number of shifts will be required, see Section 10. Even without powering the IR dodecapolar correctors a DA above the target of 6 σ is found at β^*= 30 cm, see Fig. 12.
17. If the feed-down from uncorrected decapolar and dodecapolar errors and crossing angle to amplitude detuning is an obstacle for commissioning or operation further octupolar corrections should be implemented with IR and Landau octupoles.

Optics commissioning for $\beta^* < 30$ cm could take place during MDs in the first year and in the commissioning period of following years. This will require decapole and dodecapole corrections and the operational deployment of the 2D field quality model of the MCBXF orbit correctors. Interleaving linear corrections and nonlinear will be required.

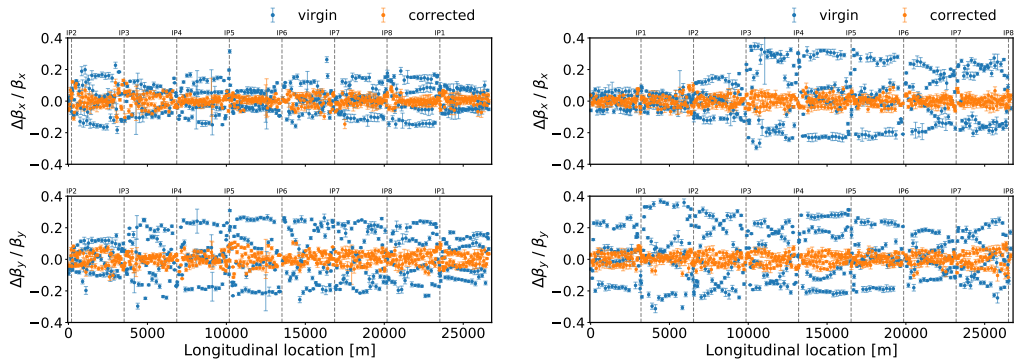

Figure 11: Measured β-beating for ATS optics at injection of virgin machine and after beam-based corrections: Beam 1 (left) and Beam 2 (right).

3.1 3D beam excitation

3D beam excitation is a combination of transverse excitation driven by AC-dipoles and longitudinal excitation by RF system modulation in an adiabatic fashion [63]. It will significantly speed up the measurements whenever dispersion or other chromatic properties need to be measured, in addition to on-momentum linear optics. This is the case, especially when global corrections are to be calculated or verified. The 3D excitation comes in two flavours:

- Excitation by means of AC dipoles together with slow (5 Hz) RF-frequency modulation was well established during Run 2 [64]. It allows for precise

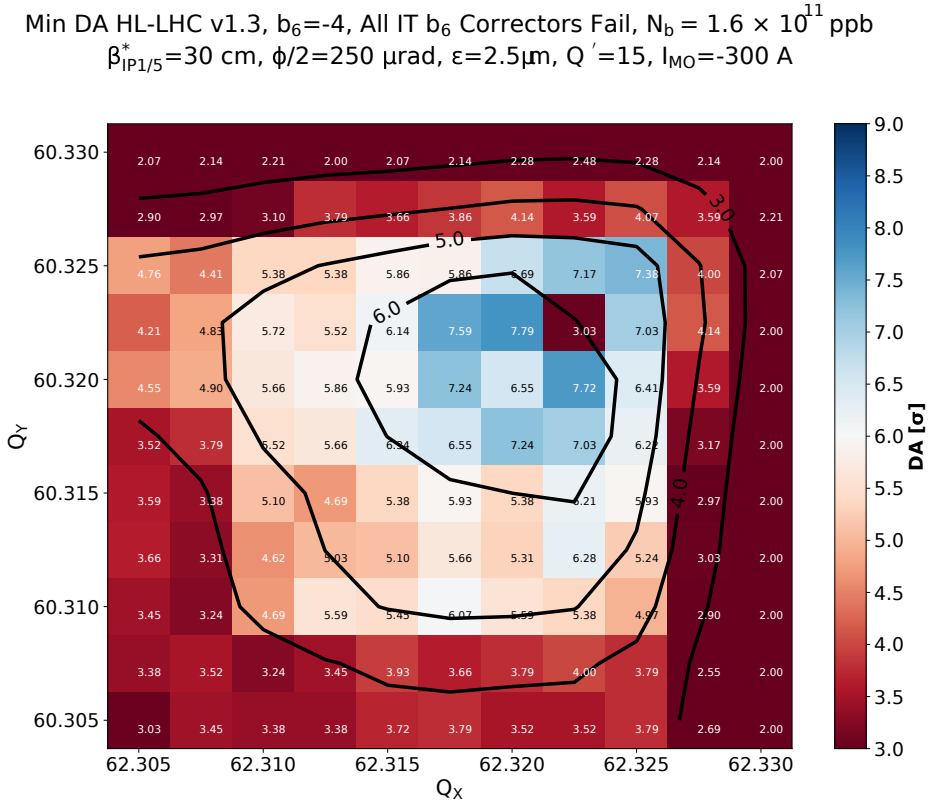

Figure 12: Dynamic aperture versus tunes without the triplet b_6 correction, at $\beta^* = 30$ cm and including beam-beam interaction. Dynamic aperture above the 6 σ is achieved allowing to start HL-LHC with this configuration.

measurement of dispersion simultaneously with linear optics in a static configuration as well as during the energy ramp [65], which would be otherwise impractical. Due to the small separation between longitudinal sidebands in the frequency spectra, chromaticity and chromatic beating are not measured with sufficient accuracy, unless the AC-dipole excitation plateau would be extended to about 2×10^4 turns.

- Fully forced 3D excitation, i.e. by means of AC dipoles and RF-phase modulation close to the synchrotron tune, where the driven frequency needs to be higher than the central synchrotron frequency [61]. This type of excitation is suitable also to measure other chromatic properties, i.e. chromatic β-beating and chromatic coupling. Thus far, it has been utilised only at injection energy and will need to be commissioned at top energy and during the energy ramp.

We expect to gain more experience with both types of 3D excitation throughout Run 3.

3.2 Combining optics and aperture measurements using AC dipoles

Global aperture measurements are crucial for safe operation and to push the ring's performance. In particular, the knowledge of the global aperture at top energy allows pushing the optics to reduce the colliding beam sizes [66]. The standard LHC aperture measurement technique consists in performing a gentle blow-up of one pilot bunch with the transverse damper (ADT) until losses are measured at a reference collimator location by the beam loss monitor system (BLMs). Usually, at top energy the tertiary collimators (TCTs), the closest ones to the aperture bottleneck typically located at the triplets, are used as reference collimators, while at injection energy the primary collimators (TCPs) are used. Then, the gap of the reference collimator is opened in steps of 0.5 σ until the losses move from the collimator to the location of the aperture bottleneck [67, 68]. This method requires the use of several low-intensity bunches for just a single measurement and makes the bunches un-usable for other activities. Note that to not interfere with the measurements, all other collimators need to be more opened than the reference one and the aperture bottleneck. Because of that, some selected collimators are kept within a certain margin with respect to the reference one for the sake of protection reasons while the others are fully retracted.

A new method to identify the location of the bottleneck and measure the aperture using the AC dipoles has been explored in 2017 and 2018 [69, 70, 71]. This method consists in exciting large coherent oscillations of the beam with the AC dipole, thus preserving the transverse emittances, and then proceed with the reference collimator scan as done in the ADT method. This method is non-destructive and enables re-using the bunches for other activities. In particular, this novel approach can be combined with optics measurements, thus saving commissioning time and enabling optics measurements to be carried out with the highest possible beam orbit amplitude, thus increasing their precision.

During 2017, global aperture measurements were performed at injection energy for Beam 1 in the horizontal plane (all details and analysis can be found in [72, 73]). In addition, during 2018, measurements were performed also at injection energy for Beam 2 to explore the effect of the AC dipole tune and of the beam chromaticity on aperture measurements [74]. Measurements performed with the AC dipole were compared with the results obtained by the standard ADT method, and in all cases considered the location of the aperture bottleneck identified was the same. Moreover, the corresponding value of the measured aperture was in good agreement within the estimated errors provided by the scan collimator step and the computed β-beating induced by the AC dipole [75]. No significant effect

on the results was observed from the change of the AC dipole tune and the beam chromaticity in the ranges studied.

The new method was also tested at flat-top energy in 2017. Global aperture measurements were performed for Beam 1 and Beam 2 both in the horizontal and vertical planes for colliding β^*=30 cm optics. In Fig. 13 the measured BLM signal at the TCP used as the reference collimator for the scan (in blue) and at the expected bottleneck elements in IR5 and IR1 (in red and green, respectively) are shown as a function of the TCP half gap in units σ. The corresponding half gap at which the TCP and the bottleneck curves cross corresponds to the aperture bottleneck in units of σ. Good agreement is found when comparing the horizontal results with the measurements performed with the ADT method compiled in [76]. However, in the vertical plane discrepancies up to 1-1.5 σ were observed [77]. The analysis of the vertical aperture measurements data revealed that, during the vertical plane measurements, the AC dipole was kicking to high amplitudes in both the vertical and horizontal planes. Because of that, the origin of the observed losses can not be associated with a certain transverse plane and the results cannot be directly compared to what was obtained with the ADT method. This situation has to be avoided in the future.

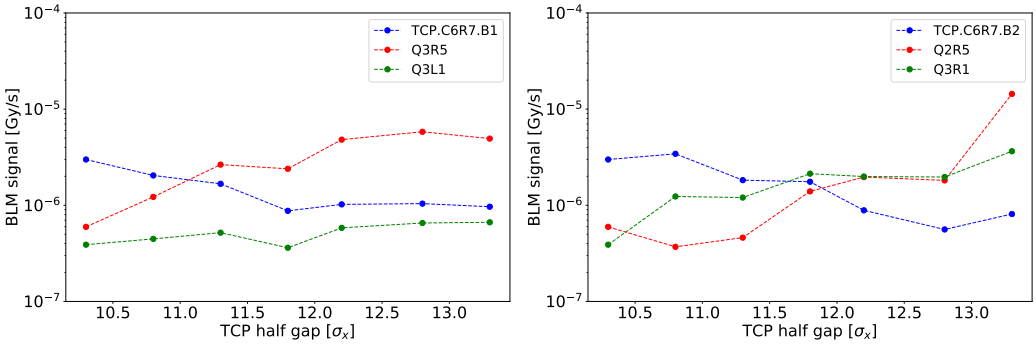

Figure 13: Horizontal Beam 1 (left) and Beam 2 (right) aperture measurements for the 2017 colliding optics with β^*=30 cm. The BLM signal as a function of the TCP half-gap at the TCP (blue) and at the locations where losses were observed in IR5 (red) and IR1 (green) are shown.

Beam measurements were performed with both the standard and the AC dipole methods, at top energy for Beam 2 in both planes during the 2018 LHC commissioning period. These measurements were performed for the colliding beam optics with β^*=25 cm using the TCTs as reference collimators. While very good agreement between the methods was obtained in the vertical plane, in the horizontal one the highest loss spike found when performing the measurements with the AC dipole was at the element Q5R5 and not at the triplet as expected. Figure 14

shows the BLM signal measured at different locations during the collimator scan performed with the ADT (left) and the AC dipole (right). Measurements with different techniques were performed within one hour. The Q5R5 magnet is not expected to be the bottleneck and no losses were observed at this element during the aperture measurements performed with the ADT method as can be seen in Fig. 14. The linear coupling measured during these tests was about 3.8×10^{-3} being higher than expected. In addition, the smallest β^* optics was used for the measurements. Because of that, the possible effect on the measurements from the linear coupling combined with nonlinearities in the IRs was investigated. However, preliminary multi-particle tracking simulations performed with MAD-X do not show any impact on the location of the aperture bottleneck. Hence, further investigations are needed to explain the observations.

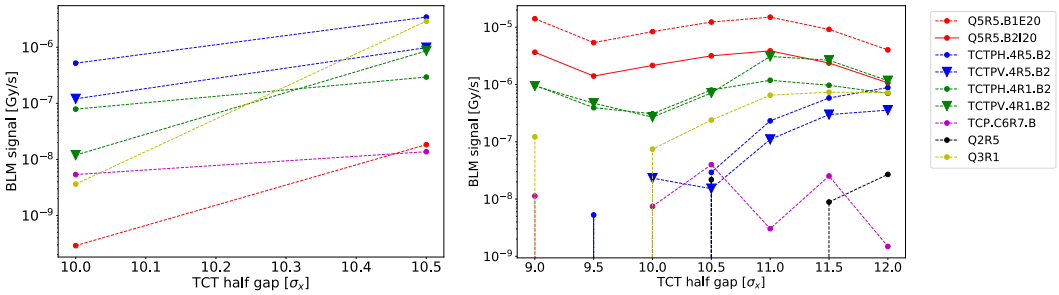

Figure 14: Losses for Beam 2 observed during the ADT (left) and AC dipole (right) horizontal aperture measurements for the 2018 commissioning with the colliding β^*=25 cm optics. Note that missing elements data on the right plot means no measured losses at these locations.

Results are promising and the new method offers a way to explore aperture limitations during or before optics measurements to detect possible issues early on. The new method has demonstrated good performance for injection energy for both beams and both planes. At top energy, good results were obtained for $\beta^* = 30$ cm optics in the horizontal plane and for the $\beta^* = 25$ cm optics in the vertical plane [77]. The issue found for $\beta^* = 25$ cm optics in the horizontal plane requires further understanding. Experimental tests will continue in Run 3 to solve the open points and further exploit the potential of this method.

4 Data processing

The main workhorse of the optics measurements is the analysis of BPM orbit readings of coherently-excited beams recorded turn-by-turn. The calculations of the actual optical functions are the last steps in the analyses and are often depend-

ing on the lattice model. In this chapter, we describe the initial data processing and analysis steps, whose algorithms are independent of the lattice model. Identification of faulty BPMs is a major concern as the computed optics corrections can be severely affected by these artefacts. Most of the faulty signals can be removed using predefined thresholds, as well as by applying advanced cleaning and noise-reduction techniques based on Singular Value Decomposition (SVD) [78] (see Section 4.2). The BPM data are Fourier-analysed (see Section 4.3) to use amplitude and phase of the different spectral lines for the computation of lattice functions. At this stage, new faulty BPMs are identified based on tune measurements [79], i.e. tune values that are far from the tune measured by the rest of BPMs. Since a few remaining faulty BPMs could still be observed in the data after applying these methods, a novel technique to identify faulty BPMs using Machine Learning was successfully introduced in 2018 LHC operation (see Section 4.4). Note that the Optics Measurement and Correction (OMC) software has evolved over many years [80, 81, 82, 83] to follow the progress made in the data treatment.

4.1 Pre-processing

At first, the range of turns is selected, and optionally the data are rescaled (the orbit unit differs in measurement and simulation). BPM signals exhibiting too low or too high signal variations are discarded, similarly to BPM signals containing exact zeros, as these generally originate as a replacement value for nonphysical readings in the acquisition. In order to synchronise the acquired turn-by-turn data with the model, some of the BPM signals are shifted by one turn with respect to the others. This way, the first BPM in the measurement is the first in the model.

4.2 SVD-cleaning

All the BPMs observe the same beam oscillations, which grants large correlations between the different BPM signals. BPM signals containing substantial uncorrelated modes are identified as potentially malfunctioning BPMs. The BPM noise is reduced based on SVD techniques [78].

For each of the two planes, the turn-by-turn data matrix $\mathbf{A}$ is decomposed as $\mathbf{A} = \mathbf{USV^T}$, where columns of the $\mathbf{U}$ and $\mathbf{V}$ matrices are orthonormal vectors. The columns of $\mathbf{V}$ are being called "modes" in the following. $\mathbf{S}$ is a diagonal matrix with non-negative elements, the singular values, sorted in decreasing order. The following holds for elements a_{ij} of $\mathbf{A}$ with i and j indexing BPMs and turns, respectively:

$$a_{ij} = \sum_{k,l=1}^{min(i,j)} u_{ik} s_{kl} v_{jl} \,, \tag{1}$$

where

$$\sum_{i}^{N_{\mathrm{BPM}}} u_{ik}^2 = 1 \,, \tag{2}$$

N_{BPM} being the number of BPMs. Note that it is of utmost importance to subtract the closed orbit before SVD calculation to avoid these offset signals to appear as, or pollute, singular modes. SVD cleaning refers to two distinct mechanisms of data processing. The first concerns the reduction of BPM noise by removing the weakest singular modes by recomposing $\mathbf{A}$ using only the first n modes with largest singular values, typically n=12 in the LHC, i.e.

$$a_{ij} = \sum_{k,l=1}^{n} u_{ik} s_{kl} v_{jl} \,. \tag{3}$$

The amplitude of the removed signals can be interpreted as a noise floor that depends on the BPM hardware, beam parameters, and the actual choice of n. Rms of the difference between raw and cleaned data estimates the BPM resolution. The second mechanism aims at removing faulty BPMs by assuming that BPMs with a signal mostly uncorrelated with other BPMs are faulty. Over time, there were a few ways to identify faulty BPMs:

- For each k, the BPM i with largest $|u_{ik}|$ is faulty if $|u_{ik}| > svd\_cut$. This was used for the analyses of the LHC data until 2016.
- For each k, the BPM i with largest $|u_{ik}|$ is faulty if $\sqrt{\sum_L u_{i'k}^2} > svd\_cut$, where the sum runs over the set L of 2 to 5 largest $u_{i'k}^2$ [78].
- For each $k \leq n$, all BPMs with $|u_{ik}| > svd\_cut$ are faulty. This was used in the LHC since 2017.

The first and third approaches are equivalent if $svd\_cut > 1/\sqrt{2}$ since, because of Eq. (2), it is not possible for 2 BPMs to fulfill the condition. For a lower svd_cut the newer approach (the third) may remove multiple BPMs per mode, while the other two approaches remove at most one BPM per mode. In the ideal configuration of linear uncoupled betatron oscillations with noiseless BPMs, the SVD decomposition would have 2 singular modes with largest $|u_{ik}|$ defined as $\hat{u}$. Assuming that the BPMs are uniformly distributed over the betatron phases, $\hat{u}$ is bounded as

$$\hat{u} \lesssim \sqrt{\frac{2}{N_{\mathrm{BPM}}} \frac{\hat{\beta}}{\overline{\beta}}} \,,$$

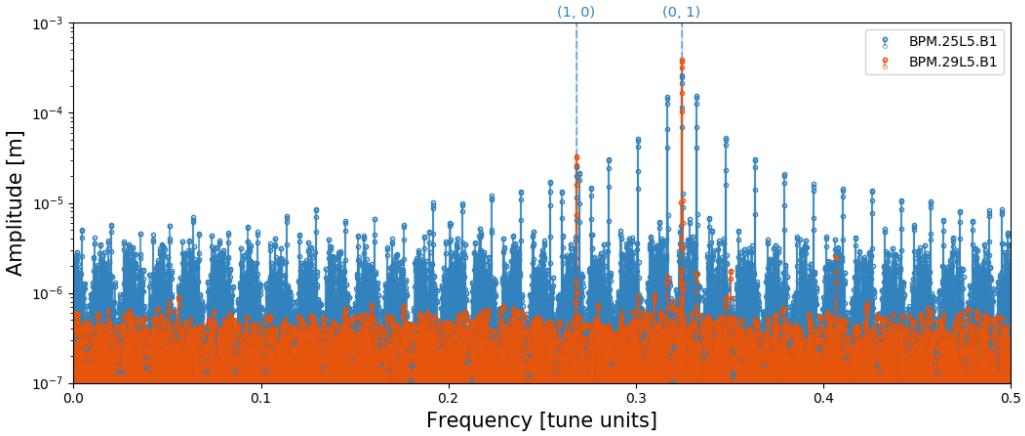

Figure 15: Frequency spectra of a faulty BPM (blue) compared to a good BPM (orange). This BPM has passed through the iterative SVD cleaning because the same pattern has appeared in multiple other BPMs distributed around the machine circumference. The highest sidebands are at a distance of $4Q_s$ from the main spectral line, and the noise level is about an order of magnitude higher than for a normal BPM. Such behaviour has not been explained yet.

where $\hat{\beta}$ and $\overline{\beta}$ are the actual machine peak and average β-functions at BPMs, respectively. This relation has been checked in simulations. For HL-LHC, with about 500 BPMs, the upper bound of $\hat{u}$ would be in the range between 0.14 and 0.33 for injection and collision optics, respectively.

Other than the beam itself, the electronic crates of the BPMs were suspected to give rise to correlations between different BPM signals, however this has not been observed. In some cases, several BPMs distributed around the machine circumference show a similar pattern. Figure 15 shows two frequency spectra to showcase the different behaviour [84]. Neither the source nor the connection between these BPMs has been identified yet.

4.2.1 Iterative SVD cleaning

In any of the above-mentioned approaches, the removal of a faulty BPM effectively reduces the singular value corresponding to the given mode, which consequently may not remain amongst the largest modes and therefore reduces the "effective" n. Another BPM may also constitute most of the remnant of the given mode, while not being removed. The modes in which a faulty BPM was identified should be re-normalised, therefore potentially changing the set of largest modes. A new cleaning method has been developed, which simulates the removal of $\mathbf{U}$ matrix elements, re-normalises the $\mathbf{U}$ matrix columns and adapts the singular val-

ues. This may be performed as an iterative process, which currently runs in up to 3 iterations [84]. At each iteration, the algorithm is as follows:

- For each k, the **U** matrix element with largest $|u_{ik}|$ is replaced with zero if $|u_{ik}| > svd\_cut$.
- For each k, all **U** matrix elements u_{ik} and the corresponding singular value s_k are renormalised, i.e. the elements u_{ik} are divided by $\sqrt{\sum_i^{N_{\mathrm{BPM}}} u_{ik}^2}$ and the corresponding singular value s_k is multiplied by $\sqrt{\sum_i^{N_{\mathrm{BPM}}} u_{ik}^2}$.

The modes corresponding to the n largest singular values are used for turn-by-turn data re-composition. A BPM i is considered faulty, and therefore removed, if any u_{ik} for k up to the index of the nth largest singular value has been replaced with zero. In case of multiple iterations, it is good to keep in mind the minimal relative difference between the two largest $|u_{ik}|$. For instance, applying $svd\_cut > 0.8$ guarantees that the second largest $|u_{ik}|$ has a maximum value of $\sqrt{1-0.8^2} = 0.6$ (Eq. (2)), i.e. at least 25% lower than the largest element.

4.3 Harmonic analysis

Once the analyses described in 4.1 have been performed, the BPM turn-by-turn data are aligned with the model in terms of the order of BPMs and turns, and the data are cleaned by SVD-based techniques. The next step is the frequency analysis and the identification of prominent spectral lines, i.e. beam-related harmonics. To avoid unnecessary errors in the frequency spectra, the closed orbits are subtracted first from the cleaned BPM signals. The actual frequency analysis algorithm has undergone significant developments since the start of LHC Run 2 and three distinct algorithms are still in use to date:

- The original algorithm SUSSIX [85] performs frequency interpolation (similar to NAFF [86]) of the strongest signal in the output of the Fast Fourier Transform (FFT), subtracts the interpolated strongest signal (after having performed a Gram-Schmidt orthonormalisation process), and repeats these steps typically 300 times resulting in a collection of the 300 strongest spectral lines. Such a spectrum is calculated for every BPM. The algorithm is computationally expensive, for the standard example of double-plane data containing 6600 turns of about 500 BPMs, the analysis takes about 30 seconds on 32 CPUs. The phase accuracy of SUSSIX was found to be slightly better than NAFF, but worse than FFT [87]. The phase advance measurement accuracy from SUSSIX was improved by using the average tune from all BPMs to compute the phase and amplitude of the main line for each BPM [88, 89]. Nevertheless, other unwanted features of SUSSIX have been observed:

  - A systematic pattern of measured tune variations around the machine was observed in data from ESRF with decoherence [90].
  - Non-monotonic phase accuracy as a function of the number of turns analysed [91], observed for simulations with high signal-to-noise ratio.
  - Inaccuracy in the determination of the weaker spectral lines (phase and/or amplitude) was observed in data from injection oscillations in the PS with low decoherence and significant tune swing, of about 10^{-3} during data acquisition [92, 91].

- The second algorithm [93, 79, 89] is similar, but differs in the frequency interpolation method (Jacobsen interpolation method with bias correction [94]), and more importantly, it uses SVD cleaning. In fact, it calculates the frequency spectra of the decomposed data (time-like singular vectors) and recomposes the BPM spectra in the frequency domain. This algorithm is more than an order of magnitude faster than SUSSIX and also more accurate for strong spectral lines. However, it does not solve the accuracy issues for weak spectral lines.

- The third algorithm, Harpy [95], successfully combines SVD with zero-padded FFT. The n modes (rows of $\mathbf{V^T}$ matrix) are padded with zeroes to the desired length, which translates into finer frequency sampling. The frequency spectrum of a given BPM can be computed as a linear combination of frequency spectra of the modes, which is not possible for the other two previous algorithms. It approaches the expected accuracy levels (without effect of spectral leakage) for phase and relative amplitude $\sigma_{\text{phase,rel\_amp}}$ of any given spectral line with amplitude $\mathcal{A}$, given by, e.g. [96, 87],

$$\sigma_{\text{phase,rel\_amp}} \approx \sqrt{\frac{2}{N_{\text{turns}}}} \frac{\sigma_{\text{orbit}}}{\mathcal{A}}, \tag{4}$$

  where σ_{orbit} is the resolution of the position measurements. This method is also an order of magnitude faster than SUSSIX. This algorithm has been implemented with a greater choice of windowing functions than the two presented above. The calculation time naturally scales with the requested precision (length of zero-padding), the number of singular modes, and the portion of frequency spectrum covered. There are also other effects playing a role: vectorisation, which increases the granularity of some of the parameters, and the speed of memory allocation. For the standard example of double-plane data containing 6600 turns from about 500 BPMs, cleaned using the 12 largest modes, and zero-padded to a length of about 2 million, the harmonic analysis takes about 2 seconds and covers about 6% of the frequency spectrum. While changing a single parameter at a time:

– Usage of 120 largest modes results in a 4 second-long calculation.
– Calculating and searching in 27% of spectrum takes about 7 seconds.
– Zero-padding to about 8 millions results in a 7 second-long calculation.

The phase accuracy of Harpy was found to be better than SUSSIX [97, 92] in simulations and in experimental data from ESRF and PS. However, no obvious difference is found in the measured errors of the phase advance between neighbouring BPMs in LHC data, as shown in Figure 16. Further studies of the phase advance accuracy and precision, may lead to a better understanding of errors in the LHC machine: the impact of the β-functions at BPM locations as well the BPM type's influence on the phase measurement error are being investigated. Results for standard BPMs can be seen in Fig. 17.

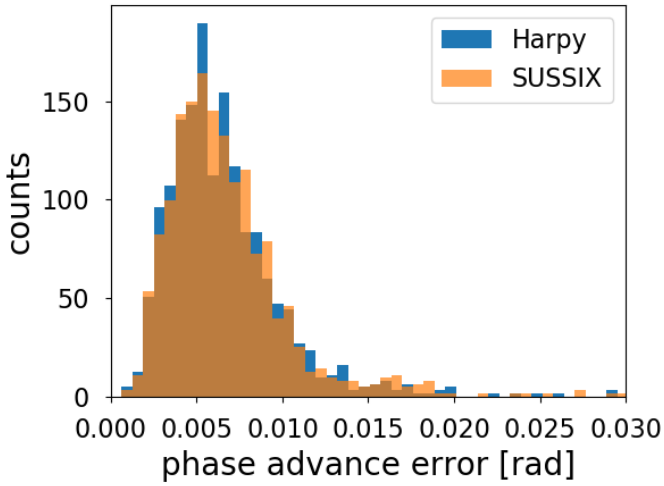

Figure 16: Histograms of measurement errors of phase advances between neighbouring BPMs in LHC ballistic optics were obtained from two different algorithms: SUSSIX and Harpy. The errors are similar, in spite of the expectation from simulations, which has not been explained yet.

Once the BPM frequency spectra are calculated, beam-related harmonics are found as the strongest lines in a given frequency interval around multiples of the driven betatron tunes. The betatron tune is a robust observable, and the same value is expected to be measured by all BPMs. The tails of the distribution of measured betatron tunes inconsistent with a sample of the normal distribution of a given size, i.e. betatron tunes too different from the average, are removed [79] from the corresponding BPM spectra. A limit stating the safe difference to the average can be set. Such type of automatic cleaning is also used in K-Modulation and amplitude detuning analyses.

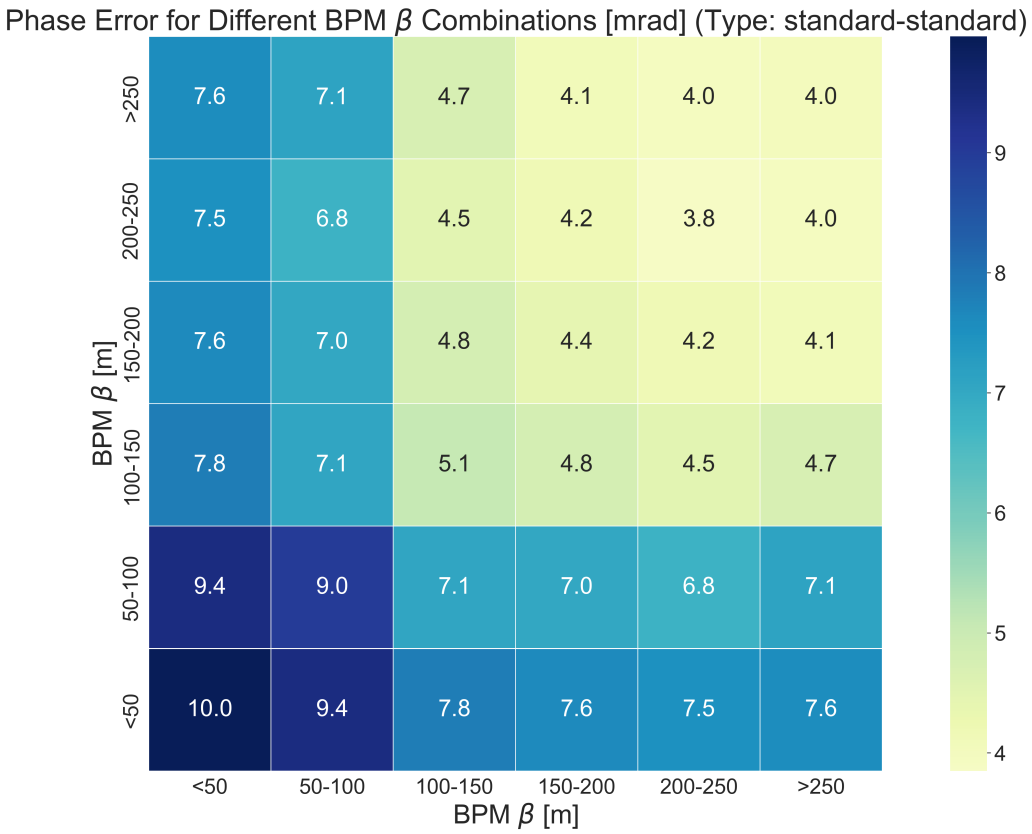

Figure 17: Computed standard deviation (in mrad) on phase measurement between standard BPMs for the LHC Run 2 (2018, $\beta^* = 30$ cm) for different β-functions combinations of BPMs.

4.4 Isolation Forest

Even after data cleaning as presented above, erroneous optics calculation can be observed at few locations hinting to the remaining faulty BPMs. Recently, we introduced Isolation Forest (IF) machine learning algorithm [98] as an additional cleaning technique to be applied on harmonic analysis data. IF is a decision-tree-based, unsupervised learning technique, applied to find anomalies by randomly splitting the given data until each point is isolated from the others. Fewer splits are needed to isolate an anomalous point. Hence, low numbers of splits indicate anomalies. The new technique has been used during LHC commissioning and MD sessions in 2018, complementing the previously-used cleaning tools efficiently, such that most of the remaining outliers could be detected by IF prior to optics computation.

The summarised results of the 10 measurements performed in 2018 are shown

in Fig. 18, demonstrating the improvements achieved by applying IF-based cleaning.

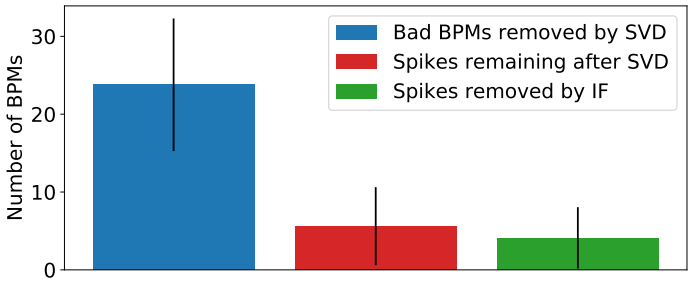

Figure 18: Summary of cleaning results and remaining outliers in β-beating and phase advance averaged over 10 measurements of Beam 1 and Beam 2 performed during commissioning and MDs in 2018.

The introduced methods have several setting parameters, which influence the efficiency of data cleaning. In the past, default SVD-cleaning settings obtained from the statistical analysis of RHIC BPMs [78] have been used and the contamination factor used in IF has been set to an empirically defined value. The contamination factor defines the expected proportion of outliers in the data and regulates the amount of BPMs to be cleaned in the harmonic analysis data.

A study on the simulated BPM faults [99] has been performed to verify the new IF algorithm and to investigate the relation between SVD and IF optimal thresholds. In the SVD-cleaning, the global noise reduction on all BPM signals is determined by the number of strongest modes to be kept during the decomposition. Using a small number of modes in SVD cleaning causes local linear-coupling information to be discarded as noise. According to the simulation study presented in [99], the number of strongest modes used for the LHC should be significantly increased, from the typical value of 12, to keep the signal needed for the correct computation of local linear coupling. The threshold used to remove BPMs that dominate the decomposition could be decreased from the previous default value 0.925 defined in [78] to somewhere above 0.4 (for LHC data) to identify more faulty BPMs with SVD. Nevertheless, it has been shown in simulations that simple cuts, together with SVD cleaning, do not succeed to identify all faulty BPMs. Changing the SVD default settings to the optimal values obtained from simulations, reduces the number of faulty BPMs remaining in the harmonic analysis data, which is used as input for the IF. Therefore, the contamination factor must be adjusted accordingly, with the range obtained from simulations being [0.01, 0.02]. IF has been found to complement these tools successfully and improve the cleaning results as demonstrated by both simulations and measurements data [99]. For the computation of optics corrections in the LHC, the existence of few bad mea-

surements is more penalising than the absence of few good BPMs. Nevertheless, in the future attention should be also paid to minimise the removal of good BPMs.

Cleaning of the BPMs related to the pattern in the spectra shown in Fig. 15 indicates the importance of adjusting the settings of the cleaning tools and the advantage of combining the traditional techniques with IF. There are 7 BPMs affected by this failure, 30% of which could be identified by lowering the SVD cut threshold to 0.6. One approach to remove all BPMs affected by this particular failure mode is to reduce the SVD dominance limit to 0.3. In case a higher SVD dominance limit is used, IF eliminates the remaining faulty BPMs independently of SVD settings. Precise adjustment of the settings should be investigated during HL-LHC commissioning. The performance of IF in combination with the new Harpy should also be investigated as the BPM tunes used as one of the features in IF input are discretised in the FFT bins. Potentially, other signal properties obtained from harmonic analysis may be used in IF input.

5 Linear optics corrections in the insertion regions and β^* control

In this section, different aspects of the linear optics correction in the insertion regions will be presented, focused in particular on the high luminosity experimental insertions, where a good control of the beam size at the IP is required. To achieve the requested precision of the optics in the interaction point and to keep imbalance between the main experiments ATLAS and CMS below 5% [100] during squeeze process, the K-Modulation method is envisaged to be used to determine the β^*. In the first section, the expected accuracy of this method is discussed. Further sections deal with special considerations for the use of K-Modulation with a Van der Meer optics and as a tool to measure the crossing angle in the experimental insertions. A complementary technique to determine a possible betatron waist shift is presented in the following. With potential use of the HEL 2.6 and crab cavities, also a similarly good control over the optics in the matching sections will be required, with techniques being addressed in the later subsections. Lastly, a new method is described to determine the field errors in the triplet quadrupoles, possibly leading the way to an improved local linear optics correction.

5.1 Performance of K-Modulation in HL-LHC

Inferring β^* from K-Modulation measurements has so far been the most accurate way of determining the optics functions at the interaction points in the LHC [101] and SuperKEKB [102]. It is thus also considered as the primary method in the HL-LHC to assess β^* within the tight constraint of 2.5% accuracy. Further use

of this technique is expected in the matching section of HL-LHC insertion to determine the β-function at the crab cavities and provide better constraints for local corrections. Furthermore, such an approach is the main one for various beam instrumentation devices in IR4, as was already done in previous runs in the LHC.

By modulating the gradient of the first quadrupoles left and right of the IP, the average β-function in the quadrupoles is calculated using the tune change during the modulation, which is then used to obtain β^* via interpolation. Compared to optics measurements based on turn-by-turn data, this method also allows to determine any longitudinal offset of the minimum β-function from the IP. An illustration of a HL-LHC interaction region is presented in Fig. 19.

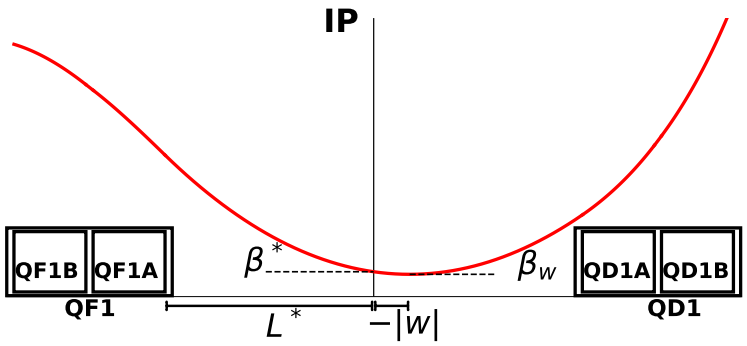

Figure 19: Schematic layout of a HL-LHC interaction region with split Q1 quadrupoles.

As the preferred measurement technique for determining β^*, precautions have already been taken in the IR design to ensure optimal conditions. Early simulations of K-Modulation in the HL-LHC [101] have shown that for a powering scheme where both magnets of the Q1 units are powered by means of the same power supply, thus preventing an individual gradient modulation, the required accuracy of 2.5 % on β^* cannot be achieved for $\beta^* \leq 22$ cm. In response to this observation, the installation of a 35 A trim power supply for Q1A is now foreseen, which reduces the uncertainty on β^* in simulations by about a factor 2. In Fig. 20, the error on β^* as a function of β^* is presented. For these simulations, the same longitudinal alignment tolerances and uncertainty on the quadrupole gradient as in [16] were used, together with updated values of the tune jitter due to power supplies [103], assuming an upgrade of the power converter in the arcs next to the high luminosity insertions to class 0.5 [104].

In the numerical simulations as well as in the optics commissioning phase, the fractional tunes are set to $Q_x = 0.28$, $Q_y = 0.31$ and a modulation amplitude of the quadrupole gradient was chosen such that the tune change does not exceed

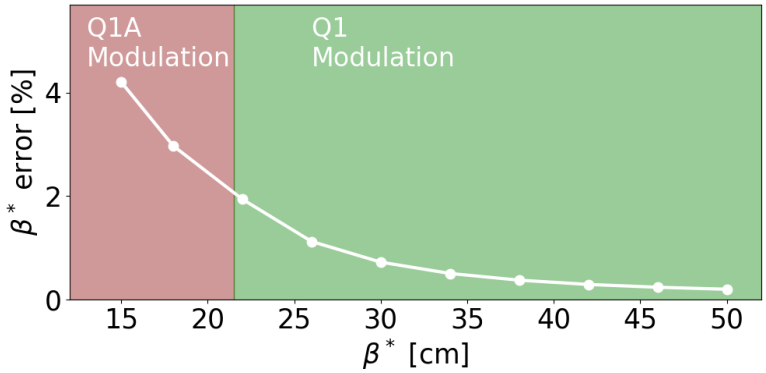

Figure 20: Expected β^* accuracy from K-Modulation versus β^*. Highlighted in red/aubergine, the range of β^* where modulation with a single quadruple has been used and provides more accurate results, taking into account the limited modulation amplitude due to the Q1A trim power supply constraints. The assumed tune uncertainty is $\delta Q = 2.9 \times 10^{-5}$.

$\Delta Q \approx 0.01$. The larger tune separation compared to nominal collision tunes ($Q_x = 0.31,\ Q_y = 0.32$) is chosen to allow for a larger tune change, which partly helps to mitigate the effect of the tune jitter δQ while avoiding distortion from linear coupling via the closest tune approach.

From Fig. 20 it is also apparent that for $\beta^* \leq$ 20 cm the requested accuracy of 2.5% is not yet achieved. In Fig. 21, the contribution of the individual error sources is presented for modulation of both Q1 parts or only Q1A. It shows that

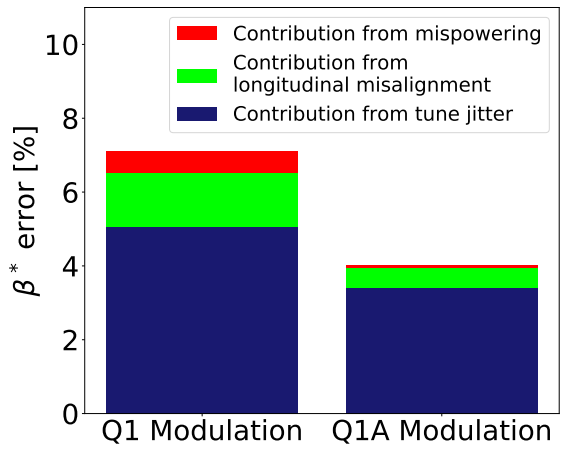

Figure 21: Contributions to the β^* accuracy when modulating Q1A and the two modules of Q1 at β^*=15 cm and $\delta Q = 2.9 \times 10^{-5}$.

even without any misalignment or mispowering errors contributions, the target accuracy is not achievable for the nominal case of $\beta^* = 15$ cm due to the dominant tune jitter of $\delta Q = 2.9 \times 10^{-5}$. In case no upgrade of the dipole power converters (PC) is performed, the tune jitter increases to $\delta Q = 4.1 \times 10^{-5}$ and, correspondingly, the accuracy at a $\beta^* = 15$ cm deteriorates from about 4 % to 7.5 %. On the other hand, assuming both the upgrade of the power converters and an additional reduction of a factor $\sqrt{2}$ in the short term stability of the power converters by running with the regulation loop closed on both DCCT+ADC channels [103], the tune jitter might decrease further to $\delta Q = 2.1 \times 10^{-5}$, thus reducing the error on $\beta^* = 15$ cm to about 2.3 %, meeting the target accuracy [105]. This configuration corresponds to the baseline as the dipole PC upgrade to class 0.5 was approved in the 136$^{\text{th}}$ HL-LHC TCC meeting [106].

However, measurements of the tune jitter during the LHC Run 2 have shown that taking only the contribution due to the power supply ripple into account underestimates the measured tune uncertainty by up to a factor 2. A comparison of expected and measured tune jitter for different optics is presented in Fig. 22. Thus, during the LHC Run 3 and the startup phase of HL-LHC, a particular focus will be put on determining the sources of tune jitter, and possible mitigation measures. For example, in Run 2 it was observed that upon application of corrections for normal octupole errors, both tune jitter and online linear-coupling measurements from the BBQ significantly improved [108]. An interleaved linear and nonlinear optics commissioning may be required in order to ensure good β^* accuracy given the potential impact of nonlinear corrections on the measured tune jitter. Further studies have linked the tune jitter to feed-down effects from sextupoles due to orbit jitter [109].

In Run 2, it was observed that the tune change due to K-Modulation is not sensitive to the local linear coupling present in the quadrupole. On the other hand, for the same level of local linear coupling, the beam size in the interaction point can be significantly affected. In order for the beam size to not deviate by more than 1% a correction of the linear-coupling RDTs f_{1001} and f_{1010} at the interaction point to $|f_{1001}|^2 + |f_{1010}|^2 \leq 0.005$ is required, under the assumption that $|f_{1001}| \approx |f_{1010}|$. The strategy for the correction of these RDTs is presented in Section 7.

Furthermore, it was observed in Run 3 that timing offsets between the gradient and BBQ data can lead to inaccurate K-modulation measurements. An new analysis of the BBQ data both improved the spectral resolution and the timing, yielding more accurate results [110].

5.1.1 Improvements on the K-Modulation analysis algorithm

In order to further constrain the measurement of β^* using K-Modulation, we introduced the phase advance of the IR measured using AC dipole excitation as a

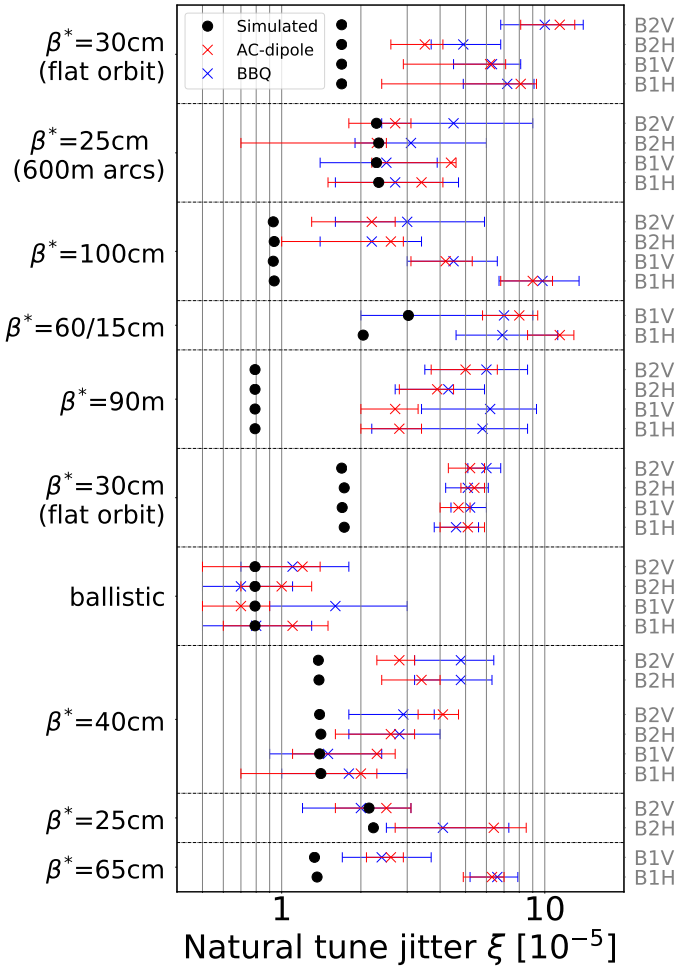

Figure 22: Comparison of expected and measured tune jitter in Run 2 with $1/\sqrt{2}$ improved noise level from power converters [107].

new constraint. The phase advance ϕ_{IP} along the drift that contains the IP can be evaluated as [44],

$$\phi_{\text{IP}} = \arctan\left(\frac{\hat{L}^* - w}{\beta_w}\right) + \arctan\left(\frac{\hat{L}^* + w}{\beta_w}\right) , \tag{5}$$

where $\hat{L}^*$ is the distance between the BPMs in both sides of the IP and β_w represents the value of the β-function at the position of the waist. From Eq. (5) we can calculate the phase advance using the reconstructed β_w and w. This value is compared to the phase-advance measurement obtained by using techniques such as the AC-dipole.

This new methodology has been tested with simulated data for different optics. The phase constraint is weighted and the weight can be adjusted manually in order

to give more preference to the phase or to the β-function value at the quadrupole location. The new figure of merit includes the new phase term $\frac{\Delta\phi_{\rm IR}}{\phi_{\rm IR}}$ not included previously and takes the form,

$$\chi^2 = (1-\Omega)\left[\left(\frac{\Delta\beta_{\rm foc}}{(\beta_{\rm foc}+\beta_{\rm def})/2}\right)^2 + \left(\frac{\Delta\beta_{\rm def}}{(\beta_{\rm foc}+\beta_{\rm def})/2}\right)^2\right] + \Omega\left(\frac{\Delta\phi_{\rm IR}}{\phi_{\rm IR}}\right)^2 , \quad (6)$$

where $\beta_{\rm foc}$ and $\beta_{\rm def}$ are the β-function at the focusing and defocusing quadrupoles and Ω is the weight between 0 and 1 assigned to the phase advance term $\Delta\phi_{\rm IR}$. The precise determination of the optimal weight Ω depends on the particular optics choice. Further studies are ongoing in order to generalise and automatise the choice of the weight.

5.2 van der Meer optics correction

During Van der Meer scans performed in the LHC [111], the transverse separation of the two beams is varied in both planes to calibrate the experimental luminosity monitors. One of the key ingredients for a correct calibration is a precise measurement of β^*.

K-Modulation presents some limitations on the accuracy of the reconstructed β^*. As derived in [112], the uncertainty in β^* is related to the uncertainty in β-function at the modulated quadrupole $\beta_{\rm mod}$ by the following relationship:

$$\frac{\sigma_{\beta^*}}{\beta^*} \approx \frac{\beta^* + \frac{(L^*+L_Q/2)^2}{\beta^*}}{\left|\beta^* - \frac{(L^*+L_Q/2)^2}{\beta^*}\right|}\frac{\sigma_{\beta_{\rm mod}}}{\beta_{\rm mod}} , \quad (7)$$

where L_Q is the length of the last quadrupole before the IP, which we need to take into account when thin lens approximation is used. One can see that for $\beta^* = L^* + L_Q/2$ a small error in the $\beta_{\rm mod}$ determination induces a large error in β^*. This is the case for the van der Meer optics and the addition of the phase advance in the IR as a constraint (as explained in the previous section) proved to be very useful to find a value of β^* with improved resolution. This new algorithm has been applied to reanalyse the measured data from the 2016 van der Meer MD [111]. After applying the changes described here, we obtained more reliable values for β^*, which are shown in [113].

5.3 Crossing angle from K-Modulation

On top of optics measurements, the orbit data collected during the K-Modulation measurements can be used to determine the position of the beams in the modulated quadrupoles. Measurements from the quadrupoles on either side of the IP

can be used to reconstruct the beam trajectory through the interaction region and calculate the crossing angle. Note that an accurate measurement of the crossing angle can be critical for controlling the luminosity in the experiments.

To make use of the vast amount of data collected at all BPMs, a new method has been developed that uses SVD to get an estimate of the beam position from the orbit data. In a first step, the method computes the expected orbit for a beam with a unit offset in the quadrupole and decomposes the result using SVD. The resulting vectors and singular values are then multiplied with the measured beam matrix in a way that returns the offset [112].

Using noise-free simulation data, this method has been used to reconstruct the crossing angle with a precision of $< 0.1\%$. When applied to measured data from modulating the quadrupoles in IR8, the error in the measured offset was initially above 10% using this method. This has been brought down to less than 5% by using the model data to disregard BPMs and time steps where the orbit response is expected to be small. Currently, it is unclear whether this precision can also be achieved for the more challenging optics in IR1 and IR5 due to lack of data, however, this method is to be further tested in future K-Modulation measurements.

5.4 Measuring betatron waist and dispersion via luminosity scans

In [44, 114] it was experimentally demonstrated that the measurement of the betatron waist position by means of luminosity scans features a significantly better uncertainty than K-Modulation, between a factor 2 to 3 at $\beta^* = 30$ cm. This measurement requires the careful preparation of knobs to change the betatron waist per plane and per beam without affecting any other optical parameter. The waist scan has to be performed returning to the initial setting frequently to remove possible drifts of luminosity due to, e.g. emittance blow-up. Figure 23 shows an illustration of the scaled luminosity versus waist knob setting from -9 cm to 9 cm, together with the parabolic fit. The measured vertical waist shift is -8.1 ± 1.1 cm. Contrary to K-Modulation, the measurement resolution of the waist position with luminosity should not deteriorate for lower β^* values. An uncertainty of 1 cm in the waist position would contribute to about 0.5% to the relative uncertainty of β^* for the HL-LHC design $\beta^* = 15$ cm.

A direct dispersion measurement at the IP can only be performed by measuring the beam displacement versus relative momentum deviation (dp/p). After beams have been set to collide the dp/p is changed only for one beam until some luminosity loss is measurable. The required transverse position shift Δx in the other beam to maximise luminosity gives IP dispersion by $D_{IP} = \Delta x/(dp/p)$. The precision of this technique is to be evaluated experimentally in Run 3.

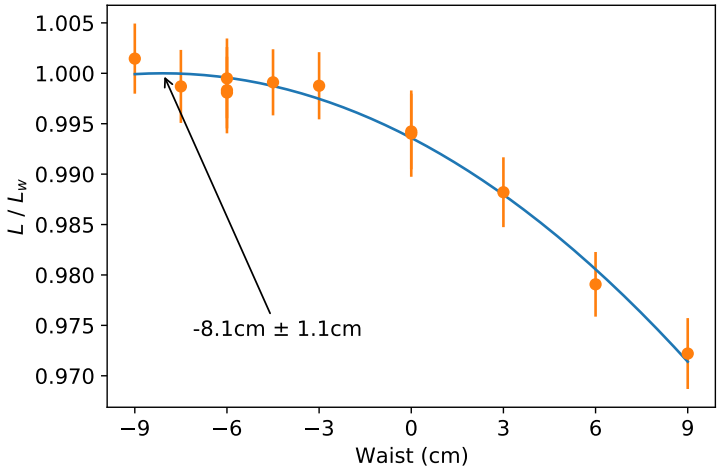

Figure 23: ATLAS luminosity versus the Beam 1 vertical betatron waist shift for β^*=30 cm [114].

5.5 Action-Phase jump technique for IR optics correction

Alternative approaches to the Segment-by-Segment (SbS) technique [115] for performing local optics corrections in the IRs are being explored. The so-called Action-Phase jump (APJ) technique [116, 117] has been tested in numerical simulations for the 2016 LHC optics to correct the local errors in IR1 and IR5 with $\beta^* = 40$ cm after introducing the errors in the inner triplet quadrupoles and matching section quadrupoles. Two scenarios are considered, differing in the errors associated with the matching section quadrupoles (Q4, Q5, Q6). In the first scenario, large magnetic errors in the matching section quadrupoles are considered. In Table 3 the distribution of absolute magnetic errors used in the simulations is shown. One can see that the errors assigned to the matching quadrupoles are particularly high. These values significantly differ from those used so far in LHC operation [71]. However, these values do not represent the actual magnetic error of the corresponding magnet, but rather they can be seen as effective errors. A better understanding of the nature of these effective errors in the matching section quadrupoles is ongoing. In the second scenario from table 3 smaller errors are considered.

In Fig. 24 the residual horizontal β-beating is shown for Beam 1 after applying both methods, and in Table 4 the RMS and the maximum β-beating before and after correction using APJ and SbS are shown for both scenarios considered. In particular, for the case with large magnetic errors in the matching section quadrupoles (scenario 1), using APJ, the residual RMS is always below 2% while SbS technique presents higher values in all planes. When smaller magnetic errors in the

Table 3: Magnetic errors assigned to the inner triplet and matching section quadrupoles.

$[10^{-5}\mathrm{m}^{-2}]$	Scenario 1 & 2	
Magnet	L	R
Q1	-0.6	0.70
Q2	-1.17	0.74
Q3	-1.31	2.60

	Scenario 1		Scenario 2	
Magnet	L	R	L	R
Q4 B1	-7.00	5.70	0.34	-0.55
Q4 B2	7.00	-5.70	0.23	0.19
Q5 B1	-6.86	2.98	0.25	-0.08
Q5 B2	7.01	-3.45	0.03	0.22
Q6 B1	41.34	-23.71	0.05	-0.009
Q6 B2	-31.51	20.44	-0.12	0.03

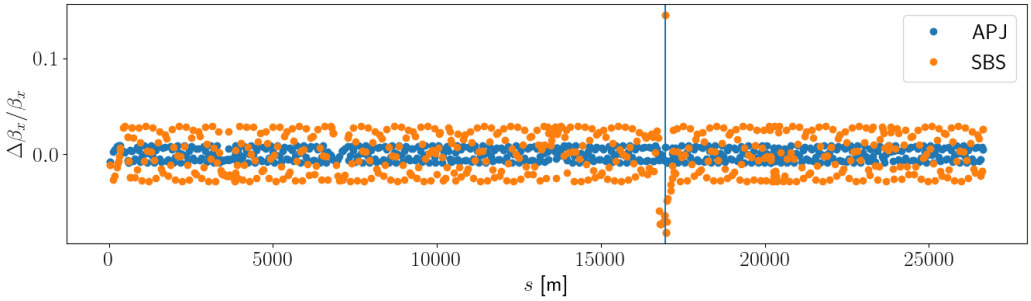

Figure 24: Computed β-beating along the LHC ring for Beam 1 in the horizontal plane, after adding the errors of scenario 1 in Table 3.

matching section are considered (scenario 2), both techniques perform similarly.

The APJ technique has been successfully used in the 2022 LHC optics commissioning to compute the local optics corrections in IR1 [118]

5.6 BPM calibration via optics measurements

β-functions can be measured using phase information (β^{ϕ}) [119, 120] or amplitude information (β^{A}). The biggest limitation of the latter is the poor knowledge of BPM calibration errors. In [121] the rms calibration errors of the arc BPMs are estimated via the ratio $\sqrt{\beta^{A}/\beta^{\phi}}$ to be about 1.5%. Figure 25 shows histograms of these calibrations for two different optics. On the other hand, the BPMs in the IRs

Table 4: Computed RMS and maximum β-beating along the ring before and after applying APJ and SbS correction techniques in Beam 1 and Beam 2. for both scenarios of magnetic errors.

	Scenario 1				Scenario 2			
	B1		B2		B1		B2	
$\Delta\beta/\beta$ [%]	H	V	H	V	H	V	H	V
Uncorrected RMS	8.14	12.8	11.8	6.16	6.10	12.5	13.9	6.22
APJ RMS	0.63	0.55	0.73	1.57	0.22	0.17	0.17	0.20
SbS RMS	2.56	0.85	1.19	3.57	0.07	0.87	1.48	0.40
Uncorrected Max	117	98.6	53.6	79.19	102	73.5	71.7	82.1
APJ Max	0.92	1.08	1.06	2.21	0.33	0.26	0.25	0.29
SbS Max	14.5	6.31	4.62	7.08	0.41	1.24	2.18	0.59

were identified to have significantly larger BPM calibration with an average shift of about -4% with respect to arc BPM calibration (see below for recent insights in the arc BPM calibration errors). These were measured with very good accuracy thanks to the use of the ballistic optics that features no quadrupolar fields in the IR and therefore negligible systematic errors in β^{ϕ}. Figure 26 shows an illustration of the difference in the reconstructed β^{A} and β^{ϕ} before and after calibration from [121].

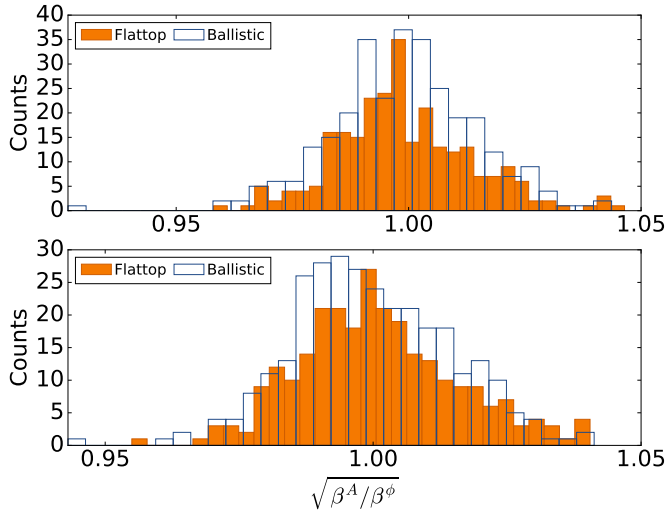

Figure 25: Histograms of the ratio $\sqrt{\beta^{A}/\beta^{\phi}}$ horizontal (top) and vertical (bottom) plane for the standard BPMs and different optical configurations in 2017, with a rms spread of about 1.5%.

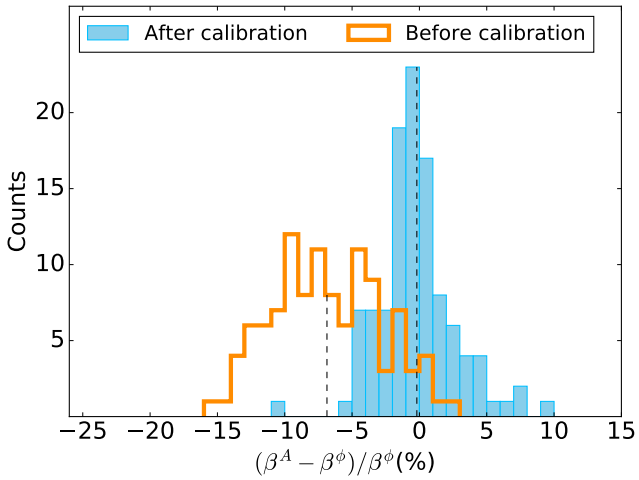

Figure 26: Histogram of β-beating before and after calibration, using β^ϕ as reference in horizontal and vertical planes measured for several optics: Injection and Flattop during 2017 and 2018 (Beam 1, horizontal and vertical planes, IR1 and IR5).

The momentum compaction factor has been aimed to be measured in [122] by fitting the RF-frequency shift over the relative momentum offset, where the latter is obtained using the orbit data recorded from arc BPMs. In analysed samples for various optics a systematic 3% lower momentum compaction factor has been found, which cannot be explained by strong systematic quadrupole errors. This offset is therefore attributed tentatively to an average arc BPM calibration error. A novel LHC optics with a lower arc cell phase advance, namely 60° compared to the nominal 90°, has been designed [123], where one important feature is the factor 2 larger momentum compaction factor. This configuration has successfully been measured in Run 3 for beam 1 yielding consistent results with the assumption of a systematic arc BPM calibration error of 3% [124]. Additionally, further analysis will enable interesting complementary studies, which will lead to new insights on the magnetic imperfections, misalignments, and optics correction techniques.

A new ballistic optics has been designed with Q5 quadrupoles switched off in IR4 that will allow accurate measurement of the IR4 BPM calibration factors. The magnets strength and beam size in this optics is designed in such a way that a test with the beam can be performed at injection as well as collision energies without changing the optics. The slight change in phase advance can be compensated in the arcs. A plot of the optics for Beam 1 is shown in Fig. 27 (the optics for Beam 2 is similar).

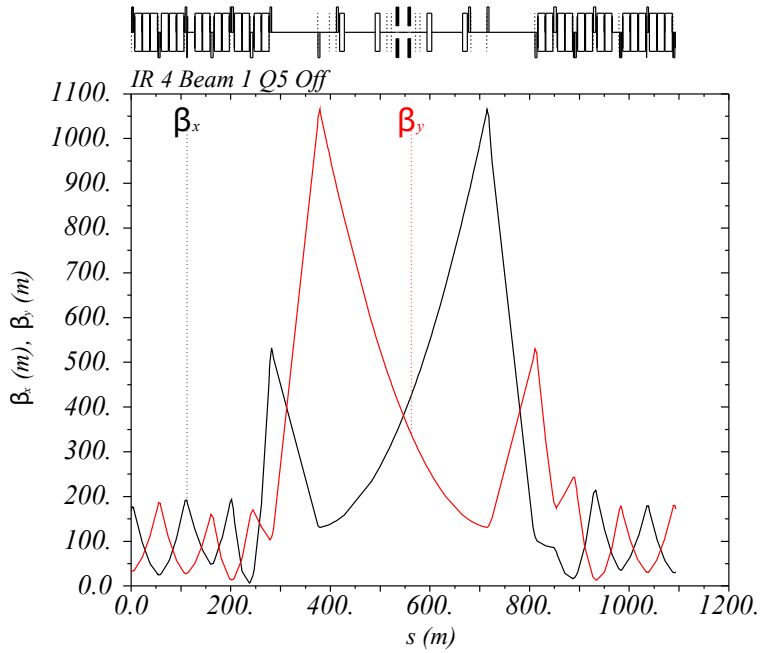

Figure 27: Ballistic Optics for BPM calibration in IR4.

5.7 Estimation of triplet errors using Machine Learning

Machine Learning (ML) techniques for optics corrections are currently being investigated. Supervised regression models [125, 126] offer a possibility to predict the gradient errors of single quadrupoles from the optics perturbations introduced by these errors. The prediction of triplet errors obtained from such a model potentially can provide a better control of β^*. To train ML models for quadrupole errors prediction, we generate thousands of MAD-X simulations where the ideal optics is perturbed by randomly-generated quadrupole errors. These errors are then used as target variables to be predicted by ML model. The input features are the deviations between ideal and perturbed values of the phase advance, normalised dispersion at all BPMs and β at the BPMs next to the IPs. The features are given realistic noise corresponding to the measurements. This allows to predict quadrupole errors for Beam 1 and Beam 2 simultaneously, considering the triplets are affecting both beams.

Currently, the models have been trained on simulations of the LHC optics used during the 2016 and 2018 runs, with $\beta^* = 40$ cm and $\beta^* = 60$ cm. The details on the data set generation and model training can be found in [127, 128, 129]. The results of individual triplet prediction obtained from a regression model using 100 000 samples (80% used as training and 20% as test set) are presented in Fig. 28. Due to the powering, the corrections are performed based on circuits rather than

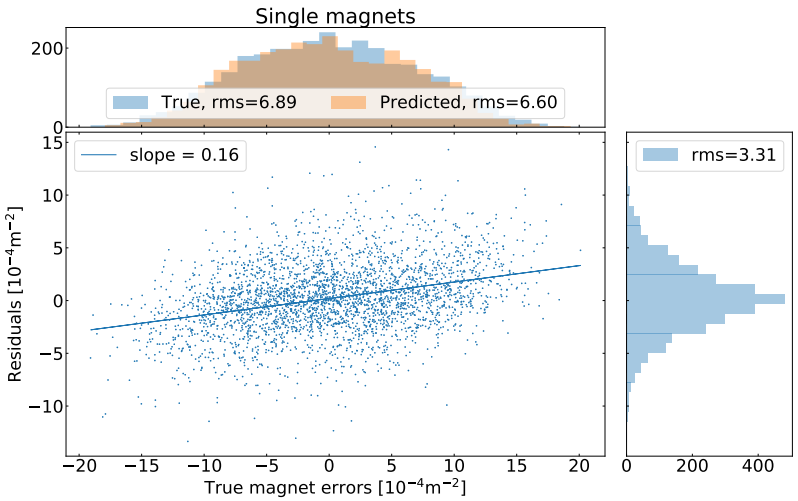

Figure 28: Prediction of individual triplet errors performed on 100 validation simulations illustrating the prediction accuracy. The slope is the correlation between true values and residuals, indicating the generalisation error of supervised regression model.

on single magnets. Combining the predictions for single triplet quadrupole magnets into the correction circuits, we observe a reduction of generalisation error from 16% to 5% and 1% for the combination of Q1 and Q3, and Q2A and Q2B quadrupoles, respectively.

6 Global linear optics corrections

Global optics corrections are based on the use of precomputed response matrices upon a change of available quadrupoles on phase advance, β^* values, dispersion, and linear-coupling measurements [130]. Phase and β beating measurements from BPMs carry similar information [131], therefore it is not needed to include both in the global corrections. Yet, β^* measurements from K-modulation are useful in global corrections. HL-LHC optics foresees to increase the β-functions in the arcs following the Achromatic Telescopic Squeeze [23]. Dedicated experiments with these optics in 2018 revealed the need for corrections in the arcs [44]. Since there are no independently powered quadrupoles in the arcs orbit bumps at sextupoles were used as illustrated in Fig. 29. The actual error sources in the arcs could not be identified. The finding of a new observable that depends only on the local optics errors in a given segment [133] might shed light on the nature of these arc errors in the future.

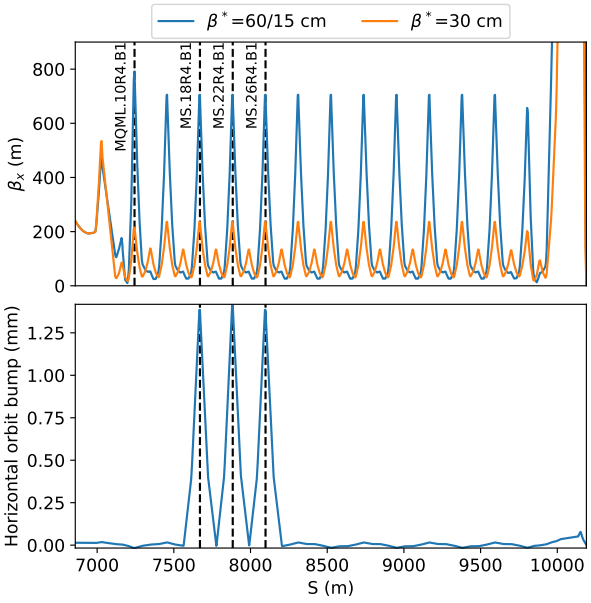

Figure 29: The top plot shows the design horizontal β-function from IP4 to IP5 for $\beta^* = 60/15$ cm flat optics and for $\beta^* = 30$ cm (the nominal 2018 optics). The ATS optics scheme in the flat optics increases the β-function in this arc by a factor of 4. The bottom plot shows the horizontal orbit bump implemented in the sextupoles to correct the measured optics errors via feed-down.

6.1 Estimation of global errors using Supervised Learning

Besides the control of β^* by reconstructing local errors in the triplets, global corrections can also benefit from applying supervised ML models. As described in 5.7, it is possible to predict all quadrupole gradient errors around the machine. In preliminary studies, the predicted individual quadrupole errors have been used to reconstruct β-beating and normalised dispersion perturbation. For the LHC simulations using 2018 optics, $\beta^* = 40$ cm we achieved rms error of β-beating reconstruction below 1%, the rms of normalised dispersion reconstruction is below 0.001 m. We have also examined this approach on the LHC measurements from 2016 in a virgin machine [134] – the rms of β-beating reconstruction in Beam 1 are 2% and 7% in horizontal and vertical planes, respectively, and 9% in the horizontal and 3% in the vertical plane of Beam 2. The achieved results on reconstructing the optics perturbation using the predicted quadrupole errors demonstrate the ability of supervised regression models to provide reliable knowledge about the error sources in the machine and potentially perform global and local optics corrections at one step for both beams simultaneously.

7 Local and global linear coupling control

The effect of global linear-coupling can be corrected by a pre-defined global correction knob [135]. Similar to a local β-function change with the application of a global tune trim, there might still be a residual effect on the local linear-coupling from the global correction. As this effect is small, the local and global linear-coupling can be treated individually and the local linear-coupling error can be corrected by a dedicated correction scheme, which is usually applied near the IRs, where the local linear coupling is most relevant.

7.1 Global linear coupling

As described in the introduction of this report, the strictest requirement for the control of the transverse linear coupling is coming from the loss of Landau damping due to a too large linear-coupling value. Additionally, the control of the global linear coupling is also of importance for the tune feedback, and special runs where the horizontal and vertical emittances are significantly different. The requirement $\Delta Q_{\min} \leq 10^{-3}$ for $Q_y - Q_x \approx 5 \times 10^{-3}$ is set for a single particle without any long-range beam-beam effect included.

The strategy to control the global linear coupling during the end of Run 2 was based on the dedicated correction tool [136, 137, 138]. This tool excites, with the help of the ADT, a forced motion of a single bunch in a similar way to the AC-dipole excitation. When used in this manner, the ADT is therefore often

referred to as ADT-AC-dipole. The turn-by-turn data is captured by all BPMs, automatically analysed, and a correction value is proposed to the operator. This tool was used successfully in Run 3 for coupling corrections, as well as linear optics measurements [139]. It is foreseen to play a prominent role for optics measurements in the HL-LHC.

7.1.1 INJECTION

The transverse linear coupling has been observed to change at injection. This has been linked to the powering of the correcting sextupoles attached to every dipole (MCS) [140]. In Run 3, a new correction scheme where the dynamic compensation of the b_3 is not evenly distributed between the arcs, is foreseen to be used. This way, the chromaticity, as well as the global linear coupling, can be kept constant. The expectation is that this will remove the observed linear-coupling decay at injection. However, there is still a fill-to-fill variation that is predicted to persist. This will be evaluated in Run 3 but it is likely that a procedure similar as in Run 2, where a pilot bunch was injected and used to measure and correct the chromaticity and the transverse linear coupling, will be needed. While the current injection tunes are mainly chosen based on e-cloud consideration, the tune split was also chosen with consideration of the transverse coupling. A potential benefit of preventing the linear-coupling decay is the possibility to lower the vertical tune, which could help mitigate effects related to the third order resonance in the vertical plane.

7.1.2 TOP ENERGY

The short-term stability of the coupling value, i.e. the stability during a single fill, has been measured in the LHC and has shown a typical value of $\pm 2 \times 10^{-4}$, without any meaningful difference between the two beams. Measurements in two consecutive fills indicate that its variation is in the range of $\pm 3 \times 10^{-4}$ [141]. However, over long time scales the linear coupling has been observed to drift. Due to the lack of measurements for all fills, or a sizeable number of them, it is not possible to establish whether the change has been a step-like variation between two fills or a gradual drift. If these changes in transverse linear coupling are driven by variations in the tilts of the triplet, then the expected range of the effect will scale linearly with $\sqrt{\beta_x \beta_y}$ in the triplets. In Run 2, drifts of $2 - 3 \times 10^{-3}$ were observed over time periods of a few months for a β^* of 30 cm. Unfortunately, we do not have many measurements with the same bunch configuration and β^* and it is therefore not possible to correlate the coupling measurements with the measurements of the triplets tilts. It is therefore desirable to measure the transverse linear coupling regularly in operation using the same bunches, without long-range

beam-beam interaction. This has been proposed for Run 3 [142]. These measurements would provide a better understanding of how the linear coupling varies over a year.

Note that the change of crossing angles has an impact on the transverse linear coupling due to feed-down from higher-order field errors [45]. The recommendation would be to measure this effect in commissioning and implement a correction that follows the change in crossing angle during each fill.

7.1.3 LINEAR COUPLING FROM LONG-RANGE BEAM-BEAM ENCOUNTERS

In 2017, the linear coupling was measured for several consecutive fills using the ADT-AC-dipole and the results showed a variation within 10^{-3}. However, when the filling scheme was changed, the measured linear coupling changed by about 2×10^{-3}. This triggered an MD where the effect of the long-range beam-beam (LRBB) encounters on transverse linear coupling was measured [143] for different transverse separations. The measured effect was very similar to the one previously observed in operation. Three bunches with different LRBB interactions were measured as shown in Table 5.

Table 5: The different bunches used in the experiment and whether they experienced long-range beam-beam effects in certain IPs, according to their collision scheme.

Bunch ID	IPs 1 and 5	IPs 2 and 8
301	No	No
901	Yes	Yes
2283	Yes	No

Bunch 901 and 2283 had almost identical values of C^- while 301 differed by $\approx 2 \times 10^{-3}$ when β^* was 40 cm and below. This indicates that the effect was mainly deriving from the LRBB in IP1 and IP5. In a perfect machine, it is not expected to see any effect of the LRBB on the transverse linear coupling. The observed effect could, however, be explained by a 5-10 deg rotation of the crossing angles [144]. In Run 3 there is a proposed MD to study this effect in more detail. This includes understanding the additional effects coming from the beam-beam interaction and how this impacts the measurement.

In the HL-LHC filling scheme, the so-called "non-colliding" bunches actually collide in IP8 and experience long-range interactions at other locations. The baseline correction strategy is therefore to have a special filling scheme where there are no beam-beam interactions for a limited number of bunches and use these to measure the linear coupling. Such a scheme would result in about 9%

less bunches, but would only be needed every second week if triplets tilt by about 40 µrad over one year (as seen in 2016), resulting in a small reduction in the integrated luminosity [145]. The strategy we are aiming to develop during Run 3 is to measure the linear coupling also for the bunches with long-range beam-beam, but this needs to be carefully validated before it can become the baseline correction strategy. However, if successful, no special filling scheme would be needed for the HL-LHC.

The linear coupling generated by long-range interactions in one IP in the presence of a roll angle error is well approximated by [146, 144]:

$$|C^-| \approx \frac{2 r_p N_{LR} N_b}{\pi \theta^2 \beta^* \gamma} \sin(\phi_r) \cos(\phi_r), \tag{8}$$

with r_p the classical proton radius. In the HL-LHC, the number of long-range interactions between the D1's in each IR N_{LR} is 36 and the bunch population N_b is $2.3 \cdot 10^{11}$. With a β^* of 1 m, a full crossing angle θ of 500 μrad and a roll angle of the crossing angle plane ϕ_r of 1.4°, one obtains $|C^-| \approx 1 \cdot 10^{-4}$. Such a roll angle corresponds to a crossing angle perpendicular to the design crossing plane of 6 μrad. The contribution of IRs 2 and 8 is approximately $3 \cdot 10^{-5}$ each, totalling $|C^-| \approx 1.6 \cdot 10^{-4}$ in the worst configuration of phase advances between the sources. The correction of these contributions can be performed globally. Nevertheless, due to the PACMAN effect this correction will not be accurate for bunches experiencing different sets of beam-beam interactions [143]. The maximum difference between the bunches experiencing the highest and the lowest number of long-range interactions is about half (neglecting the non-colliding bunches). Thus, the remaining PACMAN linear coupling after correction for a specific set of bunches is half of the total. It is worth noting that, because of the interplay of long-range interactions with the arc octupoles, the most critical bunches in terms of Landau damping are the nominal bunches (i.e. those experiencing all beam-beam interactions) when operating the Landau octupoles with negative polarity. When operating with positive polarity, the most critical bunches are the most PACMAN (i.e. the ones missing the highest number of beam-beam interactions). The coupling correction should therefore target the most critical bunches to maximise the linear coupling that can be tolerated by the other bunches.

If the required accuracy on the angle of the crossing angle plane cannot be obtained with K-Modulation, an iterative minimisation could be envisaged by rotating the crossing angle in steps and measuring the bunch-by-bunch coupling with the ADT-AC-dipole.

7.2 Local linear coupling correction

A good correction of the local linear coupling is essential to ensure the correct beam size at the IP and, as a consequence, the luminosity for the experiments. The approach used in previous LHC runs has been to measure the RDTs near the IP and use the two skew quadrupole correctors left and right of the IP to compensate for the contribution of the IR to global coupling, with the segment-by-segment technique. This has, however, proven to be challenging given that the small number of BPMs makes phase reconstruction difficult, and the phase advance in this region is itself not suitable for the reconstruction of the linear-coupling RDTs.

In 2018, during the ion run, a fitting tool was used to find automatically a correction setting of the skew quadrupoles [44]. Unfortunately, there was a human mistake when the corrections were sent and as a consequence the settings of the left and right MQSX were swapped, causing a reduction of the luminosity by approximately 50 %. This was corrected through scanning the colinearity knob, which is designed to balance the strength of the left and right MQSX, while observing the luminosity. The definition of the colinearity knob is described in Table 6.

Table 6: Definition of one unit of the colinearity knob.

Magnet	K_{1S} [m^{-2}]
MQXS.3L2/K1S	$+10^{-4}$
MQXS.3R2/K1S	-10^{-4}

A comparison of the strength found after the luminosity scan and what was found with the automatic correction from the RDTs would, in the simulation, translate into a 5% luminosity loss. In the case of HL-LHC, the luminosity loss would have been greater due to the larger β-functions in the triplet and this is shown in Fig. 30.

A luminosity scan could be needed to find the optimal setting of the skew quadrupoles, however this requires nominal bunches, which in turn requires a collimation setup. It is therefore desirable to have an additional method to find the optimal local linear-coupling correction to then be potentially validated or finely adjusted with a luminosity scan. An idea for such a method was tested in the last MD block in 2018 [148], which consists in changing the strength of the left and right side triplets in order to break the symmetry of the IR optics. The imbalance in the correction of the left- and right-hand side MQSX (MQXS.3L(IP), MQXS.3L(IP)) does then have an impact on the global transverse linear coupling, since it is no longer possible to create a closed linear-coupling bump around the IP.

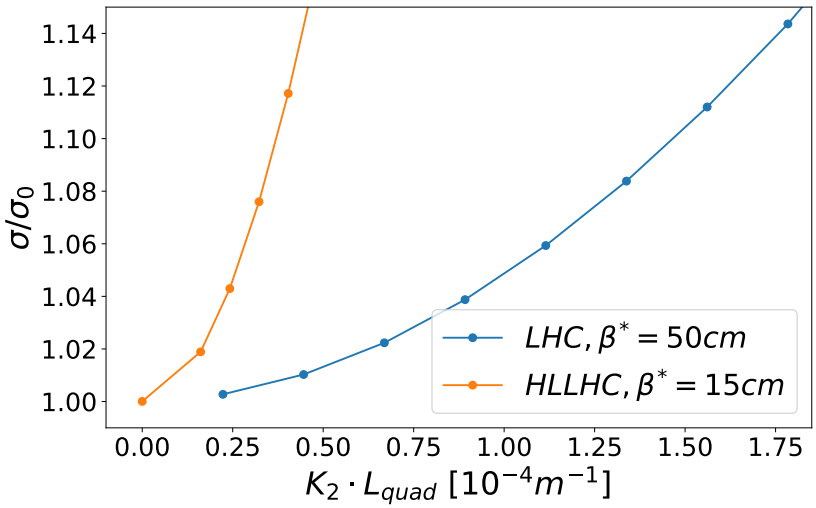

Figure 30: Relative increase in IP beam size from powering the right and left IR skew quadrupoles with opposite sign for LHC and HL-LHC [147].

The MD was successful but gave a difference of 3 units in the colinearity knob compared to results from the luminosity scans. This translates into a luminosity loss of about 3 % if the correction found from the the MD would have been used without a fine tuning of the luminosity. It should, however, be stressed that only one beam was available for the test and it is not currently possible to conclude if the optimal settings were different for the two beams, while the optimal found with luminosity was a compromise between the two.

In Run 3, this was refined and a new method was developed to determine local linear coupling corrections, that relies on the application of this Rigid Waist Shift [132].

The foreseen method for correcting the local linear-coupling in the HL-LHC would envisage three steps. First, determine a compensation of the IR's contribution to global coupling based on the RDTs from the turn-by-turn measurements, using the segment-by-segment technique. This first step is crucial to allow for the squeezing of the beams to low β^* and safe beam operations. Then, use the aforementioned Rigid Waist Shift method based on breaking the optics symmetry between the right- and left-hand side of the triplet skew quadrupole correctors. Finally, scan the colinearity knob in order to validate the correction and possibly optimise the luminosity.

7.3 Studies in preparation of the HL-LHC

A number of studies have been described in the previous sections to control the transverse linear coupling to the required level. Here we summarise the studies planned in Run 3 in order to be ready for the HL-LHC:

- Optimise the parameter of the ADT-AC-dipole and the new tune measurement system.
- Determine the accuracy and resolution of the measurement of the ADT-AC-dipole.
- Use the uneven MCS powering to compensate for the drift of the linear coupling at injection.
- Develop the method based on changing the triplet powering to calculate local linear-coupling corrections.
- Improve the luminosity scans for fine-tuning the local linear-coupling corrections.
- Improve the understanding of the LRBB impact on transverse linear coupling.

8 Sextupole and octupole corrections

Low-β^* operation implies large β-functions in the IR magnets, notably the triplets and separation dipoles. Nonlinear errors in these elements can therefore introduce large perturbations of the beam dynamics, posing significant challenges for successful operation as discussed in [151]. Since 2017, beam-based correction of sextupole and octupole errors (normal and skew) in the low-β IRs has been included in the LHC optics commissioning strategy. A detailed review of the LHC optics commissioning strategy implemented after 2017 is discussed in detail in [45]. This existing strategy also provides a baseline option for beam-based correction of sextupole and octupole errors in HL-LHC IRs. LHC commissioning strategy used multiple nonlinear observables, the minimisation of which facilitated the determination of beam-based corrections. Of particular note, the global strength of the normal octupole correction was constrained via the measurement of amplitude detuning with the AC-dipole [152]. Figure 31 shows an example of the amplitude detuning measured before and after application of normal octupole corrections in IR1 and IR5.

Detuning measurements for normal octupole correction were complemented by measurements of the quadratic feed-down to tune, which provides a local observable for b_4 errors in IR1 and IR5. Figure 32 shows the reduction to quadratic

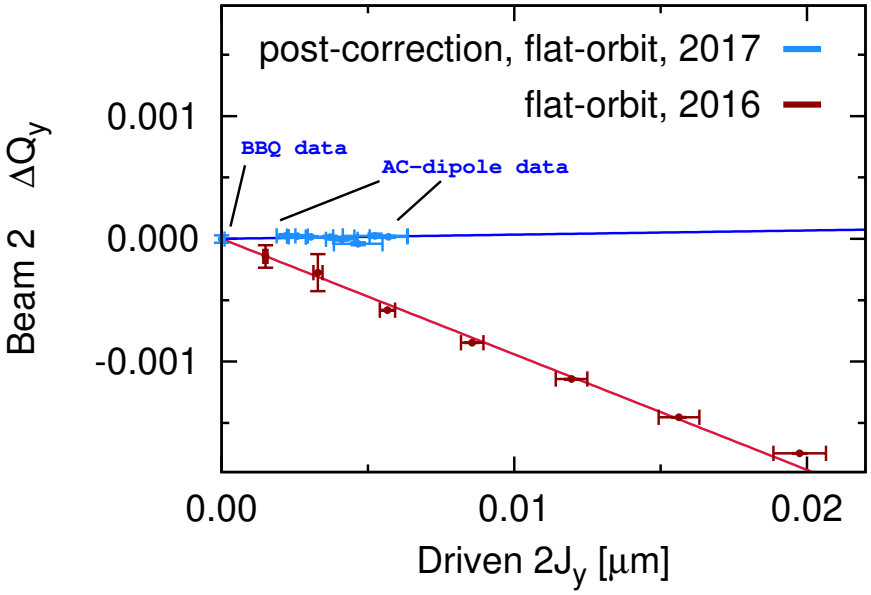

Figure 31: Example of amplitude detuning measured before and after application of normal octupole corrections in LHC IR1 and IR5.

variation of tune with crossing-angle obtained upon application of normal octupole corrections in the LHC.

Sextupole corrections were determined by minimising the linear variation of tune and linear coupling with crossing-angle. Figure 33 shows an example of the reduced linear variation of tune with crossing angle upon application of sextupole corrections.

RDTs measured with an AC-dipole differ from the free RDTs [153, 154, 155, 156, 157] and are referred to as driven RDTs. These were used to validate the sextupole and octupole corrections determined by these methods. Figure 34 shows histograms of the driven f'_{4000} RDT before and after normal octupole correction was implemented in IR1, and then also in IR5. RDT measurements were also used for the first time in 2018 to directly calculate corrections for the skew octupole errors in LHC IR1 and IR5. A detailed discussion of the application of beam-based RDT measurements to the correction of nonlinear errors in the LHC insertions is found in [156, 157].

The methods employed for the determination of beam-based correction of nonlinear errors in the low-β LHC IRs can also be applied for sextupole and octupole correction in the HL-LHC. The successful LHC commissioning required nonlinear optics measurement and corrections to be interleaved with the linear optics commissioning since the nonlinear errors can both influence the quality of

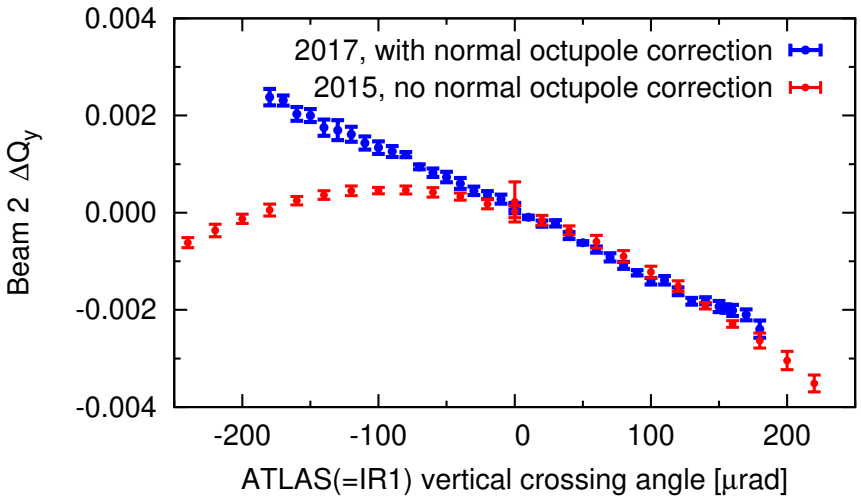

Figure 32: Quadratic variation of tune with crossing-angle measured before and after application of normal octupole correction in LHC IR1

linear optics measurements (for example via reduction in BBQ tune measurement quality), and can directly introduce additional linear optics perturbations via feed-down once the crossing-scheme is applied. This necessity of an iterative, combined approach to linear and nonlinear optics commissioning has been discussed in [45, 151].

So far, discussion has focused on the beam-based measurement and correction techniques employed at the LHC. However, the design strategy for both LHC and HL-LHC assumes the correction by minimisation of selected RDTs, based upon magnetic measurements performed during construction. This approach was not used in the LHC, as several discrepancies were observed between the corrections required to minimise beam-based observables (as described above) and the predicted corrections based upon magnetic measurements. In the sextupole domain, large relative discrepancies were observed, with the beam-based correction in some cases even showing an opposite sign to that inferred from the magnetic model [45]. The connector sides of the IT quadrupoles also generate b3/a3 but this is not included in the models. In absolute terms, however, the LHC sextupole corrections are small and were also clearly observed to be subject to additional feed-down generated by the octupole correctors due to orbit errors or misalignments of the nonlinear correctors [45]. As such, the observation of sextupole discrepancies with the model primarily serve to motivate the inclusion of feed-down due to alignment errors into any model-based commissioning strategy for the HL-LHC. A discrepancy was also observed between the beam- and model-based normal octupole correction. This can be seen, for example in Fig. 35, by comparing the

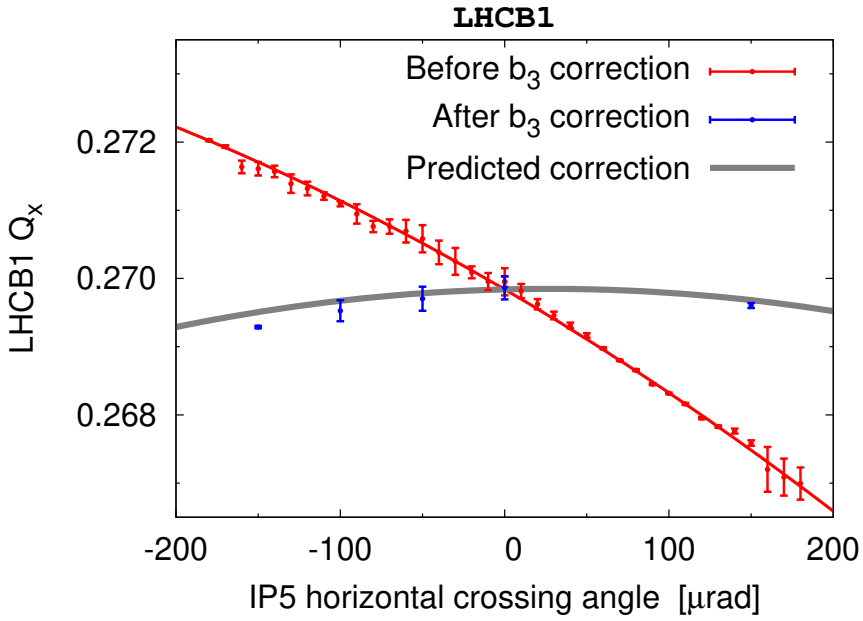

Figure 33: Reduction of linear variation of tune with crossing angle upon correction of normal sextupole errors in LHC IR5.

expected and measured amplitude detuning in the LHC (at flat-orbit, $\beta^* = 0.4\,\mathrm{m}$).

The reason for the normal octupole discrepancy with the magnetic model is not yet understood [159, 160, 161, 162]. Figure 36 compares the required normal octupole LHC corrector strength in IR1 and IR5 inferred from beam-based measurements, to that predicted by the magnetic model. The final prediction of the magnetic ('WISE' [51]) model is shown in green, while the top, middle, and bottom plots show how this final prediction is built up from several contributions. The top plot shows the contribution to the correction from a large systematic b_4 error in the MQXA. The middle plot shows the effect of including comparatively very small b_4 errors in the MQXB triplets (due to the larger β-function in these magnets they still generate a significant perturbation). Finally, the bottom plot shows the consequence of including the distortion of the main quadrupole field by the beam-screen. Values for the b_4 components in the Q1 and Q2 magnets (including the beam-screen contribution) are given in Tab. 7. Operational corrections based upon observations with beam are indicated in all plots. Model-based values were used to define corrections in IR1 (given a good agreement observed between measured and modelled feed-down to tune in this IR), with IR5 corrections then being defined to minimise the remaining amplitude detuning (unlike IR1 a large discrepancy was observed between the modelled and measured feed-down in IR5).

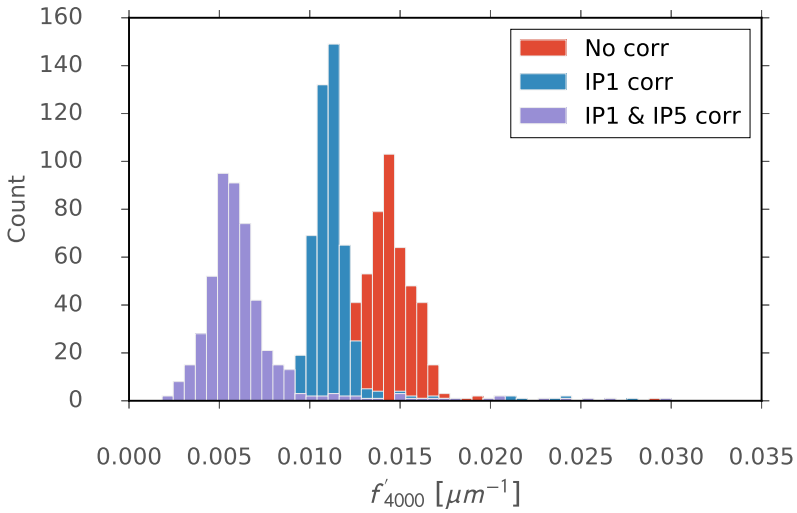

Figure 34: Reduction of the f'_{4000} normal octupole RDT, observed in the LHC upon application of normal-octupole corrections determined from measurements of amplitude detuning and quadratic feed-down to tune.

Further details can be found in [45].

Figure 36 illustrates that at the desired level of precision for IR nonlinear corrections which will be employed in the LHC and HL-LHC, even the fine detail of the magnetic model can be very relevant. We note, for example, that even small b_4 errors in the MQXB and the contribution of the beam-screen introduce non-negligible changes to the correction when compared to the spread in the values predicted by the complete model. That said, the observed octupole correction discrepancy in the LHC is also a reflection of the high-level of precision demanded of the magnetic model and the beam-based measurements. Figure 37 shows a comparison of the predicted octupole corrections in IR1 and IR5 compared to the operational values, plotted over the full range of available corrector strength.

Clearly, the influence of even small random errors on the triplet multipoles and of the beam-screen will have to be considered in the context of any future model-based correction strategy. The cause of the discrepancy between the beam- and model-based correction is not yet understood, however, several sources are under consideration. The most relevant missing source in the model seems to be the longitudinal distribution of the b_4 harmonic inside each quadrupole, which is analysed in detail in the following section. Fringe fields of the CMS solenoid are not generally included in LHC models. Studies with SAD [163], showed no impact on detuning for a basic model of the experimental solenoid fringe fields, however non-conformity of the fringes and observations from magnetic measurements re-

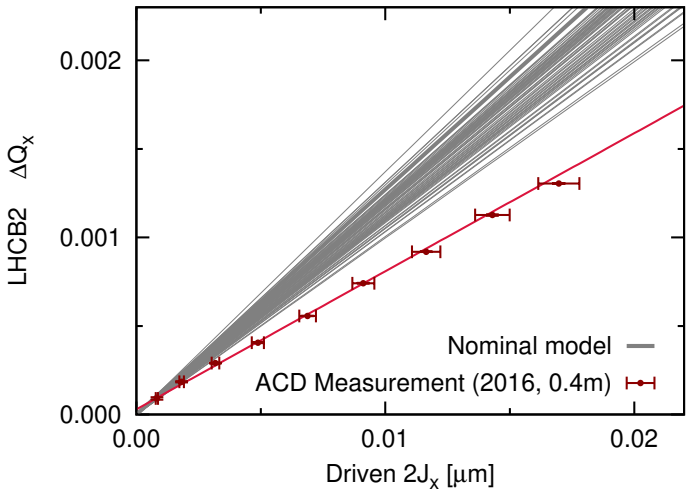

Figure 35: Amplitude detuning measured in the LHC (red) compared to that predicted by the magnetic model (gray) without inclusion of any misalignment error.

main to be considered. While the influence of the beam screen is included, it is also of interest whether additional effects, for example welds in the beam-screen, can significantly modify this component of the predicted correction. Longitudinal alignment errors are not currently included when determining model-based corrections.

While undoubtedly complicated, beam-based correction of the IR sextupole and octupole errors in the LHC yielded clear operational benefits. The operational impact of the nonlinear errors in the HL-LHC will be very dependent on the β^*, and the obtained field quality. Beam-based studies in the LHC have clearly implied that sextupole perturbations representative of those expected at end-of-squeeze in the HL-LHC can be detrimental to the commissioning effort [151]. As discussed in Section 2.8, on the upper end of the predicted b_4 error distribution the triplet octupole errors in the HL-LHC at $\beta^* = 0.4\,\mathrm{m}$ can also generate a comparable amplitude detuning as that observed in the LHC at $\beta^* = 0.4\,\mathrm{m}$ to have an impact on operation, and in particular to significantly reduce the performance of the BBQ. Noting that the perturbation scales with $(\beta^*)^{-2}$, this detuning can increase by about a factor 7 by end-of-squeeze ($\beta^* = 0.15\,\mathrm{m}$). Non-correction of the octupole errors has the potential to significantly impede commissioning efforts at lower-β^* and impact upon operation. Consequently, it is essential for HL-LHC commissioning strategy that beam-based methodology and tools are in place at moderate $\beta^* \approx 0.4\,\mathrm{m}$ to facilitate sextupole and octupole correction in the triplets.

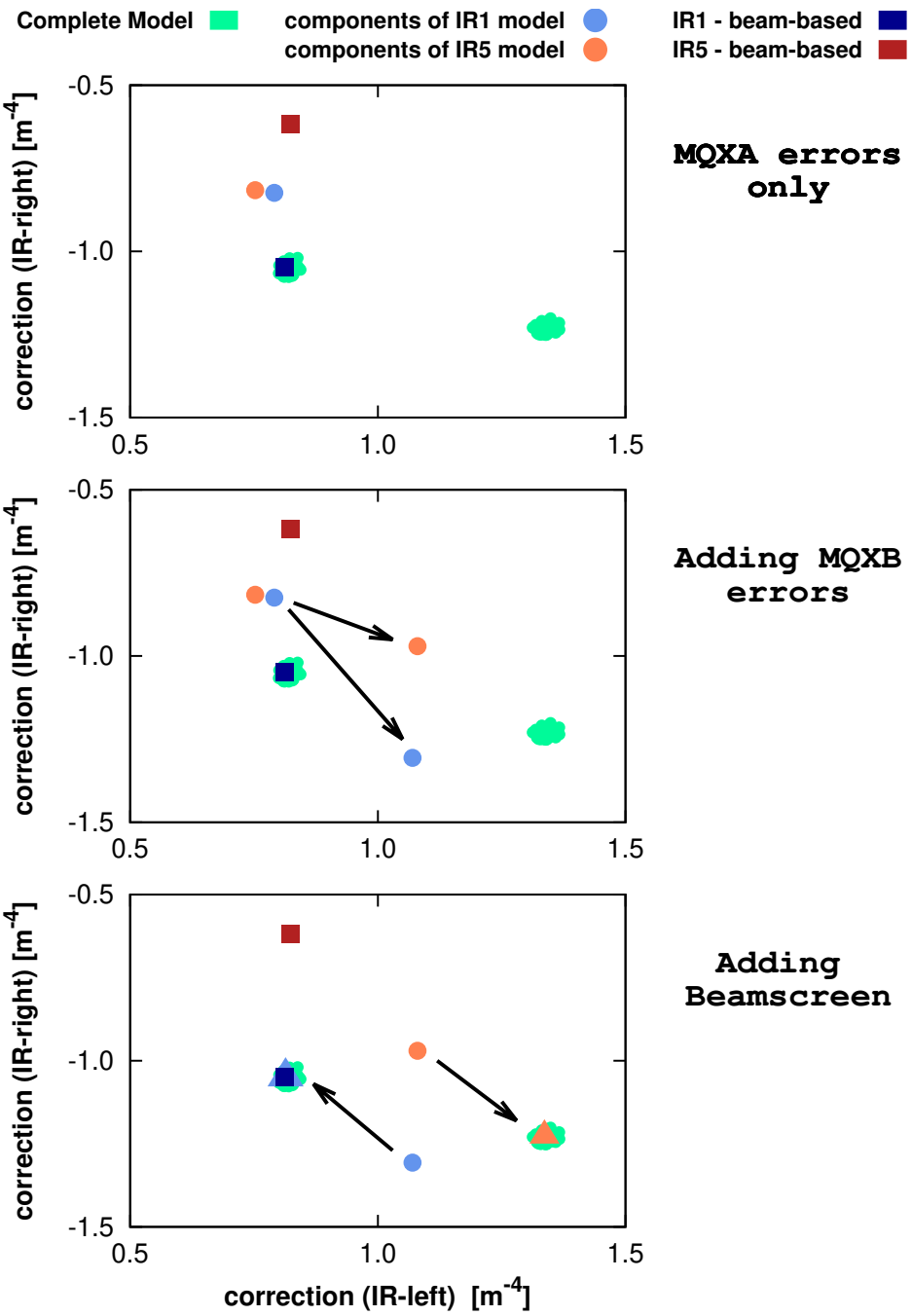

Figure 36: Comparison of beam-based b_4 correction (dark blue/red squares) to model.Complete model prediction is shown in pale green, model corrections including consecutively more sources are shown in pale red/blue circles. Units are non-integrated octupole strength (K_4 in $[\mathrm{m}^{-4}]$). Corrector length is 0.137 m.

Table 7: WISE b_4 errors in LHC. Q1 and Q3 are quadrupoles of type MQXA and Q2a and Q2b of MQXB.

	Q1	Q2a	Q2b	Q3
IR1L	0.882	0.181	0.181	1.255
IR1R	1.017	0.040	0.040	1.270
IR5L	1.512	0.196	0.196	1.414
IR5R	1.451	0.320	0.320	1.503

Table 8: Sum of REFPARM_GEO and beam screen contribution (BMSCR) b_4 components in LHC fidel tables. Q1 and Q3 are quadrupoles of type MQXA and Q2a and Q2b of MQXB [158].

	Q1	Q2a	Q2b	Q3
IR1L	0.882	0.235	0.116	1.255
IR1R	1.017	0.152	-0.070	1.270
IR5L	1.512	0.109	0.279	1.414
IR5R	1.451	0.401	0.240	1.503

9 Impact of the longitudinal distribution of field harmonics on correction settings

The longitudinal distribution of the field harmonics has not been traditionally included in the LHC models. One reason is that such magnetic measurements are only available for MQXA and not for MQXB.

The impact of the longitudinal distribution of b_4 harmonics of MQXA on the octupole corrector strength is compared with experimental data. By design, the Q1 and Q3 magnets (of MQXA type) of LHC IRs feature a systematic b_4 with a longitudinal distribution comparable to that of the b_6. A simple model that splits the magnets in three parts, namely, connection side (CS), body, and non-connection side (NC), is considered to represent the longitudinal distribution of the b_4 and b_6 harmonics of the MQXA magnet type only (called HE+Heads models). Figure 38 shows the locations of the CS sides for the LHC and HL-LHC with blue dots.

The harmonics value and the equivalent magnetic length for the CS and NC parts are reported in table 9.

The average CS and NC measured values are considered the same for all MQXAs installed in IR1 and IR5. As there are no measurement of the contribution of the body, it is deduced from the harmonic value WISE(b_n) integrated over the whole magnet using $\text{WISE}(b_n) - (b_{n,\text{NC}} \times L_{\text{NC}} + b_{n,\text{CS}} \times L_{\text{CS}})/L_{\text{MQXA}}$. L stands for magnetic length of each section of the element and for the sake of the implementation simplicity into LHC model, $L_{\text{MQXA}} = L_{\text{Body}}$. Figure 39 shows

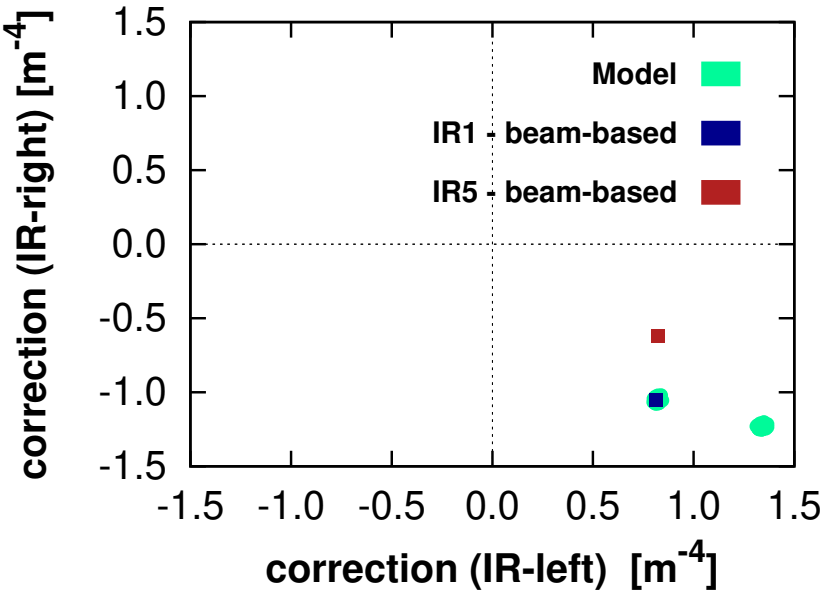

Figure 37: Comparison of beam-based b_4 correction to that of the magnetic model, over the full corrector strength range available in IR1 and IR5. Units are non-integrated octupole strength (K_4 in $[\mathrm{m}^{-4}]$). Corrector length is 0.137 m.

Table 9: b_4 and b_6 harmonics in the MQXA magnets heads according to Ref [164]. CS is the connection side head and NC is the non-connection side one.

b_n	CS (0.34 m) [units]	NC (0.62 m) [units]	standard deviation
b_4	1.17	2.07	0.14
b_6	-0.54	2.59	0.10

the comparison between the beam-based values (blue and red squares) and those computed using the magnetic model (called Hard-edge and shown in blue and orange circles) or with the simple Hard-edge+heads model for the longitudinal distribution of the MQXA b_4 component (cyan and purple circles). In the model, 60 different configurations of the LHC machine are considered, which correspond to the b_2 error component for the inner triplet quadrupoles (MQXA and MQXB) with the same matched tunes. The impact of the MQXA b_4 longitudinal distribution reported in Table 9 is in the order of 10% of the correction values. For IR5, this contribution approaches model and measurement. The MQXB fringe fields are unknown but this study shows that they could have a significant impact on the LHC IR octupolar content.

However, some doubt in the harmonics values accuracy appeared as can be seen by comparing the b_4 on each side (Tab. 9) with the integrated strength (Tab. 7).

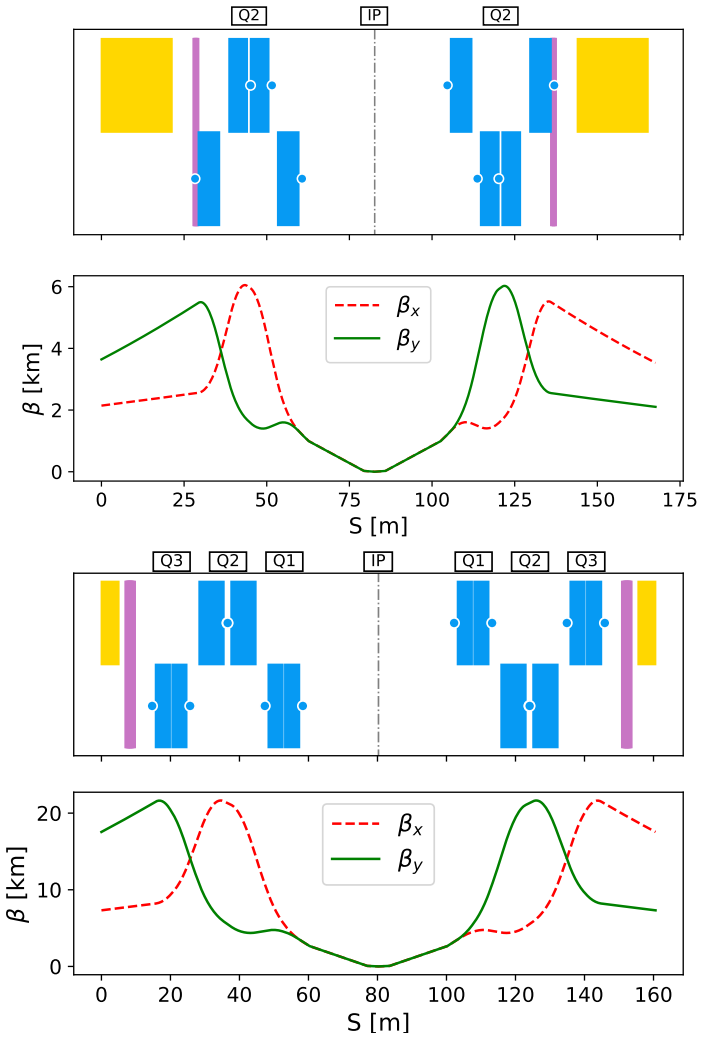

Figure 38: LHC (top) and HL-LHC (bottom) IR sketches. Quadrupoles are in blue. Connection sides (CS) are shown with blue dots.

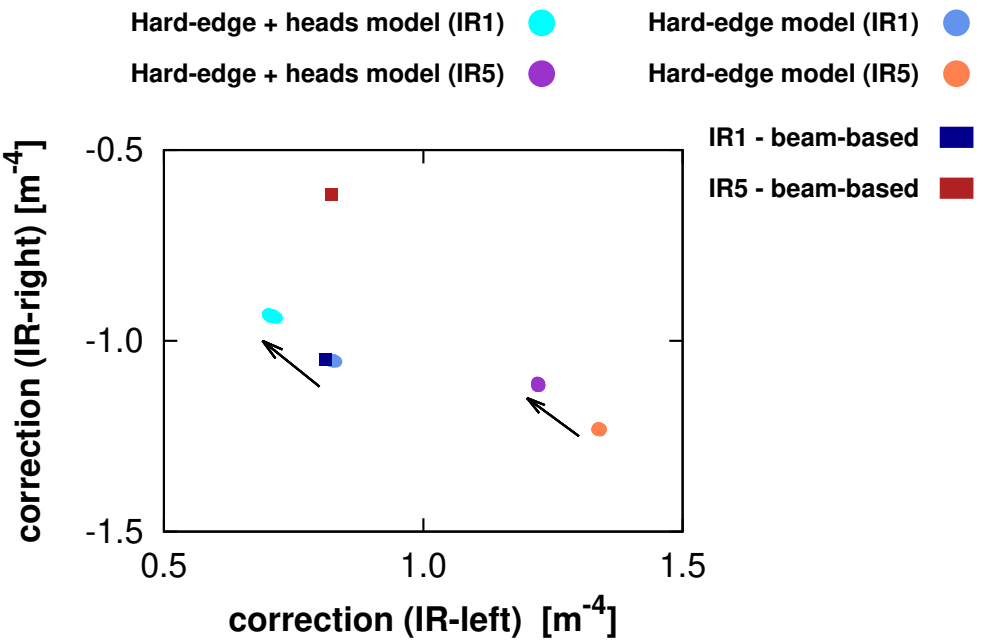

Figure 39: Impact of MQXA fringe fields on the LHC IR octupolar correction. Units are non-integrated octupole strength (K_4 in $[\mathrm{m}^{-4}]$). Corrector length is 0.137 m.

In fact, it appears that the NC side has a stronger b_4 than the body while the CS side is almost the same. This is the opposite of what the structure of the MQXA magnet type should allow and it leads to a re-analysis of the 3D magnetic field model as built. The comparison with the magnetic measurements, performed at KEK, have shown that more realistic values for the CS, NC and body strengths, and magnetic length, for both field harmonics b_4 and b_6, would be as reported in Table 10. These values include also the beam screen contribution, considering also the different orientation in IR1 and IR5 [165].

The predictions for the octupole corrector strengths, using our machine-like 3D model show a very little impact of the Heads contribution, but the total Hard Edge values coming from our 3D model are more symmetrically distributed with respect to the beam-based values, see Fig. 41.

The 3D analysis of the machine-like MQXA shifts the total integrated corrector strengths of about the same amount shown in Fig. 39. The contribution of the Heads (CS and NC side), when properly defined, is smaller. It shows the importance of including the Fringe Fields in the magnetic measurements and model, as described in more detail in Ref. [165].

Concerning the dodecapole correction for the LHC, the impact of the mea-

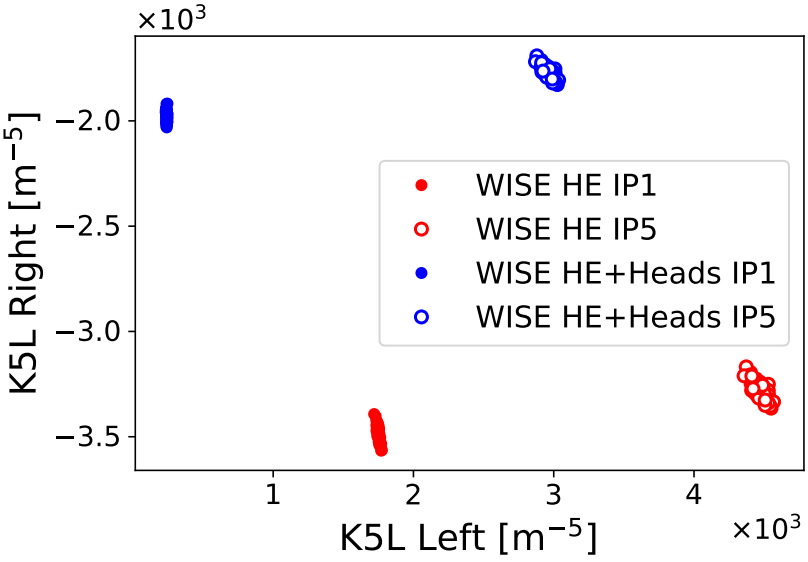

Figure 40: Impact of the MQXA magnet fringe fields on the LHC IR dodecapole correction.

Table 10: Harmonics in the different sections of the MQXA magnet. C+I refers to the magnet with only the iron, 3R1 and 3L5 refer to the Beam Screen type and orientation.

Struc.	Roxie	L	b_4	b_6
C+I	Total	6.37	1.05	0.03
	Body	–	1.03	-0.28
	CS	0.41	1.33	4.45
	NC	0.20	1.01	-0.19
C+I+3L5	Total	6.37	1.19	-0.05
	Body	–	1.17	-0.36
	CS	0.41	1.44	4.39
	NC	0.20	1.21	-0.30
C+I+3R1	Total	6.37	0.93	-0.05
	Body	–	0.90	-0.37
	CS	0.41	1.48	4.68
	NC	0.20	0.82	-0.30

sured MQXA b_6 longitudinal distribution is shown in Fig. 40, using the values reported in Table 11. The effect of considering a different value of b_6 in the body and heads of the MQXA magnet is to reduce the correction strengths between 30% and 80%. This is therefore a dominant effect in the LHC b_6 correction.

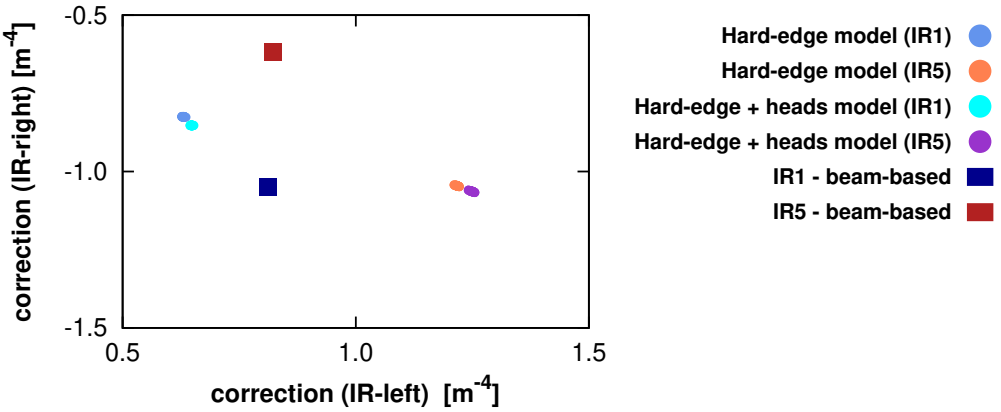

Figure 41: Impact of the machine-like MQXA model on the LHC IR octupolar correction. Units are non-integrated octupole strength (K_4 in $[\mathrm{m}^{-4}]$). Corrector length is 0.137 m.

Table 11: b_6 harmonics in the MQXF magnets heads for the Hard-edge + Heads (top) and Hard-edge+heads Lie2 models (bottom). CS is the connection side head and NC is the non-connection side one.

b_n	CS (0.40 m) [units]	NC (0.341 m) [units]
b_6	8.943	-0.025
b_n	CS (0.62 m) [units]	NC (0.581 m) [units]
b_6	4.8663	-1.030

It is important to understand the sources that can produce a major difference in the b_6 longitudinal distribution. This also motivated the 3D magnetic analysis of the inner triplet magnets. The equivalent lengths and strengths for the b_6 CS and NC side in the MQXA magnet type, that result from our machine-like magnetic model, are reported in Table 10. The impact on the dodecapole correctors strengths is shown in Fig. 7 of Ref. [165]. It is worth noticing that the machine-like 3D model of MQXA predicts a total b_6 harmonics of about a factor 4 lower than the WISE values. For the MQXB magnet type, no measurement or model for the heads is available, making even more uncertain the prediction of the b_6 correction for the LHC. Therefore a magnetic-measurement driven correction of b_6 is not possible in the LHC. Beam-based b_6 corrections will be explored in LHC Run 3 using techniques as presented in the following section.

Concerning HL-LHC, the impact of the longitudinal distribution of the systematic part of the b_6 harmonics (note that b_4 is not systematic and it is unknown) of the inner triplet quadrupoles on the correctors strength has been quantified for HL-LHC optics version 1.4. For this purpose, the magnets of the inner triplet are

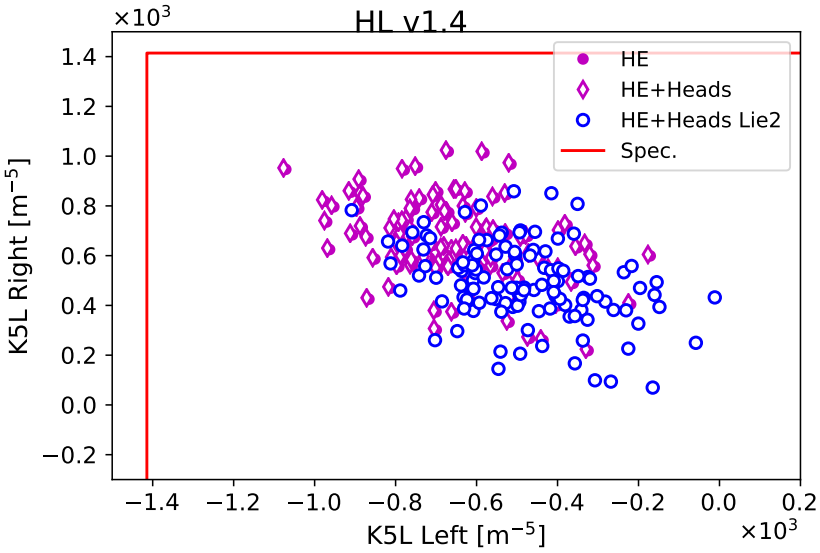

Figure 42: Integrated strength of the b_6 corrector computed for different subdivision of magnet heads and body in IR1 and IR5, with 60 seeds. "Spec." refers to maximum corrector strength.

split in three parts, as in the case of LHC.

Having the longitudinal distribution of the pseudo harmonics for the inner triplet prototype from ROXIE, sampled at 2 cm steps, a second subdivision of the magnet (called HE+Heads Lie2) is derived. The b_6 values in the magnet ends and the equivalent length of the connection side and non-connection side have been defined as the region in the magnet where the main field and the higher-order harmonics start and end with no variation along the longitudinal axis (i.e. where $A_x(x,y,z) \neq 0$ or $A_y(x,y,z) \neq 0$ (i.e. $B_z \neq 0$)), as described in detail in [166].

The impact on the correctors strength is shown in Fig. 42. While for the first subdivision of the magnet the correctors strength is very close to the one computed using the HE model, for the second one a systematic shift of about 11% appears, with respect to the current corrector strength specification (red line in Fig. 42).

The third model compared in Fig. 43, called Lie2, uses a 3D representation of the magnetic field with a 2 cm step size in z for the magnet ends. It allows to take into account not only the longitudinal distribution of the main harmonics, but also the gradient derivatives. As can be seen in Fig. 43, the b_2 gradients derivatives have a negligible impact on the b_6 correctors and the corrector strengths computed with HE+heads Lie2 and Lie2 models are pretty well equivalent. For comparison, the impact of the b_2 gradient derivatives on the octupole correction is predicted to account for 4% of the maximum corrector strength. Furthermore from tracking point of view, a complementary study has shown that a good longitudinal sampling

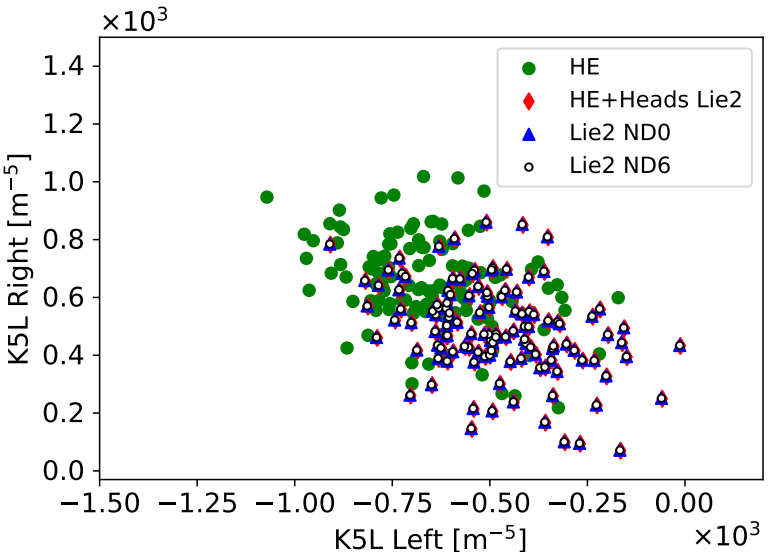

Figure 43: Integrated strength of the b_6 corrector computed for different models in IR1 and IR5, with 60 seeds.

for the field harmonics is 2 cm, in order to be able to evaluate this B_z contribution and to have a negligible impact on the tracking results [167].

10 Decapole and dodecapole correction

To guarantee effective exploitation of the HL-LHC, numerous simulation-based studies predict that correction of decapole and dodecapole nonlinearities will be required in the low-β insertions [2, 168, 3]. As an example, Fig. 44 (reproduced from [169]) shows the reduction of simulated DA if dodecapole errors in the ATLAS and CMS insertion triplets were left uncorrected. The simulation was performed in SixTrack [170] for the baseline configuration at end-of-squeeze ($\beta^* = 0.15\,\mathrm{m}$) including also the beam-beam force. All nonlinear and linear-coupling sources other than normal dodecapole errors in the triplets are assumed to be perfectly corrected (within the capabilities of the lattice) by the corrector package magnets. The figure shows minimum DA after 10^6 turns (1.5 minutes) over sixty instances (called 'seeds') of magnetic field errors to account for potential uncertainties in the magnetic measurements. Failure to correct even just the normal dodecapole errors leads to a substantial 25 % reduction in the predicted minimum DA on this timescale, which poses an unacceptable risk to productive operation.

Given the experience of sextupole and octupole correction in the LHC, methods for beam-based measurement and correction of the higher order nonlinearities

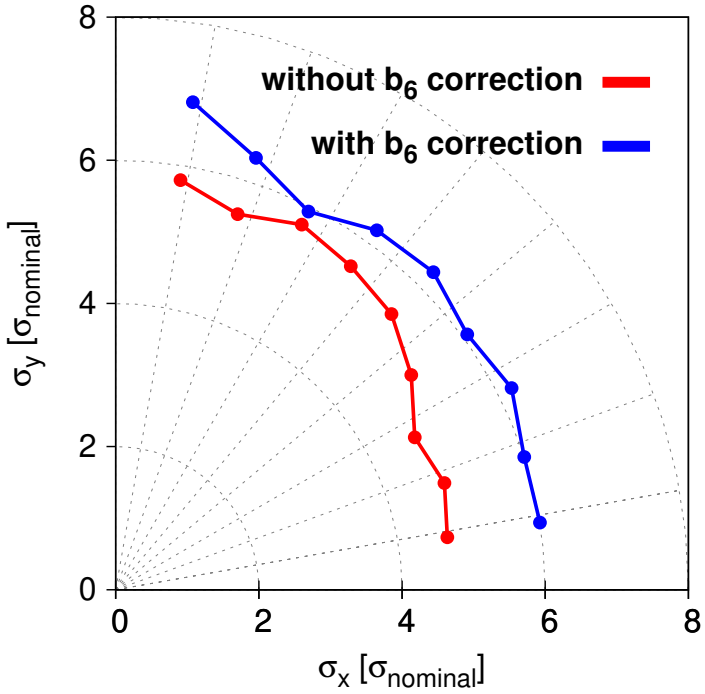

Figure 44: Simulated DA of the HL-LHC in collision at end-of-squeeze ($\beta^* =$ 0.15 m, with beam-beam included), with (blue) and without (red) correction of normal dodecapole errors in the ATLAS and CMS insertion triplets.

are also desirable, both to validate corrections based upon the magnetic model, and in case of discrepancies with machine observations, refine the original corrections. To date, three main avenues for beam-based techniques have been considered, namely: amplitude-detuning methods, RDTs, and dynamic aperture. These studies have entailed both numerical tests as well as initial experimental tests at the LHC.

10.1 Detuning-based methods

Normal dodecapole errors generate a quadratic change of tune with action, i.e. second-order detuning. They also feed-down to generate a normal octupole error (producing a linear change of tune with the action, i.e. first-order detuning) with a quadratic dependence on either a horizontal or vertical orbit offset. To first order in the perturbation, decapole errors do not generate detuning (though some quadratic detuning - for example - can be generated via terms quadratic in the decapole strength and through cross-terms with other multipoles, although this is small compared to the expected quadratic detuning generated by the do-

decapoles). Decapoles can, however, generate a first-order detuning with a linear dependence on the orbit offset. Normal decapoles feed-down to normal octupole with a horizontal offset, while skew decapoles feed-down to normal octupole with a vertical offset. It is possible, therefore, to draw a direct analogy between normal/skew decapole and normal dodecapole measurement, and the measurement of normal/skew sextupole and normal octupole errors in LHC. In the latter case, global octupole strength is constrained via first-order detuning, with the balance of corrector strength between IR1 and IR5 being determined via the quadratic feed-down to tune, with sextupole errors measured via linear feed-down to tune. In the higher-order case, the global b_6 can be constrained through the measurement of second-order detuning, with the local distribution in IR1 and IR5 determined via quadratic feed-down to first-order detuning, while normal and skew decapole errors can be identified via linear feed-down to first-order detuning as a function of the crossing-angle. However, the measurement of second-order detuning and feed-down to first-order detuning represent a much more challenging operation than the lower-order equivalent. Nonetheless, the initial beam tests of these methods were performed at top energy in the LHC.

Figure 45 shows histograms of the predicted second-order detuning in the HL-LHC at $\beta^* = 0.15\,\mathrm{m}$ at flat-orbit. Histograms are shown for two configurations of the b_6 errors: a systematic part of $b_6 = -0.64\,\mathrm{units}$ together with a random part of $1\,\mathrm{unit}$ (blue); and a systematic part of $b_6 = -4\,\mathrm{units}$ together with a random part of $1\,\mathrm{unit}$ (orange).

To test the viability of second-order detuning as observable for b_6 errors an MD was performed in the LHC at $\beta^* = 0.4\,\mathrm{m}$, with dodecapole sources artificially enhanced via the b_6 correctors in the ATLAS and CMS insertions. This was used to generate a second-order detuning representative of that predicted at $\beta^* = 0.15\,\mathrm{m}$, specifically, MCTX were powered to generate a detuning of $|4.5 \times 10^{12}|\ \mathrm{m}^{-2}$). Sextupole and octupole corrections determined during commissioning were applied. A detailed description of the MD is found in [171].

Figure 46 shows the outcome of the detuning measurement with enhanced b_6 (black/red) contrasted to a measurement with depowered dodecapole correctors (blue). Data shown in the plot corresponds to the difference between the natural tune determined from spectral analysis of the AC-dipole excitation, and the unkicked ($J = 0\,\mu\mathrm{m}$) tune measured in the LHC BBQ. The difference with the BBQ tune measurement is taken to eliminate the drifts or shifts of the natural tune over time, from the detuning with amplitude measurement. In the absence of enhanced b_6, no second-order detuning is observed in the LHC. With enhanced b_6 however, a quadratic component to the variation of tune with amplitude can be observed.

To determine the second-order detuning coefficient, polynomial fits were performed on the enhanced b_6 measurement. The general form of the fit is given by

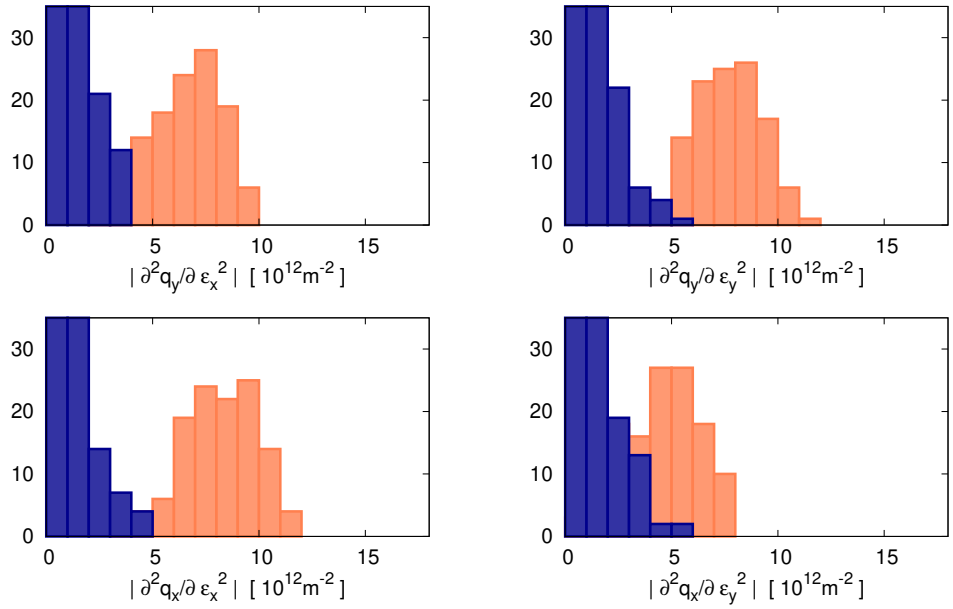

Figure 45: Predicted quadratic detuning coefficients for the at $\beta^* = 0.15$ m. Histograms are shown over sixty instances of the field errors. Two configurations of the systematic part of the normal dodecapole error in the magnet body are considered: the initial target value (blue), with systematic and random parts of -0.64 and 1 units, respectively; and a more pessimistic expectation based on early magnet cross-section designs (red) with systematic and random parts of -4 and 1 units, respectively.

$$\Delta Q_0 + \left(2 \times \frac{\partial Q}{\partial (2J)}\right)(2J) + \left(3 \times \frac{1}{2!}\frac{\partial^2 Q}{\partial (2J)^2}\right)(2J)^2 \tag{9}$$

where free parameters in the fit are the offset of the tune from the BBQ value at zero-action (ΔQ_0), the first order detuning coefficient ($\frac{\partial Q}{\partial (2J)}$) and the second-order detuning coefficient ($\frac{\partial^2 Q}{\partial (2J)^2}$). The 2! factor in the fit arises from the description of the amplitude detuning in terms of a Taylor expansion about the unperturbed tune (in order to be consistent with codes such as PTC). When determining the detuning coefficients of driven oscillations it is also necessary to account for the enhancement of the direct detuning terms obtained with an AC-dipole. Factors $2\times$ and $3\times$ in the first- and second-order coefficient terms correspond to this enhancement due to driven oscillation, such that the fitted detuning coefficients correspond to that expected for the free motion.

Several forms of fit were tested (Eqs. 10–12), with the outcome for the quadratic

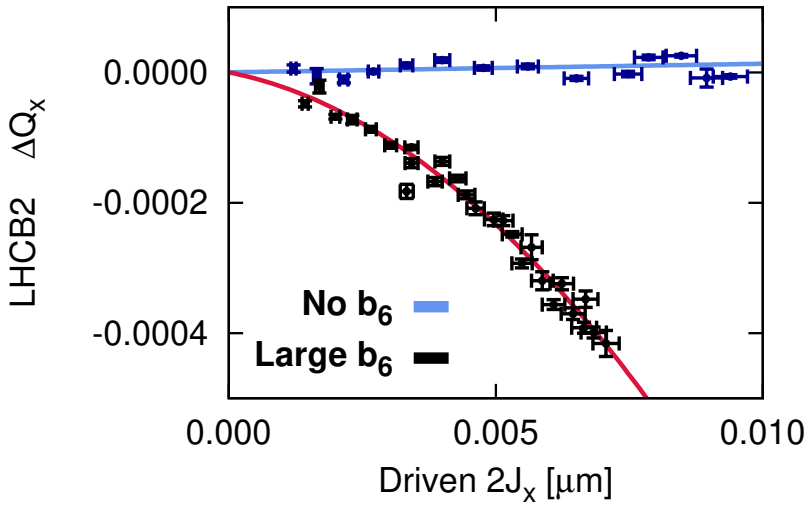

Figure 46: Measurement of tune change with action of AC-dipole excitation, with and without an artificially enhanced dodecapole content of the ATLAS and CMS insertions.

detuning term presented in Table 12. A linear fit (Eq. 10), with no second-order term, was performed to confirm the observed detuning was incompatible with a linear variation of tune with action. Considering Table 12, the χ^2_{red} statistic was significantly worse for the linear fit than for fits including the quadratic term, demonstrating the clear identification of quadratic detuning with the enhanced b_6 sources.

Two quadratic fits (Eqs. (11)–(12)) were performed. In the first case, only the linear and quadratic detuning coefficients were left as free parameters, while the offset of the unkicked tune (the difference of the tune to the BBQ value at zero action) was forced to 0.0. In the latter case the offset of the tune (ΔQ_0) was also fit as a free parameter (which can correspond, for example, to an error in the adjustment of the AC-dipole measurement with BBQ data, or to the influence of any cross-term detuning due to any small constant excitation in the action-plane not under consideration - the vertical plane in this case). In an ideal case Eqs. (11) and (12) would return the same quadratic detuning coefficient, in practice any difference between the fits should also help quantify the precision of the inferred quadratic

term.

$$\Delta Q_0 + \left(2 \times \frac{\partial Q}{\partial (2J)}\right)(2J) \tag{10}$$

$$0.0 + \left(2 \times \frac{\partial Q}{\partial (2J)}\right)(2J) + \left(3 \times \frac{1}{2!}\frac{\partial^2 Q}{\partial (2J)^2}\right)(2J)^2 \tag{11}$$

$$\Delta Q_0 + \left(2 \times \frac{\partial Q}{\partial (2J)}\right)(2J) + \left(3 \times \frac{1}{2!}\frac{\partial^2 Q}{\partial (2J)^2}\right)(2J)^2 \tag{12}$$

Table 12: Second-order detuning coefficients and reduced chi-squared statistics obtained from fits to the AC-dipole detuning data. The expected second-order detuning coefficient obtained from PTC_NORMAL for the applied powering of MCTX is also shown.

Fit form	χ^2_{red}	$\partial^2 Q_x/\partial(2J_x)^2$ $[10^{12}\mathrm{m}^{-2}]$
Expected value	**N/A**	-4.5
Eq. (10)	16.1	0.0
Eq. (11)	6.3	-4.1 ± 0.4
Eq. (12)	5.8	-5.5 ± 1

Both fits including the quadratic coefficient agree with the expected value of the detuning, within the standard error of the fitted coefficient, and within 20 % of the expected value. Fits with and without the unperturbed tune as a free parameter were consistent within 20 %. The measurement implies a 20 % precision of the global constraint on the IR1+IR5 b_6 correction should be achievable at end-of-squeeze, for a representative configuration of the expected dodecapole errors. It is also worth noting that the detuning measurement shown in Fig. 46 was performed over an extremely small action range, due to blowup of the bunch emittance during earlier studies. Typical LHC detuning measurements have utilised a significantly larger action range ($2J \leq 0.02\,\mu\mathrm{m}$), which should allow a further improvement in the measurement of the quadratic detuning coefficient provided small emittance bunches can be preserved for use in high-order optics commissioning measurements.

While the measurement of second-order detuning described above does appear to be a promising technique for studying dodecapole errors in the experimental IRs, it suffers from two significant weaknesses. Firstly, as a global variable it

cannot distinguish between errors in different IRs. Secondly, given the extremely strong scaling of second-order detuning with $(\beta^*)^{-3}$ the quadratic change of tune with action is only expected to be measurable at very low-β^*. However, there may exist motivations to correct the higher-order errors even for larger $\beta^* \leq 0.4\,\mathrm{m}$. In particular, if it is ever desired to squeeze nominal intensity beams to $\beta^* \leq 0.4\,\mathrm{m}$ before collision, there may be insufficient margin in the strength of Landau octupole to maintain the beams stable due to the presence of decapolar and dodecapolar feed-down effects. For example, Fig. 10 demonstrated that an equivalent Landau octupole detuning of up to 250 A at flattop can be generated via feed-down from a 190 µrad crossing-scheme at $\beta^* = 0.4\,\mathrm{m}$. Should such an operational scenario ever arise, then to reduce the detuning within the 50 A equivalent current margin anticipated at high-intensity, both decapole and dodecapole corrections may be necessary (the predicted detuning generated by feed-down after decapole and dodecapole correction at $\beta^* = 0.4\,\mathrm{m}$ is shown in green in Fig. 10). Further, high-order corrections may be desired for improved detuning-related reductions to the performance of beam-instrumentation (particularly the BBQ), to facilitate optics corrections with the crossing-scheme applied, or in case AC-dipole kick amplitude is limited by beam losses. These challenges arising from high-order errors were discussed in further detail in [16].

Measurement of changes to first-order amplitude detuning as a function of crossing-angle can overcome these limitations. Crossing-angle can be varied in IR1 and IR5 independently, allowing separate measurements of the feed-down from each IR, while the weaker scaling of first-order detuning with $(\beta^*)^{-2}$ makes the observable more viable at higher β^* early in the squeeze compared to second-order detuning. Multiple beam-based measurements of shifts to first-order detuning with changes in crossing-angle have been performed in the LHC at top energy, both to test the viability of the measurement technique, and to study any potential higher-order errors present in the existing LHC triplets. An example of one such beam-based study is shown in Fig. 47 which shows a detuning measurement performed at flat orbit (blue), with IR1 and IR5 crossing angles applied (black), and with only the crossing angle in IR5 applied (red). Measurements were performed at $\beta^* = 0.3\,\mathrm{m}$ at the end of 2018 LHC commissioning, and during a dedicated MD early in the start 2018 LHC run. The applied crossing-angles were 160 µrad in the IR1 and IR5 insertions. At flat orbit the detuning is consistent with zero (normal octupole corrections have been applied), consistent with measurements performed in previous years. Table 13 presents the direct detuning coefficients measured with crossing-angle bumps applied.

Figure 47 and Table 13 demonstrate that a comparable quality of detuning measurement can be obtained with the crossing-angle orbit bumps applied, as is obtained with flat-orbit. An in-depth review of LHC detuning measurements at top energy is given in [172], which shows comparable measurement quality has

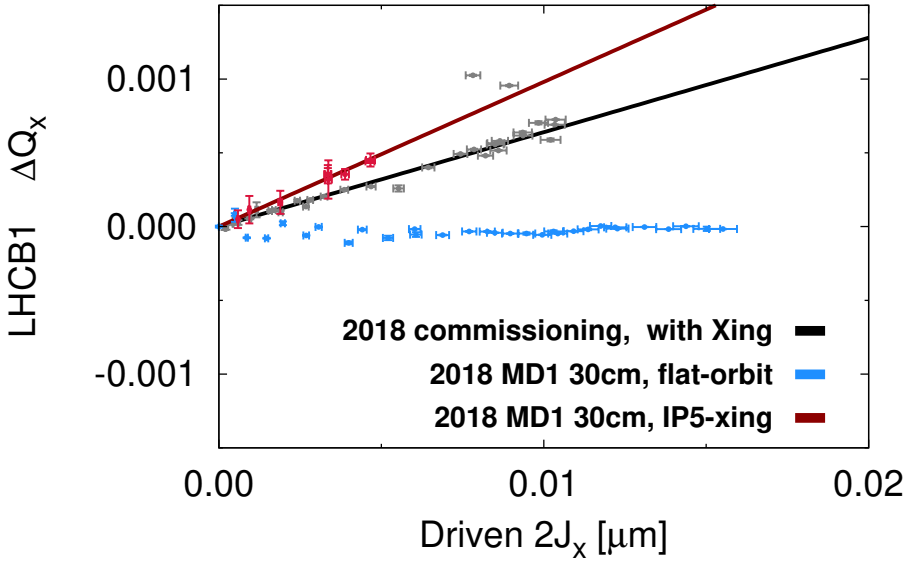

Figure 47: Example of amplitude detuning measurements performed for various configurations of the crossing-scheme in the LHC at $\beta^* = 0.3\,\mathrm{m}$.

Table 13: Direct detuning coefficients measured in the LHC at $\beta^* = 0.3\,\mathrm{m}$ with the full LHC crossing-scheme applied and with only the IR5 crossing-scheme applied.

	Detuning $[10^3\mathrm{m}^{-1}]$			
	LHCB1		LHCB2	
	Full Xing scheme	IR5 only	Full Xing scheme	IR5 only
$\partial Q_x/\partial 2J_x$	$+32 \pm 2$	$+46 \pm 3$	-5 ± 1	$+2 \pm 1$
$\partial Q_y/\partial 2J_y$	-40 ± 1	$+5 \pm 2$	$+20 \pm 4$	$+13 \pm 2$

been achieved in multiple studies. Shifts in the detuning coefficients at a level of $20 \times 10^3\,\mathrm{m}^{-1}$, due to feed-down in the experimental IRs, have been clearly measured in the LHC. The precise source of these shifts in the LHC remains to be determined, and it will require multiple measurements at different crossing angles to disentangle decapolar and dodecapolar components of the observed feed-down.

To explore the viability of the measurement of first-order detuning versus crossing angle as observable for decapole and dodecapole errors at large β^*, a series of simulated measurements were considered for the HL-LHC at $\beta^* = 0.4\,\mathrm{m}$. Linear and quadratic variations of the detuning coefficients with crossing-angle in both IR1 and IR5 were obtained from the model. From these model variations, fake measurement data was then generated for a scan of detuning coefficients vs crossing angle, based upon an assumed five detuning measurements performed

over a $\pm 250\,\mu$rad range. Random Gaussian errors were added to the crossing-angle of each detuning "measurement", with $\sigma_{xing} = 10\,\mu$rad, truncated at $3\,\sigma$. Random Gaussian errors were also added to the detuning value, truncated to $3\,\sigma$, with $\sigma = 4000\,\mathrm{m}^{-1}$ (typical uncertainties on detuning measurements can be seen in Table 13). Artificial measurement data was generated for 100 instances of each of the 60 WISE seeds. Figure 48 shows two examples of the artificial measurements of detuning vs crossing angle, with the left and right plots showing particularly good and bad instances of the fake data respectively.

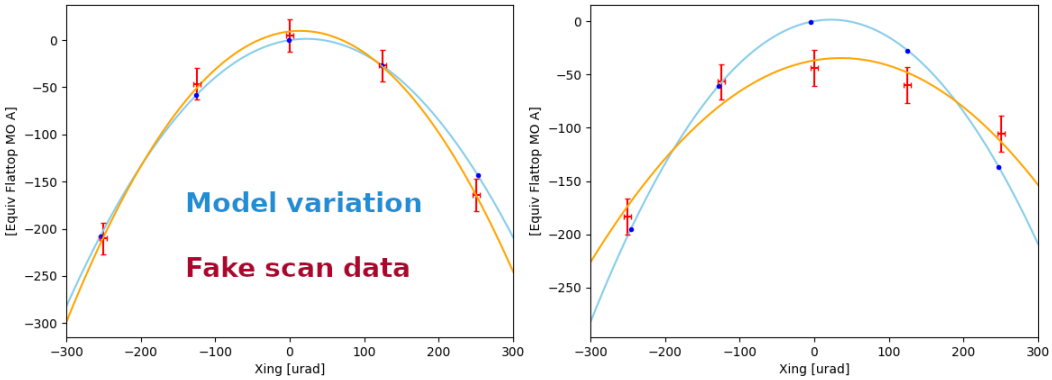

Figure 48: Two examples of artificial measurements of first-order detuning versus crossing angle in IR5 at $\beta^* = 0.4\,$m. The true variation of detuning is shown in blue, and the artificial measurement including errors on both the crossing angle and detuning value are shown in red.

Simulated measurements underwent a polynomial fit to obtain the linear and quadratic variations of detuning with crossing-angle. To test the artificial measurement quality, the fitted variations were used to infer the detuning value at the operational crossing angle (assumed to be 190 µrad), which was compared to the true value obtained from the model. The difference between measured and true detuning at the operational crossing angle was then quantified in terms of the equivalent Landau octupole current necessary to generate that shift to amplitude detuning at flattop. Figure 49 (blue data) shows a histogram of the difference obtained for artificial measurement of the vertical direct detuning coefficient of IR5 (at $\beta^* = 0.4\,$m, 190 µrad). In the worst cases, a discrepancy of the true detuning coefficient is seen at the level of 40 A equivalent MO current (with comparable distributions seen across the detuning terms and IRs). This implies that even at a relatively large $\beta^* \approx 0.4\,$m the precision of a detuning vs crossing-angle measurement appears a viable option to define and test decapole and dodecapole corrections.

The method is particularly sensitive to the quality of the individual detuning measurements. Reducing the σ of the random detuning errors from $4 \times 10^3\,\mathrm{m}^{-1}$

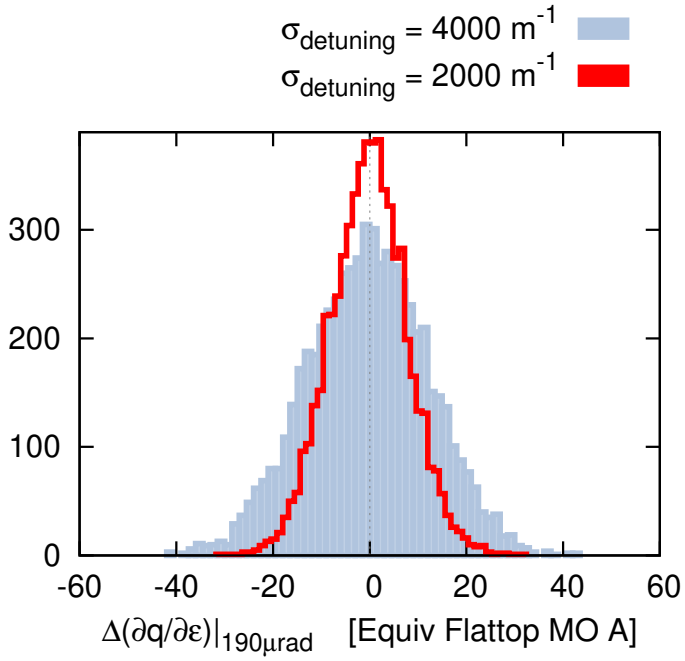

Figure 49: Difference obtained at $\beta^* = 0.4\,\mathrm{m}$, 190 µrad, between the direct vertical detuning value via fits to artificial measurement of detuning vs crossing angle, versus the true value obtained from the model. Histograms are shown for artificial measurements with applied random detuning errors of $\sigma_{detuning} = 4000\,\mathrm{m}^{-1}$ (pale blue) and $\sigma_{detuning} = 2000\,\mathrm{m}^{-1}$ (red).

to $2 \times 10^3\,\mathrm{m}$ (which is representative of the uncertainty on a good quality detuning measurement) can significantly improve the precision of the fitted linear and quadratic variations. Figure 49 (red data) shows a histogram of the difference to the true model value obtained with this reduced uncertainty on the detuning values. Performance was also significantly improved by increasing the number of crossing-angles measured.

Measurement of detuning variation with crossing angle appears to have significant potential as observable for decapole and dodecapole errors, even at β^* as high as 0.4 m. Only limited tests have been performed at the LHC to date, however, and further tests and exploitation of this method will be a priority in Run 3. The method does, however, suffer from a significant weakness in terms of the time investment necessary. A high-quality detuning measurement, such as that seen in black in Fig. 47 necessitates many AC-dipole excitations (in the highlighted example ~ 20 kicks were performed at varying amplitudes). Scaling this to a realistic measurement scenario implies a significant number of excitations:

$$
\begin{aligned}
&20(\text{kicks}) \\
&\qquad \times 5(\text{crossing angles}) \\
&\qquad \times 2(\text{detuning coefficient}) \\
&\qquad \times 2(\text{IRs}) \\
&\qquad \times 2(\text{measurements : before/after correction}) \\
&\approx 800(\text{kicks/beam})
\end{aligned}
$$

This would at present constitute a significant number of shifts dedicated to the measurements themselves, as well as a very substantial post-processing effort.

10.2 Direct DA measurement

Dynamic aperture poses significant challenges in regard to a quantitative determination of high-order corrections. As a global observable, it may struggle to distinguish optimal corrections in the different IRs, and with many contributing effects it may be difficult to isolate any direct impact of different multipoles. Nonetheless, it represents in many circumstances the ultimate figure of merit for nonlinear correction in the HL-LHC, and as illustrated in Fig. 44 has the potential for a direct operational impact via high-order errors. As such, direct measurement of changes to DA under the influence of decapole and dodecapole corrections can represent a significant observable for the validation of corrections determined through magnetic measurements or via alternative beam-based techniques.

Conventional DA measurements (based upon measurement of losses following single and large-amplitude kicks) are not viable at top energy in the LHC due to machine protection concerns, and the beam-destructive nature of the measurement, making repeated excitation with single kicks impractical. An alternative DA measurement has been demonstrated in the LHC at injection [173], based upon heating the beam to a large emittance with the transverse damper and observing beam losses upon changes in the nonlinear correctors [173]. Dedicated machine tests were performed in the LHC in 2017 to demonstrate this technique at top-energy in the LHC, and make an initial exploration of its viability for study of high-order corrections. A detailed report of the measurement procedure is provided in [174]. Measurements were performed at flat-orbit in LHC ($\beta^* = 0.4\,\text{m}$), with enhanced b_6, generated via uniform powering of the MCTX correctors. A discussion of the outcome of the measurements in the context of tests of a diffusion model for DA evolution are discussed in [175].

Several bunches were heated to $\sim 25\,\mu\text{m}$ emittance in the H, V, and H+V planes, with depowered MCTX. With dodecapoles depowered no losses from dynamic aperture were observed. Dodecapole correctors were then uniformly pow-

ered to increase artificially the dodecapole sources in the ATLAS and CMS insertions. Figure 50 shows the measured intensity as dodecapole correctors (green) were powered on, then as all sextupole and octupole IR-correctors used in operation were powered off (red area).

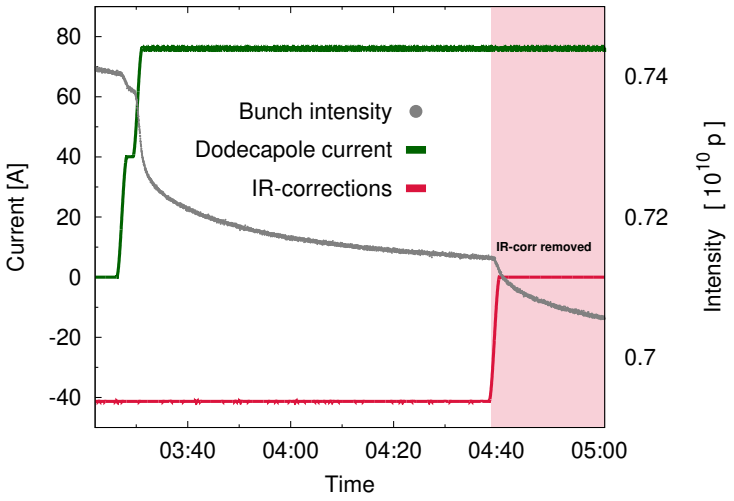

Figure 50: Measurement of beam intensity of heated bunch with $\varepsilon_x = \varepsilon_y = 25\,\mu\text{m}$ as dodecapole correctors in IR1 and IR5 are uniformly powered on (green curve), then as operational corrections for normal/skew sextupole and octupole errors in IR1 and IR5 are removed (red region).

Dodecapole strength was increased in two steps of $\approx 40\,\text{A}$ ($\Delta K_6 = 18 \times 10^{-3}\,\text{m}^{-6}$). Clearly measurable beam losses, well outside the noise on the BCT measurement, could be observed following each step, due to reduction of the dynamic aperture (as evidenced by the characteristic slow beam loss observed to persist after the end of the MCTX trims). Shifts to dodecapole corrector strengths employed in this test are significantly larger than the multipole errors expected in HL-LHC, however the dodecapole perturbation scales extremely strongly with β^3 at the location of the error, which in the experimental insertion means the perturbation scales as $\approx (\beta^*)^{-3}$. Thus, a change in corrector powering of 40 A ($18 \times 10^{-3}\,\text{m}^{-6}$) at $\beta^* = 0.4\,\text{m}$ is comparable to a $\approx 2\,\text{A}$ ($\approx 2 \times 10^3\,\text{m}^{-6}$) at $\beta^* = 0.15\,\text{m}$, or to $\approx 0.5\,\text{A}$ ($\approx 0.3 \times 10^3\,\text{m}^{-6}$) at $\beta^* = 0.10\,\text{m}$. While the corrector package will change between LHC and HL-LHC, the equivalent strengths of the perturbation at smaller β^* are representative of the dodecapole errors anticipated in HL-LHC. This implies that qualitative validation of the high-order corrections should be possible using a DA measurement technique based upon heating of pilot bunches to large emittance and observing beam losses as the nonlinear corrections are removed. That is: if dodecapole (or indeed lower-order) correctors are well defined and

have a beneficial impact on the dynamic aperture, the reduction to DA upon their removal should be observable via the method demonstrated above. This also implies that a direct optimisation of the DA via the dodecapole correctors should be possible in the eventuality that problems with lifetime are observed at end-of-squeeze.

More quantitative analysis of the DA is also possible by comparing DA measurements with predictions from numerical simulations. Figure 51 shows the 10^6 turn DA for the enhanced dodecapole configuration (with MCTX powered to 80 A) predicted via SixTrack simulations of the LHC model. An asymmetry between horizontal and vertical DA is predicted, with significantly smaller DA in the vertical plane. Figure 52 compares fractional beam-loss observed following the increase in dodecapole strength to 80 A for bunches blown up in only the horizontal or vertical planes. The pattern of observed losses, with no significant beam loss seen for the bunch with large horizontal emittance, but significant losses for the bunch with the large vertical emittance, matches that expected from the model prediction. More detailed quantitative comparison of these measurements are reported in [175], where a good agreement is observed. Similarly, [173] reports quantitative comparisons between model and measured DA for studies performed by this method at injection in the LHC, where an agreement was seen at the level of $\sim 10\,\%$ for well-defined changes in octupole powering. Such studies suggest that quantitative study and measurement of dynamic aperture may also become viable as a method to validate the error model. It is worth noting that such quantitative successes have so far only been achieved in cases with a single dominant multipole error. Nevertheless, this is one of the most important cases of application. Of course, it should be assessed whether the viability of quantitative DA analysis for high-order correction may be limited by the understanding and correction quality of the lower orders for example. Nonetheless, in the context of a large systematic dodecapole error in the triplets, the direct study of DA represents an interesting technique for validation of the error model and corrections.

10.3 Short-Term Dynamic Aperture of Driven Oscillations

The short-term dynamic aperture of a beam under the influence of driven oscillations from an AC-dipole is, in general, substantially smaller than the long-term DA of free betatron oscillations. A discussion of the concept of dynamic aperture for driven oscillations is provided in [176]. This can pose a challenge to optics measurement and commissioning (for example [151]), but as with free-DA can also provide an observable to test the impact of b_6 errors and their corrections. In parallel with the machine studies on free-DA presented in the previous section, studies were also performed on the driven DA. Beam-losses upon excitation for ten thousand turns with an AC-dipole (constituting two thousand turns of ramp-up

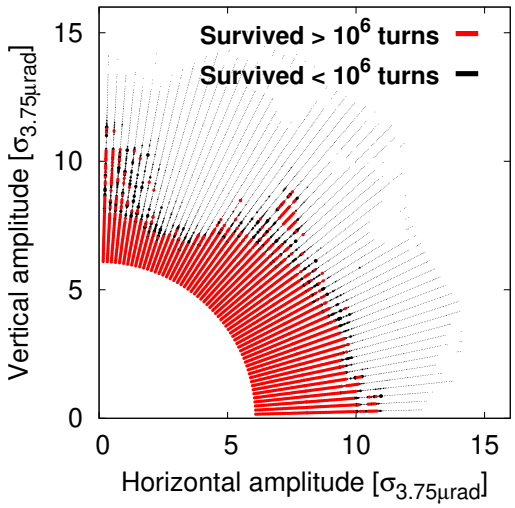

Figure 51: SixTrack simulation of the 10^6 turn LHC DA, with MCTX powered to 80 A and all lower-order corrections applied.

of the driven oscillation, six thousand turns flat top excitation, and two thousand turns of ramp down of the excitation amplitude) were examined as a function of the AC-dipole kick amplitude, for configurations of the LHC at $\beta^* = 0.4\,\mathrm{m}$ with and without the enhanced configuration of the b_6 sources (i.e. with MCTX powered to 76 A). A detailed review of the study is provided in [174]. Figure 53 shows measured beam losses upon AC-dipole excitation with (red) and without (green) the enhanced b_6 sources. A clearly measurable increase to the beam-losses can be observed in the enhanced b_6 configuration. As the measured emittance (via BSRT) remained constant between the measurements [174], the increased losses upon introduction of the b_6 correspond to a measurable reduction in the dynamic aperture of the forced oscillations.

An expression for beam-losses upon AC-dipole excitation as a function of the action of the DA and kick is given in Eq. (14) of [176]. This can be re-expressed in terms of kick amplitudes in units of σ,

$$\frac{\Delta I}{I} = e^{\frac{1}{2}\frac{\varepsilon_{nom}}{\varepsilon_{beam}}\left(K^2_{forced} - D^2_{forced}\right)} \tag{13}$$

where $\varepsilon_{\mathrm{nom}}$ is the nominal beam emittance (3.75 µm for the LHC), $\varepsilon_{\mathrm{beam}}$ is the measured beam emittance, K is the AC-dipole kick amplitude in units of $[\sigma_{\mathrm{nom}}]$ (as defined by $\varepsilon_{\mathrm{nom}}$), and D_{forced} is the DA of the forced oscillation in units of $[\sigma_{\mathrm{nom}}]$. In practice, for the extremely small forced DA considered here (where losses occur at kick amplitudes comparable with the beam size), this relation can become problematic for small actions. At zero AC-dipole kick action, the beam

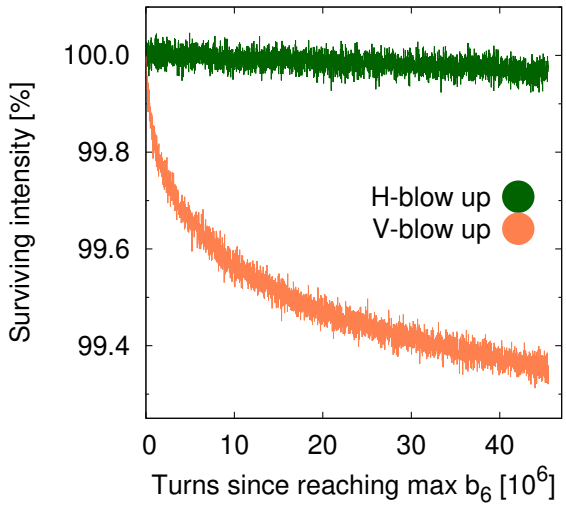

Figure 52: Fractional beam-loss observed after MCTX were powered to 80 A. Losses are shown for two bunches: one blown-up in only the H plane (green), and one blown-up in only the V plane (orange).

loss reduces to,

$$\frac{\Delta I}{I} = e^{-\frac{1}{2}\frac{\varepsilon_{\text{nom}}}{\varepsilon_{\text{beam}}}D^2_{\text{forced}}}, \tag{14}$$

which is equivalent to the loss relation for free-DA described in [177], but with D_{forced} defining the losses. In the case of small D_{forced} this can imply non-negligible beam losses at zero action, which are nonphysical since in the absence of an AC-dipole excitation losses should be defined by the DA of the free betatron motion. One modification to Eq. (13) which can be considered is,

$$\frac{\Delta I}{I} = e^{\frac{1}{2}\frac{\varepsilon_{\text{nom}}}{\varepsilon_{\text{beam}}}\left(K^2_{\text{forced}}-D^2_{\text{forced}}\right)} - e^{-\frac{1}{2}\frac{\varepsilon_{\text{nom}}}{\varepsilon_{\text{beam}}}D^2_{\text{forced}}} \tag{15}$$

where the second term removes the nonphysical losses predicted at zero AC-dipole action due to D_{forced} and losses from the free DA (which is in general much larger than the forced DA) are assumed to be negligible (one could consider adding an additional term to account also for free-DA losses, however for the optics configuration used here, the free DA inferred from simulations and beam-based measurements was large enough that any such contribution is negligible). In practice, the consideration of losses at zero action is only relevant for very small forced DA, or very large emittances, and was not relevant for the studies presented in [176]. If the analysis of small D_{forced} proves of interest in the context of strong nonlinearities at end-of-squeeze in the HL-LHC, further consideration of the expected losses at small kick amplitude may be of interest.

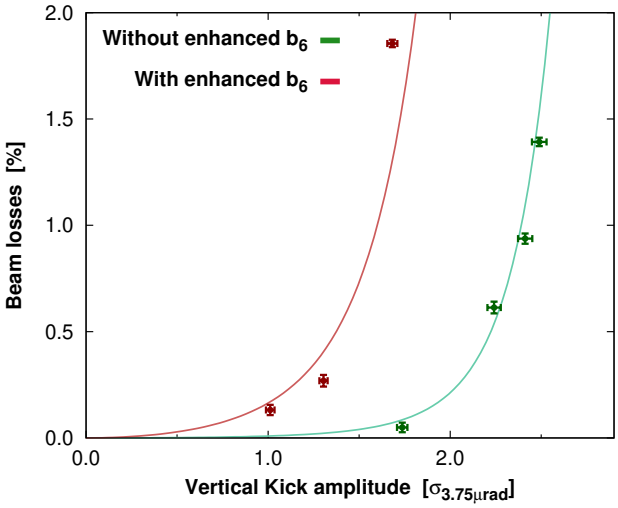

Figure 53: Measured beam-losses upon AC-dipole excitation with (red) and without (green) artificially enhanced b_6 sources in the ATLAS and CMS insertions of the LHC at $\beta^* = 0.4\,\mathrm{m}$. Solid lines show the beam-loss expected for a single-Gaussian bunch profile with DA_{forced} equal to $2.8\,\sigma_{\mathrm{nom}}$ and $3.3\,\sigma_{\mathrm{nom}}$ for the configurations with and without the enhanced b_6 sources respectively.

Lines in Fig. 53 show the expected beam loss according to Eq. (15), for forced DA of $2.8\,\sigma_{\mathrm{nom}}$ (red) and $3.3\,\sigma_{\mathrm{nom}}$ (green). The modification of Eq. (15) for zero-action losses is imperceptible in the latter case, and gave only a small change to the predicted losses for the smaller forced DA obtained with strong b_6 sources (red).

Measurement of changes to the forced DA at the level of $0.5\,\sigma_{\mathrm{nom}}$ due to a b_6 perturbation representative of that expected in the HL-LHC at end-of-squeeze has been achieved at the LHC. This implies that beam losses upon AC-dipole excitation may also be able to provide an observable for rapid validation of dodecapole correction. It is worth emphasising, however, that while based upon LHC experience, the measurement of forced DA does have the potential to assist in the study of dodecapole errors, the forced DA does not directly relate to that of free-betatron oscillations. Thus, an optimisation of the forced DA cannot be guaranteed as a method to optimise the free DA, which is the key figure of merit for Luminosity production.

10.4 Resonance Driving Term Methods

Measurement of driven RDTs with the AC-dipole has been employed in the LHC both for validation of corrections determined by other means, and directly for the

correction of skew octupole errors. This has been discussed extensively in [156, 157]. By careful selection of the driven and free working points to enhance relevant resonances, it has also been demonstrated to be possible to obtain clear measurements of normal and skew decapole resonance lines in the LHC. Figure 54 shows an example of a large-amplitude AC-dipole excitation performed in the LHC operational configuration (with non-colliding pilot beams) at end-of-squeeze. Spectral lines corresponding to normal decapole resonance f_{1004} and skew decapole resonance f_{1130} are clearly visible at frequencies $(-Q_x, 3Q_y)$ (highlighted in pink), and $(0, 4Q_y)$ (highlighted in orange) respectively (the spectral line corresponding to the tune of the free oscillation is indicated in black). Decapole-order RDTs have now been observed on multiple occasions, with sufficient quality to obtain an RDT measurement in the majority of LHC arc BPMs around the ring (see for example [156, 157]). Given these observations at the LHC, it should be possible to employ RDT measurements as an observable to define or validate decapole corrections in the HL-LHC. The relative speed of an RDT measurement compared to the study of feed-down to amplitude detuning may make this measurement particularly useful in the context of decapole correction.

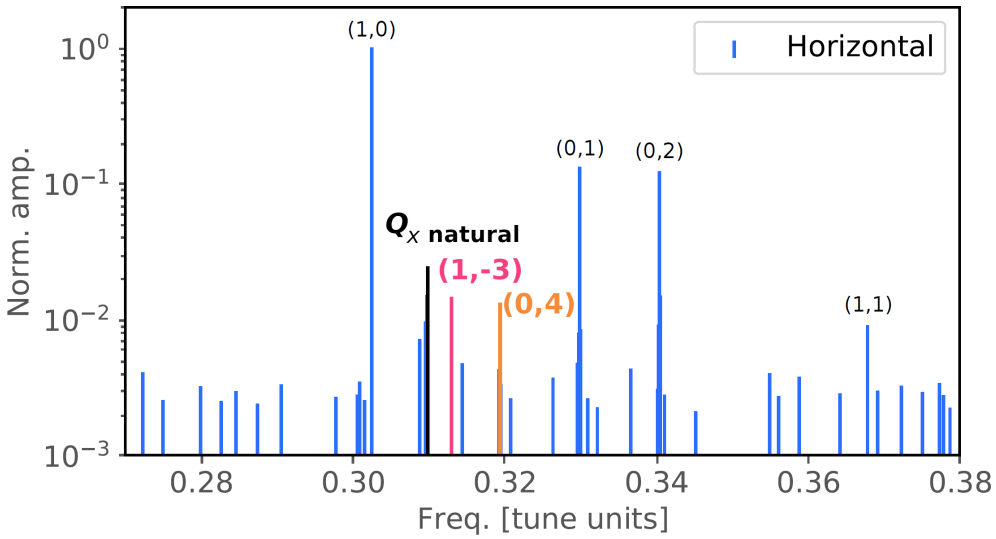

Figure 54: Example of tune spectrum obtained from a large-amplitude AC-dipole excitation in the LHC at end-of-squeeze, showing visible spectral components corresponding to normal and skew decapole resonances. Reproduced from [157].

To date, it has not proven possible to observe dodecapole RDTs in the LHC, even for those configurations with enhanced b_6 sources, which were used to test detuning and dynamic aperture as observables. It was observed during LHC commissioning in 2018, however, that clear feed-down to skew octupole RDTs could be observed in the LHC when the IR crossing scheme was applied. This is shown

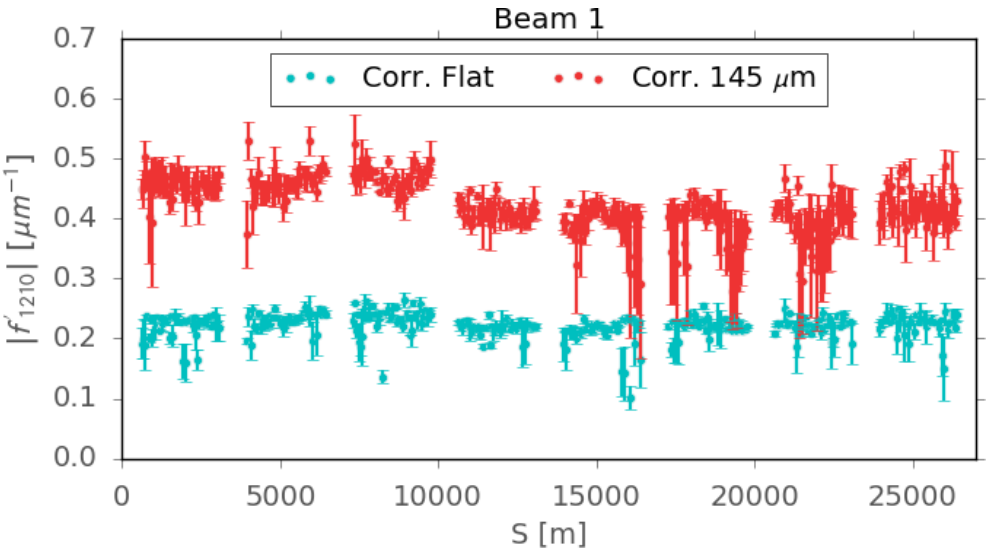

Figure 55: Measurement of skew octupole RDT in the BPMs around the LHC ring, at flat-orbit (green) and with the crossing-scheme applied (red).

in Fig. 55, where a clear change to the f_{1210} skew octupole RDT (driving the $Q_x - Q_y$ resonance) can be observed upon application of the orbit bumps in the IRs. Normal and skew octupole RDTs have proven readily observable at the LHC at 6.5 TeV. Similar to the detuning method described above, a linear change of the octupole RDT can be generated by decapole errors, and a quadratic change with orbit bump by dodecapole errors. Measurement of feed-down to many octupolar RDTs could be obtained in parallel with measurements of feed-down to amplitude detuning, providing a complementary observable. Of particular interest, the measurement of the quadratic feed-down to skew octupole RDTs could also provide an observable for skew-dodecapole errors, for which no observable has yet been demonstrated. As such, this represents an interesting new measurement which, based on LHC experience, will have viable application to the study of high-order errors in IRs.

10.5 Outlook for High-Order Measurement Techniques

Beam-based measurement of decapole and dodecapole errors represents an undoubted step-change in difficulty when compared to techniques for sextupole and octupole measurement, which have been successfully employed in LHC commissioning. Nonetheless, several measurement techniques show significant promise, and have been demonstrated to some degree already in the LHC. Of particular concern moving forward, however is the potentially significant beam-time investment required by many of these techniques, notably feed-down to amplitude detuning

and RDTs. Further, while multiple observables seem viable for normal dodecapole errors, options for skew-dodecapole correction are by comparison limited. No measurement technique has been demonstrated for skew-dodecapole errors in the LHC, although direct DA measurement and second-order feed-down to skew-octupole RDTs may be viable options.

11 Conclusions and outlook

HL-LHC optics commissioning will face unprecedented challenges both in the linear and non-linear regimes. The HL-LHC performance will be ramped up over several years to allow for a staged optics commissioning, starting from relaxed values of IP β^* and crossing angle. Crab cavities and the full remote alignment system will only become operational after the first full year of HL-LHC operation. This will allow to focus the efforts on the commissioning of the new BPMs, orbit correctors, dipoles, and quadrupoles, including linear and non-linear corrections up to octupolar order. In this stage, the peak β-beating can reach up to 150% before corrections and the dominant source has been identified to be the uncertainty on the transfer function of the HL-LHC triplet quadrupoles, with a systematic component within $\pm 10^{-3}$, in relative terms. The following sources are the D2 b_2 and MCBXF sextupolar components, nearing a 10% peak β-beating each. Pre-computed corrections could be applicable for these secondary sources, while validation with the beam might be difficult due to the shadowing effect of the quadrupole errors (the use of dedicated ballistic optics with β^* de-squeezed at top energy might be explored). It should be easier to validate the expected 5% peak vertical β-beating coming from the 11 T dipoles in IR7, if these are eventually installed in the machine.

The beam-based techniques to accomplish this first stage have already been demonstrated to some level during LHC Runs 1, 2 and 3. The resulting beam-based linear and non-linear corrections coarsely agreed with magnetic measurements within a factor of 2. A missing key magnetic measurement was the b_4 longitudinal distribution of MQXA and MQXB that could shed light in the b_4 discrepancy. Efforts should be made in view of HL-LHC to develop a robust and accurate magnetic model that includes the beam pipe effect and longitudinal profiles. It has been requested to measure the longitudinal harmonic content with a 2 cm step in the triplet quadrupoles, 2 cm being the optimum step length before beam based observable discrepancies begin to be measurable [166].

To accomplish the HL-LHC required level of accuracy on β-functions, dispersion and coupling parameters, it will be essential to combine different beam-based techniques and iterate between linear and non-linear corrections, as reported in this note. Simulations have been performed to verify the success of this approach assuming magnetic, alignment and instrumentation tolerances are met. In Run 3, arc BPM calibration errors should be well established to allow an accurate beam-based calibration of the new HL-LHC IR BPMs.

As HL-LHC increases performance reducing β^*, all the HL-LHC systems will be required operationally. The accurate knowledge of the field quality of the IR magnets will be critical in this stage. In particular, it will be required to track the MCBXF orbit corrector's sextupolar components and update corrections ac-

cordingly. Since these are nested correctors, the field quality depends upon two settings (this will be the first magnet with such a feature in the LHC). This correction approach needs to use the FRAS to minimise the use of MCBXF for orbit correction.

The local beam-based correction of decapolar and dodecapolar errors will require a large amount of measurements of feed-down to tune and amplitude detuning and possibly RDTs. At LHC, there is only limited experience with these higher order measurements and corrections. Further developments will be required during Run 3 and with the HL-LHC.

This report focuses in the HL-LHC optics commissioning, nevertheless it provides valuable input for future circular colliders as, e.g. for FCC-ee [184].

A Luminosity loss from beam-beam β-beating

Head-on beam-beam β-beating can be derived from beam-beam tune shift versus the two transverse actions J_x and J_y, see e.g. [178, 179, 180], as:

$$\begin{aligned} Q_x(J_x,J_y) &= \xi \int_0^\infty \frac{\mathrm{d}t}{(1+t)^2} e^{-\frac{J_x+J_y}{2\varepsilon(1+t)}} I_0\left(\frac{J_y}{2\varepsilon(1+t)}\right) \times \\ &\qquad \left[I_0\left(\frac{J_x}{2\varepsilon(1+t)}\right) - I_1\left(\frac{J_x}{2\varepsilon(1+t)}\right)\right] , \qquad (16) \\ \frac{\Delta\beta}{\beta}(J_x,J_y) &= \frac{\Delta\beta_0}{\beta}\frac{Q_x(J_x,J_y)}{\xi} , \qquad (17) \end{aligned}$$

where ξ is the beam-beam parameter and $\Delta\beta_0/\beta$ is the linear β-beating or, equivalently, at $J_x = J_y = 0$. The average β-beating over the bunch can be calculated as

$$\overline{\frac{\Delta\beta}{\beta}} = \int_0^\infty dJ_x \int_0^\infty dJ_y \frac{\Delta\beta}{\beta}(J_x,J_y) e^{-J_x-J_y} = \frac{\Delta\beta_0}{\beta} 0.633... \qquad (18)$$

The rms beam size, σ_x, including this beta-beating is computed using the following relation

$$x^2 = 2\beta J_x \left(1+\frac{\Delta\beta}{\beta}\right)\cos^2\phi = \beta J_x \left(1+\frac{\Delta\beta}{\beta}\right)(1+\cos 2\phi) \qquad (19)$$

and assuming a Gaussian bunch distribution as follows,

$$\begin{aligned} \sigma_x^2 &= \int_0^\infty dJ_x \int_0^\infty dJ_y \int_0^{2\pi} \frac{d\phi}{2\pi}\, x^2 e^{-J_x-J_y} \qquad (20) \\ &= \beta\left(1+\int_0^\infty dJ_x \int_0^\infty dJ_y e^{-J_x-J_y} J_x \frac{\Delta\beta}{\beta}(J_x,J_y)\right) , \end{aligned}$$

where, for simplicity, we have used an emittance of value $\varepsilon = 1$. The triple integral on the r.h.s has an exact solution, yielding

$$\sigma_x^2 \;=\; \beta\left(1+\frac{\Delta\beta_0}{\beta}\frac{1}{2}\right)\,.$$

From this calculation, we expect that the head-on beam-beam interaction with linear β-beating of magnitude $\Delta\beta_0/\beta$ in both horizontal and vertical planes causes a relative luminosity change of

$$\frac{\Delta L}{L} \approx -\frac{\Delta\beta_0}{\beta}\frac{1}{2}\,. \tag{21}$$

Numerical simulations presented in [181, 182] show indeed that the factor relating $\Delta\beta_0/\beta$ and $\Delta L/L$ for head-on collisions is about 1/2, in good agreement with the above derivation, which has been included in the journal publication [183]

References

[1] Editors: I. Béjar Alonso, O. Brüning, P. Fessia, M. Lamont, L. Rossi, L. Tavian, M. Zerlauth, "High-Luminosity Large Hadron Collider (HL-LHC): Technical design report", CERN Yellow Reports: Monographs, Vol. **10** (2020).

[2] G. Apollinari, I. Béjar Alonso, O. Bruning, M. Lamont, and L. Rossi. High-Luminosity Large Hadron Collider (HL-LHC) : Preliminary Design Report. Technical report, 2015. CERN-2015-005.

[3] I. Béjar Alonso and L. Rossi. HiLumi LHC Technical Design Report : Deliverable: D1.10. Technical report, 2015. CERN-ACC-2015-0140.

[4] R. Calaga *et al.*, "First demonstration of the use of crab cavities on hadron beams" Phys. Rev. Accel. Beams **24**, 062001 (2021) .

[5] S. Claudet, "Request for slow luminosity increase", 160$^{\text{th}}$ HiLumi WP2 Meeting, September 2019.

[6] G. Arduini *et al*, "New Parameter table & HL-LHC luminosity ramp-up", 104$^{\text{th}}$ HL-LHC TCC.

[7] R. Tomás *et al.*, "Operational Scenario for the First HL–LHC Run", presented at IPAC'22, Bangkok, Thailand, June 2022

[8] T. Pieloni *et al.*, "Dynamic beta and beta-beating effects in the presence of the beam-beam interactions", in Proc. 57th ICFA Advanced Beam Dynamics Workshop on High-Intensity and High-Brightness Hadron Beams

(HB'16), Malmö, Sweden, Jun. 2016, paper MOPR027, pp. 136–139, ISBN: 978-3-95450-185-4, http://jacow.org/hb2016/papers/mopr027.pdf

[9] L. Medina *et al.*, "Update on Beta beating from head on/long range: is it a problem? Can we measure and compensate it?", 113th HiLumi WP2 Meeting, 2017, https://indico.cern.ch/event/685264/timetable/

[10] N. Karastathis, R. De Maria, S. Fartoukh, Y. Papaphilippou and D. Pellegrini, "Refining the HL-LHC operational settings with inputs from dynamic aperture simulations: a progress report", IPAC2018, Vancouver, BC, Canada, pp. 188-191.

[11] Francesco Cerutti, Marta Sabate Gilarte, "Q4 latest dose estimates and updates for the DS region", 111th HL-LHC TCC, https://indico.cern.ch/event/945883/

[12] F. Van Der Veken *et al.*, "DA Studies for HL-LHC v1.4: Flat optics, MCBRD, and more", 166th HiLumi WP2 Meeting

[13] F. Van Der Veken *et al.*, "The effect from b2 and b3 in D1/D2, including feed-down and beta-beating", 172nd HiLumi WP2 Meeting

[14] F. Van Der Veken *et al.*, "Impact on DA from MCBXF field quality", 122nd HL-LHC TCC, https://indico.cern.ch/event/981951/

[15] A. Herty *et al.*, "HL-LHC full remote alignment study", 10th International Particle Accelerator Conference, Melbourne, Australia, 19 - 24 May 2019, pp. THPGW057.

[16] F. Carlier, *et al.*, "Optics Measurement and Correction Challenges for the HL-LHC", CERN-ACC-2017-0088.

[17] R. Bruce *et al.*, "Updated parameters for HL-LHC aperture calculations for proton beams", CERN-ACC-2017-0051.

[18] E. Metral *et al.*, "Update of the HL-LHC operational scenarios for proton operation", CERN-ACC-NOTE-2018-0002.

[19] S. Kostoglou *et al.*, "DA with beam-beam, coupling & MCBXF errors", 180th HiLumi WP2 Meeting.

[20] M. Hofer and R. Tomás, "Effect of local linear coupling on linear and non-linear observables in circular accelerators" Phys. Rev. Accel. Beams **23**, 094001, 2020.

[21] X. Buffat *et al.*, "Update on the operational scenario taking into account of the constraints on coupling and non-linear optics corrections", 159th HiLumi WP2 Meeting.

[22] S. Kostoglou, "DA with beam-beam at the end of leveling as a function of the emittance", 194th HiLumi WP2 Meeting, 27 Jul 2021.

[23] Stéphane Fartoukh, "Achromatic telescopic squeezing scheme and application to the LHC and its luminosity upgrade", Phys. Rev. ST Accel. Beams **16**, 111002, 2013.

[24] R. De Maria, M. Giovannozzi, Y. Nosochkov and F. Van Der Veken, "HL-LHC IR non-linear correction and options", 77th HiLumi WP2 Meeting, September 2016.

[25] R. Carcagno, *et al.*, "ACCEPTANCE CRITERIA PART A: MQXFA MAGNET", EDMS No. 2031083, Rev. 1.2, 2020.

[26] E. Todesco, "Update on IR magnets field quality: nested correctors and spread of TF in quadrupoles", 186th HiLumi WP2 Meeting, `https://indico.cern.ch/event/977180/`

[27] E. Todesco, L. Fiscarelli, R. Tomás, "WP2 to WP3 interface document. Accuracy and precision of magnetic measurements of interaction region magnets", emds 2436024, LHC-M-ES-0016.

[28] R. Carcagno, "Functional specification LMQXFA cold mass", EDMS No.1686197, Rev. 1.4, 2020.

[29] J. Andersson, "A Linear Framework for Orbit Correction in the High-Luminosity Large Hadron Collider", Lund University, ISSN: 1404-6342, 2019.

[30] J. Andersson *et al.*, "Orbit Correction Studies on the HL-LHC Optics V1.5", CERN-ACC-NOTE-2020-0045.

[31] R. De Maria *et al.*, "Alignment and Mechanical Tolerances for HL-LHC in Point 1 and 5", EDMS No. 2458050 v.0.95, 2021.

[32] F. Rodriguez Mateos *et al.*, "HL-LHC ECR WP3. Baseline for the Inner Triplet Main Circuit", EDMS No. 1832082, Reference: LHC-MQXFB-EC-0001 v.0.9.

[33] R. Tomás *et al.*, "Transfer Function pairing of Q2 magnets", in the 89th HL-LHC TCC meeting.

[34] R. Tomás *et al.*, "Preview of the procedures for linear and nonlinear optics correction and assumptions underlying", 9th HL-LHC collaboration meting, Fermilab, 2019.

[35] "ACCEPTANCE CRITERIA OF CIEMAT IN-KIND CONTRIBUTION (MCBXF NESTED ORBIT CORRECTOR MAGNETS)" EDMS No. 2051311, Rev. 0.2.

[36] E. Todesco *et al.*, "ACCEPTANCE CRITERIA OF IHEP IN-KIND CONTRIBUTION (MCBRD ORBIT CORRECTOR MAGNETS)", EDMS No. 2051870, Rev. 0.95.

[37] F.F. Van der Veken and M. Giovannozzi, "MCBXF Field Quality Impact on DA", 122nd HL-LHC TCC Meeting, 10 December 2020, `https://edms.cern.ch/ui/file/2448062/1/MCBXF_TCC_VdV_WP2.pdf`.

[38] L. Fiscarelli, "Magnetic measurements on MBH magnets (11T dipoles)" in Run III FiDeL meeting 04/02/2020 .

[39] F.F. Van der Veken, "HiLumi LHC: Performance of Non-Linear Correctors", 91st HiLumi WP2 Meeting.

[40] J. Coello, "Effects of the electron lens solenoid on coupling", ABP-HSS Section meeting, 11 October 2017.

[41] R. Bruce *et al.*, "Functional Specification HELs – Functional and Operational Conditions", EDMS no. 2514085.

[42] D. Gamba *et al.*, "Conceptual Specifications for the HL-LHC BPMs", EDMS no. 2387369 v.1.

[43] L. Malina *et al.*, "LHC experience and HL-LHC requirements for BPMs", 157th HiLumi WP2 Meeting, Sep. 2019.

[44] J. Coello, R. Tomás and M. Hofer, "New local optics measurements and correction techniques for the LHC and its luminosity upgrade", Phys. Rev. Accel. Beams **23**, 041001 (2020).

[45] E.H. Maclean, R. Tomás, F.S. Carlier, M.S. Camillocci, J.W. Dilly, J.M. Coello de Portugal, E. Fol, K. Fuchsberger, A. Garcia-Tabares Valdivieso, M. Giovannozzi, M. Hofer, L. Malina, T.H.B. Persson, P.K. Skowronski, and A. Wegscheider. New approach to LHC optics commissioning for the nonlinear era. *Phys. Rev. Accel. Beams* **22**, 061004, 2019.

[46] T. Pugnat, "Impact of non-linear correctors on DA for β^* =30 cm", Special Joint HiLumi WP2/WP4 Meeting, April 5, 2022.

[47] J. Dilly, V. Ferrentino, M. Le Garrec, E.H. Maclean, L. Malina, T. Persson, T. Pugnat, L. van Riesen-Haupt, F. Soubelet, and R. Tomás. First Operational Dodecapole Correction in the LHC. *Phys. Rev. Accel. Beams*, **26**, 121001 (2023). DOI 10.1103/PhysRevAccelBeams.26.121001.

[48] J. Dilly, "Amplitude Detuning from misaligned Triplets and IR multipolar Correctors", 167th WP2 Meeting, 18th Februrary 2020.

[49] J. Dilly, E.H. Maclean, and R. Tomás. Amplitude Detuning from Nonlinear-Corrector- and Triplet-Misalignments in the LHC and HL-LHC. Technical report, 2022. CERN-ACC-NOTE-2022-0078.

[50] "WISE Errortables for 6.5 TeV", \\cern.ch\dfs\Projects\WISE\Other\Errors\2015-2016\fq runII 2015 squeeze 0.4_10.0_0.4_3.0 6.5TeV seeds.

[51] "WISE : An Adaptative Simulation of the LHC Optics", CERN-LHC-Project-Report-971

[52] "MQXF Errortable v5", ITbody_errortable_v5, ITnc_errortable_v5, ITcs_errortable_v5 in /afs/cern.ch/eng/lhc/optics/HLLHCV1.3/errors/.

[53] "D1 Errortable v1", /afs/cern.ch/eng/lhc/optics/HLLHCV1.3/errors/D1_errortable_v1.

[54] Meghan McAteer *et al.*, "Magnet polarity checks in the LHC", CERN-ACC-NOTE-2014-0012.

[55] M. Aiba, S. Fartoukh, A. Franchi, M. Giovannozzi, V. Kain, M. Lamont, R. Tomás, G. Vanbavinckhove, J. Wenninger, F. Zimmermann, R. Calaga, and A. Morita, "First beta-beating measurement and optics analysis for the CERN Large Had ron Collider", Phys. Rev. ST Accel. Beams **12**, 081002 (2009).

[56] R. Tomás, M. Aiba, C. Alabau, O. Brüning, R. Calaga, M. Giovannozzi, V. Kain, P. Hagen, M. Lamont, R. Miyamoto, F. Schmidt, M. Strzelczyk and G. Vanbavinckhove "The LHC optics in practice", 2nd Evian Workshop on LHC Beam Operation, Evian-les-bains, France, Dec. 2010.

[57] T. Persson *et al.*, "LHC injection optics commissioning in 2021 and 2022", CERN, Geneva, Switzerland, Tech. Rep. CERN-ACC-NOTE-2023-0015, 2023.

[58] R. Tomás, F. Carlier, F. Chudoba, L. Deniau, J. Dilly, S. Horney, M. Hostettler, J. Keintzel, S. Kostoglou, M. Le Garrec, E.H. Maclean, T. Nissinen, K. Paraschou, T. Persson, M. Solfaroli, F. Soubelet, A. Wegscheider and J. Wenninger, "Optics for Landau damping with minimized octupolar resonances in the LHC", HB 2023, Geneva, Switzerland.

[59] L. Malina and R. Tomás, "AC-dipole operation with three bunches", in 191st Machine Protection Panel Meeting (LHC) 2020.

[60] L. Malina and R. Tomás, "Experience from the 2018 ATS round optics MD program", in Special LHC Run 3 meeting 2020.

[61] L.Malina *et al.*, "LHC MD 4505: Forced 3D beam oscillations", CERN-ACC-NOTE-2020-0065, 2020.

[62] P. Fessia and H. Mainaud Durand, “Full remote alignment system – Functional specification”, EDMS No. 2166298.

[63] R. Tomás, “Adiabaticity of the ramping process of an ac dipole”, Phys. Rev. ST Accel. Beams **8**, 024401 (2005).

[64] L. Malina and J. Coello de Portugal,“Optics measurements in storage rings based on simultaneous 3-dimensional beam excitation”, in *Proc. IPAC’18*, Vancouver, BC, Canada, May 2018, paper THPAF046, pp. 3068-3071.

[65] L. Malina and R. Tomás, “Optics measurements in the ramp and impact on emittance”, in LHC Machine Committee (LMC) 2019.

[66] R. Bruce, C. Bracco, R. De Maria, M. Giovannozzi, A. Mereghetti, D. Mirarchi, S. Redaelli, E. Quaranta, B. Salvachua, “Reaching record-low β^* at the CERN Large Hadron Collider using a novel scheme of collimator settings and optics", Nucl. Instrum. Methods Phys. Res. Sect. A **848** (2017), `http://www.sciencedirect.com/science/article/pii/S0168900216313092`.

[67] R. Bruce and P. D. Hermes and H. Garcia and R. Kwee-Hinzmann and A. Mereghetti and D. Mirarchi and S. Redaelli and P. Skowronski and G. Valentino and A. Valloni, “IR aperture measurement at β^*=40 cm", CERN-ACC-NOTE-2015-0037, 2015.

[68] P. D. Hermes, R. Bruce, M. Fiascaris, H. Garcia, M. Giovannozzi, R. Kwee-Hinzmann, A. Mareghetti, D. Mirarchi, E. Quaranta, S. Redaelli, B. Salvachua, G. Valentino “Improved aperture measurements at the LHC and results from their applications in 2016”, TUPMW014, Proceedings of IPAC2016, Busan, Korea.

[69] J. Serrano, M. Cattin,“The LHC AC dipole system: an introduction”, CERN-BE-Note-2010-014 (CO).

[70] R. Tomás, S. Fartoukh and J. Serrano, “Operation of the AC dipole in the LHC”, LHC Project Report 1095.

[71] T. Persson, F. Carlier, J. Coello de Portugal, A. Garcia-Tabares Valdivieso, A. Langner, E. H. Maclean, L. Malina, P. Skowronski, B. Salvant, R. Tomás, and A. C. Garcia Bonilla, “LHC optics commissioning: A journey towards 1% optics control”, Phys. Rev. Accel. Beams, **20**, 061002 (2017).

[72] N. Fuster-Martínez, E. Maclean, J. Dilly, R. Bruce, R. Tomás, S. Redaelli, T. Persson and L. Nevay, “Aperture measurements with AC dipole”, CERN-ACC-NOTE-2018-0008.

[73] N. Fuster-Martínez, E. Maclean, J. Dilly, R. Bruce, R. Tomás, S. Redaelli, T. Persson, L. Nevay, “Aperture measurements with AC Dipole at the Large

Hadron Collider", 9th International Particle Accelerator Conference, Vancouver, Canada, 2018. DOI: 10.18429/JACoW-IPAC2018-MOPMF048.

[74] N. Fuster-Martínez, M. Hofer, E. Maclean, D. Mirarchi, R. Bruce, R. Tomás and S. Redaelli, "MD4506: Aperture measurements with AC dipole", https://indico.cern.ch/event/776844/contributions/3231098/attachments/1765264/2865730/AC$_$dipole$_$LCWG$_$2018.pdf.

[75] N. Fuster-Martínez, R. Bruce, M. Hofer, T. Persson, S. Redaelli and R. Tomás, "Aperture measurements with AC-dipoles and movable collimators in the Large Hadron Collider", submitted to PRAB.

[76] R. Bruce, N. Fuster-Martínez, A. Mereghetti, D. Mirarchi, S. Redaelli, "Review of LHC Run 2 machine configurations", 9th LHC Operations Evian Workshop

[77] N. Fuster-Martínez, OMC-OP workshop, 7-8 October 2019 https://indico.cern.ch/event/828284/contributions/3473471/attachments/1921974/3240883/AC$_$dipole$_$OMC$_$OP$_$f.pdf.

[78] R. Calaga, R. Tomás, "Statistical analysis of RHIC beam position monitors performance", *Phys. Rev. ST Accel. Beams* vol. 7, p. 042801, 2004, doi:10.1103/PhysRevSTAB.7.042801

[79] L. Malina, PhD thesis: "Novel beam-based correction and stabilisation methods for particle accelerators", University of Oslo, CERN-THESIS-2018-426 and ISSN1501-7710/No.2041, 2018.

[80] J. Coello de Portugal, F.S. Carlier, A. Langner, T. Persson, P.K. Skowronski, R. Tomás, "OMC Software Improvements in 2014", Proc. 6th Int. Particle Accelerator Conf. (IPAC'15), Richmond, VA, USA, pp. 426–429, doi:10.18429/JACoW-IPAC2015-MOPJE056.

[81] R. Tomás *et al.*, "LHC Optics Measurement and Correction Software Progress and Plans", Proc. 10th Int. Particle Accelerator Conf. (IPAC'19), Melbourne, Australia, pp. 2773–2776.

[82] "OMC repository (Beta-Beat.src)", https://github.com/pylhc/Beta-Beat.src.git.

[83] "OMC repository (omc3)", https://github.com/pylhc/omc3. Documentation at https://pylhc.github.io/omc3/

[84] L. Malina, "Noise and stability", in the Updates on studies, Oct. 2019.

[85] R. Bartolini and F. Schmidt, "A Computer Code for Frequency Analysis of Non-Linear Betatron Motion", CERN, Geneva, Switzerland, Rep. CERN-SL-NOTE-98-017-AP, 1998.

[86] J. Laskar, "Frequency analysis for multi-dimensional systems. Global dynamics and diffusion", *Physica D* vol. 67, p. 257-281, 1993.

[87] N. Biancacci and R. Tomás, "Using ac dipoles to localize sources of beam coupling impedance", Phys. Rev. Accel. Beams **19**, 054001 (2016).

[88] J. Coello, "Details of SUSSIX with fixed frequency" in Review of the ESRF optics measurements, 2015.

[89] J. Coello, PhD thesis: "Local Optics Corrections in the HL-LHC", Universidad Politecnica de Cataluyna, CERN-THESIS-2021-104.

[90] L. Malina, "(De)tuned ring and a look into crystal ball", in the OMC Celebration Meeting, Aug. 2016.

[91] L. Malina, "New approach to frequency analysis of beam data", in the ABP-HSS Section Meetings, Jun. 2019.

[92] P. Skowronski, "RDTs in PS vs frequency analysis", in the Software development - LS2 IV, Mar. 2019.

[93] L. Malina *et al.*,"Performance optimization of turn-by-turn beam position monitor data harmonic analysis", in *Proc. IPAC'18*, Vancouver, Canada, May 2018, paper THPAF045.

[94] Ç. Candan, "A method For Fine Resolution Frequency Estimation From Three DFT Samples", *IEEE Signal Procces. Lett.*, vol. **18**, p. 351-354, 2011.

[95] L. Malina, "Harpy", `https://github.com/pylhc/omc3/tree/master/omc3/harpy`.

[96] Y. Alexahin and E. Gianfelice-Wendt, "Determination of linear optics functions from turn-by-turn data", JINST **6**, P10006, (2011).

[97] L. Malina, "Frequency analysis on fingers", in the Software development - LS2 II, Mar. 2019.

[98] F. Liu, K.M. Ting, Z. Zhou, "Isolation Forest", in *Proc. 8th IEEE International Conference on Data Mining*, Washington, USA, Dec. 2008, pp. 413–422. `doi:10.1109/ICDM.2008.17`

[99] E. Fol *et al.*, "Detection of faulty beam position monitors using unsupervised learning", *Phys. Rev. Accel. Beams* **23**, p. 102805 (2020).

[100] R. Tomás, *et al.*, "Record low β beating in the LHC" Phys. Rev. ST Accel. Beams **15**, 091001, September 2012.

[101] F. Carlier and R. Tomás, "Accuracy and feasibility of the β^* measurement for HL-LHC using K-modulation", Phys. Rev. Accel. Beams vol. **20**, p. 011005 (2017).

[102] P. Thrane, *et al.*, "Measuring β^* in SuperKEKB with K modulation" Phys. Rev. Accel. Beams **23**, 012803, January 2020.

[103] D. Gamba, *et al.*, "Update of beam dynamics requirements for HL-LHC electrical circuits", CERN-ACC-2019-0030.

[104] N. Beev, M. Martino, M. Cerqueira Bastos, "Upgrade of the LHC class 1 power converter precision measurement systems: Class 0.5", EDMS No. 2379888.

[105] M. Hofer, *et al.*, "Impact of tune jitter on β^* accuracy and potential hardware upgrades", 124th HL-LHC Technical Coordination Committee, January 2021.

[106] "Minutes of the 136th Technical Coordination Committee meeting.", `https://edms.cern.ch/document/2477067/1`, June 2021.

[107] D.W. Wolf, "Analysis of tune modulations in the LHC", Bachelor thesis, CERN-THESIS-2018-251.

[108] E.H. Maclean, *et al.*, "A new approach to the LHC optics commissioning for the nonlinear era", *Phys. Rev. Accel. Beams* **22**, p. 061004 (2019).

[109] S. Visavadia, "Investigation into Possible Sources of Tune Jitter in the LHC", Master thesis, CERN-THESIS-2019-131.

[110] F. Carlier *et al.*, "Challenges of K-modulation measurements in the LHC Run 3", in emphProc. IPAC'23, Venice, Italy, May 2023, pp. 531-534.

[111] R. Alemany-Fernández *et al.*, "Cross-Calibration of the LHC Transverse Beam-Profile Monitors", in *Proc. IPAC2017*, Copenhagen, Denmark, May 2017, paper MOPAB130, pp. 437–440.

[112] L. van Riesen-Haupt, J.M. Coello de Portugal, E. Fol, A. Seryi, and R. Tomás, "K-Modulation Developments via Simultaneous Beam Based Alignment in the LHC", in *Proc. IPAC2017*, Copenhagen, Denmark, May 2017, paper TUPVA042, pp. 2159–2162,

[113] H. Garcia-Morales et al., "Phase advance constraint in K-modulation for β^* determination in the LHC", Submitted to PRAB (2020)

[114] J. Coello, L. Malina and R. Tomás García, "MD3287: Luminosity scans with waist shifts", CERN-ACC-NOTE-2020-0048.

[115] R. Tomás *et al.*, "LHC optics model, measurements and corrections", Phys. Rev. ST Accel. Beams **13**, 121004 (2010).

[116] J. F. Cardona, A. C. García, and R. Tomás, "Local correction of quadrupole errors at LHC interaction regions using action and phase jump analysis on turn-by-turn beam position data", *Phys. Rev. Accel. Beams* **20**, p. 111004 (2017).

[117] J. F. Cardona, Y. Rodríguez, and R. Tomás, "A twelve-quadrupole correction for the interaction regions of high-energy accelerators", arXiv:2002.05836 [physics.acc-ph] (2020).

[118] J. F. Cardona, *et al.*, "Progress on action-phase jump for LHC local optics correction", IPAC 2022, Bangkok, Thailand.

[119] A. Langner and R. Tomás, "Optics measurement algorithms and error analysis for the proton energy frontier", Phys. Rev. ST Accel. Beams **18**, 031002 (2015).

[120] A. Wegscheider, A. Langner, R. Tomás and A. Franchi, "Analytical N beam position monitor method", Phys. Rev. Accel. Beams **20**, 111002 (2017)

[121] A. García-Tabarés Valdivieso and R. Tomás, "Optics-measurement-based beam position monitor calibrations in the LHC insertion regions", Phys. Rev. Accel. Beams **23**, 042801 (2020).

[122] J. Keintzel, L. Malina and R. Tomás, "Momentum compaction factor measurements in the Large Hadron Collider", in *Proc. IPAC2021*, Foz do Iguazu, Brazil, May 2021, paper TUPAB011, pp. 1360–1363.

[123] J. Keintzel, R. Tomás, R. Bruce, M. Giovannozzi, T. Risselada, and F. Zimmermann, "Lattice and optics options for possible energy upgrades of the Large Hadron Collider", *Phys. Rev. Accel. Beams* **23**, p. 101602 (2020).

[124] J. Keintzel, M. Le Garrec, E. Todesco, R. Tomás, J. Wenninger, S. Fartoukh, T. Persson, M. Solfaroli, "60° phase advance optics measurements in the Large Hadron Collider at CERN", in *Proc. IPAC2023*, Venice, Italy, May 2023, paper MOPL026, pp. 571–574.

[125] T. L. Lai, H. Robbins, "Strong consistency of least-squares estimates in regression models", in *Journal of Multivariate Analysis*, vol. 23, no. 1, pp. 77–92, 1987. doi:10.1016/0047-259X(87)90179-5

[126] R.M. Rifkin, R.A. Lippert, "Notes on Regularized Least Squares", Tech. Rep. MIT-CSAIL-TR-2007-025, CBCL-268, 2007.

[127] E. Fol, J. M. Coello de Portugal, G.Franchetti and R. Tomás, "Application of Machine Learning to Beam Diagnostics", presented at the 39th Int. Free Electron Laser Conf. (FEL'19), Hamburg, Germany, Aug. 2019, paper WEB03.

[128] E. Fol, J.M. Coello de Portugal, G. Franchetti, and R. Tomás, "Optics Corrections Using Machine Learning in the LHC", in *Proc. IPAC'19*, Melbourne, Australia, May 2019, pp. 3990–3993, doi:10.18429/JACoW-IPAC2019-THPRB077

[129] E. Fol, G. Franchetti, and R. Tomás, "Machine Learning Techniques for Optics Measurements and Correction", in *Proc. IPAC'20*, Caen, France, May 2020, pp. 61–66. doi:10.18429/JACoW-IPAC2020-WEVIR12

[130] J. Dilly, L. Malina, and R. Tomás. An Updated Global Optics Correction Scheme. Technical report, 2018. CERN-ACC-NOTE-2018-0056.

[131] R. Tomás *et al.*, "Procedures and accuracy estimates for beta-beat correction in the LHC", LHC Project Report 941.

[132] F. Soubelet *et al.*, "Rigid waist shift: A new method for local coupling corrections in the LHC interaction regions", Phys. Rev. Accel. Beams **26**, 051001, May 2023.

[133] A. Wegscheider and R. Tomás, "Local observable for linear lattice imperfections in circular accelerators", Phys. Rev. Accel. Beams **23**, 054002, May 2020.

[134] E. Fol, R. Tomás, G. Franchetti, "Supervised learning-based reconstruction of magnet errors in circular accelerators". Eur. Phys. J. Plus **136**, 365 (2021).

[135] R. Tomás, "Optimizing the global coupling knobs for the LHC", CERN-ATS-Note-2012-019 MD.

[136] A. Calia, *et al.*, "Online coupling measurement and correction throughout the LHC Cycle", in *Proc. ICALEPCS'17*, Barcelona, Spain, October 2017, paper TUPHA119, pp. 686-691

[137] T. Persson and R. Tomás, "Improved control of the betatron coupling in the Large Hadron Collider", *Phys. Rev. ST Accel. Beams* **17**, p. 051004 (2014).

[138] T. Persson, *et al.*, "Transverse Coupling Measurements With High Intensity Beams Using Driven Oscillations", in Proc. 9th Int. Particle Accelerator Conf. (IPAC'18), Vancouver, Canada, Apr.-May 2018, pp. 208-211.

[139] T. Nissinen, F. Carlier, M. Le Garrec, E.H. Maclean, T.H.B. Persson, R. Tomás, A. Wegscheider, "LHC optics measurements from transverse damper for the high intensity frontier", Proceedings of HB2023, Geneva, Switzerland.

[140] T. Persson, *et al.*, "LHC 3324: Counteracting coupling decay at injection", CERN-ACC-NOTE-2021-0008.

[141] T. Persson, "Stability of Linear Coupling in Run 2", 159th WP2 Meeting, 17th September 2019.

[142] T. Persson, "Transverse Coupling", OMC-OP Workshop, CERN, 7th October 2019.

[143] J. Wenninger , *et al.*, "LHC MD2877: Beam-beam long range impact on coupling measurements", CERN-ACC-NOTE-2018-0026.

[144] A. Ribes Metidieri and X. Buffat, "Studies of PACMAN effects in the HL-LHC", CERN-ACC-NOTE-2019-0037 (CERN, Geneva, Switzerland, 2019)

[145] G. Iadarola, "HL-LHC filling schemes", 172nd HiLumi WP2 Meeting, 7 Apr 2020.

[146] F. Ruggiero, G. Rumolo, F. Zimmermann and Y. Papaphilippou, "Beam Dynamics Studies for Uniform (Hollow) Bunches or Super-bunches in the LHC: Beam-Beam Effects, Electron Cloud, Longitudinal Dynamics, and Intrabeam Scattering", LHC Project Report 627 (CERN, Geneva, Switzerland, 2002)

[147] F. Carlier *et al.*, "LHC Run 2 Optics Commissioning Experience in View of HL-LHC", IPAC 2019.

[148] T. Persson, *et al.*, "MD4944: Local linear coupling measurement at the IPs", CERN-ACC-NOTE-2020-0013.

[149] F. Soubelet, T.H.B. Persson and R. Tomás, "Prospect for Interaction Region Local Coupling Correction in the LHC Run 3", Proc. IPAC2021, May 2021.

[150] F. Soubelet, T.H.B. Persson and R. Tomás, "First Interaction Region Local Coupling Corrections in the LHC Run 3", Proc. IPAC2021, June 2021.

[151] F. Carlier, J. Coello, S. Fartoukh, E. Fol, A. García-Tabares, M. Giovannozzi, M. Hofer, A. Langer, E.H. Maclean, L. Malina, L. Medina, T.H.B. Persson, P. Skowronski, R. Tomás, F. Van der Veken, and A. Wegscheider. Optics Measurement and Correction Challenges for the HL-LHC. Technical report, 2017. CERN-ACC-2017-0088.

[152] S. White, E. Maclean and R. Tomás, "Direct amplitude detuning measurement with AC dipole", Phys. Rev. ST Accel. Beams **16**, 071002, July 2013.

[153] R. Tomás, "Direct Measurement of Resonance Driving Terms in the Super Proton Synchrotron (SPS) of CERN using Beam Position Monitors", University of Valencia, CERN-THESIS-2003-010.

[154] R. Tomás, "Normal Form of Particle Motion under the Influence of an AC Dipole", Phys. Rev. ST Accel Beams **5**, 54001 (2002).

[155] R. Tomás, M. Bai, R. Calaga, W. Fischer, A. Franchi and G. Rumolo, "Measurement of global and local resonance terms", Phys. Rev. ST Accel. Beams **8**, issue 2, 024001 (2005).

[156] Felix S. Carlier, “A Nonlinear Future - Measurements and corrections of nonlinear beam dynamics using forced transverse oscillations”, PhD Amsterdam University, CERN-THESIS-2020-025.

[157] F.S. Carlier, R. Tomás and E.H. Maclean. Measurement and Correction of Resonance Driving Terms in the Large Hadron Collider, Submitted to Phys. Rev. Accel. Beams.

[158] E.H. Maclean, “MQXB & feeddown in HL”, in HL-LHC strategy report discussion.

[159] E. Todesco, b4 correction in IP1 and IP5 , https://indico.cern.ch/event/876308/

[160] E.H. Maclean, The b4 issue, https://indico.cern.ch/event/892017/

[161] E. Todesco, Update on the b4, https://indico.cern.ch/event/901165/

[162] S. Izquierdo Bermudez, Recap on the available BS contribution to the field quality in the triplets for the HL-LHC, https://indico.cern.ch/event/924096/

[163] L. Van Riesen-Haupt, Amplitude detuning in SAD vs MAD-X for the LHC, https://indico.cern.ch/event/949105/

[164] Fidel: https://lhc-div-mms.web.cern.ch/lhc-div-mms/tests/MAG/Fidel/.

[165] T. Pugnat, *et al.*, “3D magnetic field analysis of LHC final focus quadrupoles with Beam Screen”, IPAC 2021. https://ipac2021.vrws.de/papers/tupab225.pdf

[166] T. Pugnat, *et al.*, “Computation of beam based quantities with 3D final focus quadrupoles field in circular hadronic accelerators”, NIM-A **978**, October 2020.

[167] A. Simona *et al.*, “High order time integrators for the simulation of charged particle motion in magnetic quadrupoles", Computer Physics Communications, 239 (2019).

[168] M. Giovannozzi. Field quality and DA. 6th Collaboration Meeting (14-16 November 2016, Paris, Espace St Martin).

[169] E.H. Maclean, F.S. Carlier, J.W. Dilly, M. Giovannozzi, N. Karastathis, T.H.B. Persson, and R. Tomás. Non-linear optics measurements and corrections. In *2nd edition of the High Luminosity LHC Book*, number 28, 2019.

[170] SixTrack - 6D Tracking Code.

[171] E.H. Maclean, F.S. Carlier, E. Cruz Alaniz, B. Dalena, J.W. Dilly, E. Fol, M. Giovannozzi, M. Hofer, L. Malina, T.H.B. Persson, J.M. Coello de Portugal, P.K. Skowronski, M.S Camillocci, R. Tomás, A. Garcia-Tabares Valdivieso, and A. Wegscheider. Report from LHC MD 2158: IR-nonlinear studies. Technical report, 2017. CERN-ACC-NOTE-2018-0021.

[172] J.W. Dilly, A. Markus, A. Theodoros, F. Carlier, M. Hofer, L. Malina, E.H. Maclean, E. Solfaroli Camillocci, and R. Tomás. Report and Analysis from LHC MD 3311: Amplitude detuning at end-of-squeeze. Technical report, 2019. CERN-ACC-NOTE-2019-0042.

[173] E. H. Maclean, M. Giovannozzi, and R. B. Appleby. Innovative method to measure the extent of the stable phase-space region of proton synchrotrons. *Phys. Rev. Accel. Beams*, 22(034002), 2019.

[174] E.H. Maclean, F.S. Carlier, M. Giovannozzi, and R. Tomás. Report from LHC MD 2171: Dynamic aperture at 6.5 TeV. Technical report, 2018. CERN-ACC-2018-0054.

[175] A. Bazzani, M. Giovannozzi, and E. H. Maclean. Analysis of the nonlinear beam dynamics at top energy for the CERN Large Hadron Collider by means of a diffusion model. *Eur. Phys. J. Plus*, 135(77), 2020.

[176] F.S. Carlier, R. Tomás, E.H. Maclean, and T.H.B. Persson, "First Demonstration of Dynamic Aperture Measurements with an AC-dipole", Phys. Rev. Accel. Beams **22** 031002 (2019).

[177] M. Giovannozzi, Proposed scaling law for intensity evolution in hadron storage rings based on dynamic aperture variation with time. *Phys. Rev. ST. Accel. Beams*, **15**(024001), 2012. URL `https://journals.aps.org/prab/pdf/10.1103/PhysRevSTAB.15.024001`.

[178] A.W. Chao, *The Beam-beam instability*, SLAC-PUB-3179 (1983). `http://www.iaea.org/inis/collection/NCLCollectionStore/_Public/15/021/15021887.pdf`

[179] A.W. Chao, P. Bambade and W.T. Weng, *Nonlinear beam-beam resonances*, SLAC-PUB-3545 (1985). `http://www.slac.stanford.edu/cgi-wrap/getdoc/slac-pub-3545.pdf`

[180] R. Tomás, X. Buffat, S. White, J. Barranco, P. Goncalves Jorge, and T. Pieloni, "Beam-beam amplitude detuning with forced oscillations", Phys. Rev. Accel. Beams **20**, 101002 (2017).

[181] Vladik Balagura, "Beam-beam correction in vdM scans", LHC Lumi Days, 4-5 June 2019.

[182] T. Pieloni and C. Tambasco, “Beam-beam effects in Van der Meer scans: COMBI and TRAIN beam-beam corrections”, LHC Lumi Days, 4-5 June 2019.

[183] A. Babaev, T. Barklow, O. Karacheban, W. Kozanecki, I. Kralik, A. Mehta, G. Pasztor, T. Pieloni, D. Stickland, C. Tambasco, R. Tomás and J. Wanczyk, “Impact of beam-beam effects on absolute luminosity calibrations at the CERN Large Hadron ColliderImpact of beam-beam effects on absolute luminosity calibrations at the CERN Large Hadron Collider”, EPJ C, Vol. **84**, 17, (2024).

[184] Tessa K. Charles, Bernhard Holzer, Rogelio Tomás, Katsunobu Oide, Léon van Riesen-Haupt and Frank Zimmermann , “Alignment & stability challenges for FCC-ee”, EPJ Techniques and Instrumentation, vol. **10**, Article number: 8 (2023).